Engineering Library

Journal of Research

of the

National Bureau of Standards

NOVEMBER 1949

VOLUME 43 NUMBER 5

PERIODICALS OF THE NATIONAL BUREAU OF STANDARDS

Journal of Research

The National Bureau of Standards is the principal agency of the Federal Government for fundamental research in physics, chemistry, and engineering. It has the custody of the national standards of physical measurement in terms of which all working standards in research laboratories and industry are calibrated, and carries on necessary research leading to improvement in such standards and methods of measurement. It also has a general responsibility for basic research in physics, chemistry, and engineering, and for development of improved methods for testing materials and equipment. It determines physical constants and properties of materials, tests and calibrates standard measuring apparatus and reference standards, and studies technical processes. The results of the Bureau's research and investigations are published in the JOURNAL OF RESEARCH.

Research Papers

Reprints of individual articles appearing in the JOURNAL OF RESEARCH. They are made available to serve the needs of research workers, technical groups, and others for the separate papers relating to the special subjects in which they are interested.

Technical News Bulletin

Contains short but complete summaries of research, development, and testing in progress at the Bureau, accounts of the Bureau's national and international activities, scientific and technical announcements of new plans and programs, and a list of publications by members of the staff. It is a prompt and reliable source of official information of value to those who desire to keep in touch with the general activities of the Bureau.

Basic Radio Propagation Predictions

The CRPL-D series, Basic Radio Propagation Predictions, is issued as a monthly publication for those concerned with radio communication in determining the best sky-wave frequencies over any path at any time of day for average conditions for the month of prediction, which is made 3 months in advance. Charts of extraordinary-wave critical frequency for the F2 layer, of maximum usable frequency for a transmission distance of 4,000 km, and of percentage of time occurrence for transmission by sporadic E in excess of 15 Mc, for a distance of 2,000 km, are included.

ANNUAL SUBSCRIPTION Send order, with remittance, to Superintendent of Documents U. S. Government Printing Office, Washington 25, D. C.	United States, Canada, Cuba, Mexico, Newfoundland, Republic of Panama	Other countries
JOURNAL OF RESEARCH of the National Bureau of Standards: 12 monthly issues (2 volumes), paper covers	$4.50	$5.50
Bound volume (½ year, 1 volume), blue buckram	3.00	3.50
RESEARCH PAPERS	(*)	(*)
TECHNICAL NEWS BULLETIN, 12 monthly issues	1.00	1.35
BASIC RADIO PROPAGATION PREDICTIONS, 12 monthly issues	1.00	1.25

*The prices of the separate Research Papers appearing in this JOURNAL are given in the Contents. If 100 or more copies of any separate are ordered, a discount of 25 percent is allowed. Those who desire copies of separate Research Papers should send their orders and remittances without delay to the Superintendent of Documents, U. S. Government Printing Office, Washington 25, D. C. This will aid him to determine the number of copies to be printed for sale. Research Papers are not printed from electrotypes and usually no more reprints can be had when the first and only printing is exhausted.

The printing of this publication has been approved by the Director of the Bureau of the Budget, April 23, 1947.

U. S. DEPARTMENT OF COMMERCE
Charles Sawyer, Secretary
NATIONAL BUREAU OF STANDARDS
E. U. Condon, Director

NOVEMBER 1949
VOLUME • 43
NUMBER 5

JOURNAL OF RESEARCH

of the

NATIONAL BUREAU OF STANDARDS

Contents

RP		Page
2034.	Some physical properties of porcelains in the systems magnesia-beryllia-zirconia and magnesia-beryllia-thoria and their phase relations. S. M. Lang, L. H. Maxwell, and R. F. Geller. (Price 15 cents)	429
2035.	Laboratory flow tests of fixed spray nozzles with hydrocarbons and with air. M. R. Shafer and H. L. Bovey. (Price 10 cents)	449
2036.	Mechanical production of very thin oscillator plates. Leland T. Sogn and Walter J. Howard. (Price 5 cents)	459
2037.	Instability in shear of simply supported square plates with reinforced hole. Wilhelmina D. Kroll. (Price 5 cents)	465
2038.	Physical properties of sixty API-NBS hydrocarbons. Alphonse F. Forziati and Frederick D. Rossini. (Price 5 cents)	473
2039.	Fatigue characteristics of electroformed sheets with and without iron backing. Harry K. Herschman and Carroll Thomas. (Price 10 cents)	477
2040.	Interfacial instability and mixing in stratified flows. Garbis H. Keulegan. (Price 10 cents)	487
2041.	The remainder in linear methods of approximation. W. E. Milne. (Price 10 cents)	501

For sale by the Superintendent of Documents, U. S. Government Printing Office, Washington 25, D. C. • Price 45 cents
$4.50 per year on subscription

UNITED STATES GOVERNMENT PRINTING OFFICE, WASHINGTON : 1949

U. S. Department of Commerce
National Bureau of Standards

Research Paper RP2034
Volume 43, November 1949

Part of the Journal of Research of the National Bureau of Standards

Some Physical Properties of Porcelains in the Systems Magnesia-Beryllia-Zirconia and Magnesia-Beryllia-Thoria and Their Phase Relations[1]

By S. M. Lang, L. H. Maxwell, and R. F. Geller

The ternary eutectic for the system MgO-BeO-ZrO_2 was located at mole composition $4MgO:5BeO:3ZrO_2$ and 1,669° C, and that for the system MgO-BeO-ThO_2 was located at mole composition $5MgO:10BeO:1ThO_2$ and 1,797° C. No binary or ternary compounds were found in either of the systems, and an area of solid solution is indicated for each. A number of bodies were found suitable for various high-strength and high-temperature services where thermal shock resistance is not of prime importance. The compressive strength values at room temperature ranged as high as 266,000 lb/in.^{2} for some porcelains in both systems. The maximum values for the strength in bending at room temperatures and at 1,800° F (982° C) were considerably higher for the MgO-BeO-ZrO_2 bodies (39,000 and 32,000 lb/in.^{2}, respectively) than for the MgO-BeO-ThO_2 bodies (14,000 and 16,000 lb/in.^{2}, respectively), and the modulus of rupture value at 1,800° F (982° C) of one body in the binary system MgO-ZrO_2 was 29,000 lb/in^2. The resistance to thermal shock for the MgO-BeO-ZrO_2 porcelains was fair to good, and for the MgO-BeO-ThO_2 porcelains it was poor. All of the MgO-BeO-ZrO_2 bodies can be matured in commercial kilns used currently in the porcelain industry, whereas part of the MgO-BeO-ThO_2 porcelains and none of the MgO-ZrO_2 porcelains can be so matured.

I. Introduction

Under the impetus of the recent war and because of the outstanding advances made in the design and efficiency of such power plants as the gas-turbine and jet-propulsion engines, varied programs are being sponsored by industrial, research, and government laboratories in the realm of high-temperature materials.

In design and, especially, in efficiency the present models of the various heat power-plants are severely restricted by the ability of some of their components to withstand the required high operational temperatures and stresses. The important physical properties of such power-plant elements are dependent to a large extent upon whether the part in question is to be stationary or moving, whether the engine is to be continuously or intermittently operated, or any combination of these conditions [1].[2]

The allowable metal-blade temperature of the present conventional gas turbine, for example, is limited to approximately 1,500° F (815° C), but conventional fuels could provide inlet-gas temperatures exceeding 3,500° F (1,927° C) [1] and, thereby, greatly increase the efficiency of such an engine. In addition to refractoriness, considerable mechanical strength is required in certain instances as illustrated, for example, by the tensile stresses set up in a turbine blade by centrifugal force [2, 3, 4]. A number of other properties also are required, among which are: high thermal shock resistance, high thermal conductivity, resistance to oxidation and erosion, and ability to maintain exacting dimensions at high temperatures.

Many of the ceramic oxides and combinations of these oxides are well suited for such diversified uses as turbine nozzles, interstage stator blades, rotors and buckets, rocket liners and nozzles, and control vanes because of their high melting points, low density, and potentially low cost and availabil-

[1] This project was sponsored in part by the Office of Naval Research under Contract No. N Aori 2-47, Project No. NR 032074.

[2] Figures in brackets indicate the literature references at the end of this paper.

ity. The limitations imposed by the glassy bond of the conventional feldspathic bodies and the earlier developments leading to the formulation of the glass-free oxide porcelains are discussed in detail in a previous report [5]. Excepting the detailed studies of the phase relations of the oxides [6], many reports of the pure ceramic oxide and of the ceramic oxide-metal combination studies are still in the restricted classification.

In order to supply some of the fundamental information upon which the practical work of producing ceramics to meet the future needs can be based, there was undertaken a study of the characteristics of variously heated binary and ternary combinations of the high melting-point oxides. A preliminary report was published in 1941 [7], and a report on some of the porcelain compositions of the systems MgO-BeO-Al_2O_3, CaO-BeO-Al_2O_3, BaO-BeO, BeO-Al_2O_3-ThO_2, and BeO-Al_2O_3-ZrO_2, along with the probable phase relations in these systems, was published in 1946 [5]. A preliminary report on the strength in tension and the creep characteristics of a number of bodies described in the 1946 report also was made in 1946 [2], and the final report was published as NACA Technical Note 1561, April 18, 1949. The present paper reports the results obtained since the 1946 report [5].

It may be of interest to the reader to compare some of the reported physical properties of a few refractory ceramic bodies and of some oxide porcelain bodies. These data are given in table 1.

II. Materials

The oxides used in the preparation of specimens for testing the various physical properties were commercially available high-purity materials, whereas the oxides used in the study of the phase relations were of the highest purity available.

Beryllia (BeO): (1) Commercial grade of nominal 99.7-percent purity. The spectrograms show only traces of copper, iron, and magnesium and very weak lines for silicon.

(2) Fluorescent grade of over 99.9-percent purity.

Magnesia (MgO): (1) Fused, recrystallized material of nominal 97-percent purity.

(2) Especially selected, water-clear crystals of artificial periclase of over 99-percent nominal purity (furnished through the courtesy of The Norton Co.).

Thoria (ThO_2) (1) Calcined material of over 99-percent nominal purity. The spectrograms show only very weak lines for calcium, copper, and silicon.

(2) Calcined material of at least 99.99-percent purity.

Zirconia (ZrO_2): Commercial grade of nominal 99-percent purity. After recalcining at 1,440° C,[3] the spectrograms showed medium lines for columbium, titanium, and only very weak lines or traces for calcium, copper, iron, magnesium, lead, and silicon. This material was used for both the porcelain test specimens and for the phase relation studies.

As prepared for use, the materials were, in all instances, sufficiently finely divided to pass the No. 325 U. S. Standard Sieve. In order to obtain this desired fineness, it was necessary to reduce the particle sizes of all of the materials except the fluorescent grade beryllia. The commercial grade of beryllia was reduced to about 95 percent of minus 325 mesh material by wet grinding for 2 hr in a porcelain mill with alumina balls (approximately 2% total mill gain of which about 1½% was gained from the alumina balls). Both grades of magnesia could be reduced in size fairly easily in a mullite mortar, but it was found more advisable for quantity work to mill the less pure material in alcohol for 30 min to 1 hr in a porcelain mill with alumina balls (less than ¼% total mill gain). Both the thoria and the zirconia were dry-ground in a steel rod-mill for 30 hr and then cleaned. A magnetic separator was used first, and the material was then washed alternately with 1:3 hydrochloric acid and distilled water until both the decanted acid and wash water gave a negative iron test using potassium thiocyanate or potassium ferrocyanide or both as indicators.

III. Methods

In order to insure the desired reproducibility of results and to prevent segregation of the batch constituents during specimen preparation, a definite compounding method was followed.

The calculations of weight composition from the desired mole composition were based upon the accepted molecular weights of the oxides [8]. Calculations were made to ±0.005 weight percent.

[3] All temperature values are given according to the International Temperature Scale of 1927.

TABLE 1. *Some physical properties of various refractory ceramic bodies*

TABLE 1. *Some physical properties [a] of various refractory ceramic bodies*

[Other compilations of a similar nature, but without literature references, may be found in Ceramic Age **50,** 19 (1947); Materials and Methods **26,** 87 (Dec. 1947); Electronics **17,** 136 (May 1944) and **12,** 33 (April 1939); Ceramic Ind. **39,** 70 (1942); and Rev. Sci. Instr. **12,** 527 (1941).]

Body types	Porosity		Specific gravity		Coefficient of linear thermal expansion			Thermal conductivity [b]			Resistance to thermal shock		Compressive strength			Tensile strength			Modulus of rupture		
	Value	Reference [c]	Value	Reference [c]	Range	Value	Reference [c]	Range	Value	Reference [c]	Value (relative)	Reference [c]	Temperature	Value	Reference [c]	Temperature	Value	Reference [c]	Temperature	Value	Reference [c]
	Percent		*g/cm³*		°*C*	$n\times10^{-6}$/°*C*		°*C*	$n\times10^{-3}$ *watts*				°*C*	$n\times10^{3}$ *lb/in.²*		°*C*	$n\times10^{3}$ *lb/in.²*		°*C*	$n\times10^{3}$ *lb/in.²*	
Steatite	0.0	[1]	2.6 to 2.8	[1]	25 to 100	6.0 to 9.0	[1]	24 to 100	About 29	[1]	Good	[1]		117 to 138	[1]		8 to 13	[1]		16 to 22	[1]
	0.0 to 0.08	[2]	2.7 to 2.7	[2]	25 to 100	6.9 to 7.7	[2]		25	[2]				65 to 85	[2]		7.5 to 10	[2]		18 to 20	[2]
					25 to 700	8.6 to 10.2	[2]												25	20	[3]
Mullite	3.9	[4]	3.2	[4]	20 to 1,320	4.5	[6]	425 to 870	17 to 23	[5]	do	[5]		60 to 200	[5]		10 to 30	[5]		15 to 25	[5]
	nil	[5]	2.3 to 2.9	[5]	0 to 1,700	5.3	[7]	95 to 1,430	12	[6]											
			3.03	[6]	300 to 700	8.2	[7]	335	32	[8]											
					20 to 1,430	5.5	[18]														
Zircon			4.7	[9]	25 to 1,000	4.6	[5]	425 to 870	17 to 23	[5]	Very good.	[5]		60 to 200	[5]		10 to 30	[5]		15 to 25	[5]
			4.6	[10]	20 to 1,550	4.2	[6]	200 to 1,000	19	[6]											
					0 to 1,500	4.2 to 6.4	[7]	300	45	[8]											
					300 to 700	4.8 to 9.2	[7]														
					20 to 1,340	4.1	[18]														
					20 to 1,500	5.1	[19]														
Alumina	0	[1]	3.24	[4]	20 to 1,000	7.0	[6]	425 to 870	34 to 44	[5]	Good	[10]	20	[d] 410	[1]	20	[d] 36	[1]	20	27.6	[1]
	25. plus	[4]	3.3 to 3.9	[5]	0 to 1,580	7.7	[7]	1,095	25 to 29	[6]			1,230	[d] 69	[1]	1,050	[d] 33	[1]	20	46.8	[1]
	21. plus	[7]	3.8 to 4.0	[6]	300 to 700	8.2	[7]	300	42	[8]			1,500	[d] 14	[1]	1,230	[d] 18	[1]	20	55.0	[1]
			3.67	[7]	25 to 1,400	7.4	[10]	350 to 850	24	[10]				60 to 200	[5]		10 to 30	[7]		15 to 25	[5]
			2.9	[10]	20 to 1,000	8.3	[19]	400 to 1,200	31 to 42	[11]											
					20 to 1,700	9.3	[19]														
Silicon carbide	18 to 34	[12]	3.13 to 3.22	[6]	20 to 1,100	4.5	[6]	1,095	95	[6]	Good	[13]		12.5 to 14.7	[14]				20	2.1	[13]
	13 to 35	[13]	3.17	[9]	0 to 1,700	4.3	[7]	800 to 1,200	159 to 121	[11]	do	[14]							1,350	0.9 to 2.5	[13]
			2.1 to 2.6	[13]	300 to 700	4.8	[7]	400 to 1,200	159 to 167	[12]											
			2.3 to 2.45	[14]	25 to 1,400	5.–	[13]	500 to 1,300	243 to 100	[13]											
MgO-BeO-Al_2O_3	0.04 to 0.07	[15]	3 to 3	[16]	20 to 700	7 to 10	[15]	250	[e] 4 to 12.5	[15]			25	105 to 286	[17]						
BeO-Al_2O_3-ThO_2	0.00 to 0.02	[15]	3 to 5	[16]	20 to 700	7 to 10	[15]	250	[e] 4 to 25	[15]	do	[17]	25	240 to 279	[15]	870	[f] 13	[16]	20	[f] 20	[17]
																980	[f] 6	[16]	980	[f] 17	[17]
BeO-Al_2O_3-ZrO_2	0.00 to 0.05	[15]	3	[16]	20 to 700	7 to 8	[15]	250	[g] 8 to 10	[15]	do	[17]	25	250	[15]	870	20	[16]	20	25	[17]
																980	18	[16]	980	14	[17]

[a] Little evaluation of the test methods and reported results has been made. All literature references are given in footnote c.

[b] These data are given as Watts/cm/cm²/°C. In order to convert to gram-cal/cm/sec/cm²/°C, multiply by 0.2388, and to convert to Btu in./hr/ft²/°F, multiply by 693.5.

[c] References:

[1] R. Russell, Jr., FIAT Final Report No. 647 (Dec. 1945), OTS, Dept. of Commerce, Washington, D. C.

[2] American Lava Corporation Chart No. 346.

[3] H. M. Kraner and R. A. Snyder, J. Am. Ceram. Soc. **14,** 617 (1931).

[4] H. E. White, J. Am. Ceram. Soc. **15,** 598 (1932).

[5] F. H. Riddle, SAE J. **46,** 236 (1940).

[6] Norton Company Heavy Refractories Data Sheet No. R-110-21 (May 1947).

[7] F. H. Norton, J. Am. Ceram. Soc. **8,** 709 (1925).

[8] W. J. Knapp, J. Am. Ceram. Soc. **26,** 48 (1943).

[9] National Research Council: International Critical Tables, McGraw-Hill Book Co., N.Y. (1926-33).

[10] H. N. Baumann, Jr. and A. A. Turner, J. Am. Ceram. Soc. **23,** 334 (1940).

[11] F. H. Norton, J. Am. Ceram. Soc. **10,** 30 (1927).

[12] M. L. Hartmann and O. B. Westmont, Trans. Am. Electrochem. Soc. **59,** 117 (1926).

[13] H. N. Baumann, Jr. and J. F. Swentzel, Bull. Am. Ceram. Soc. **16,** 419 (1937); evaluated data from 85 literature references.

[14] R. H. Houchins and C. McMullen, Metals & Alloys **3,** 12 (1932).

[15] R. F. Geller, P. J. Yavorsky, B. L. Steierman, and A. S. Creamer, J. Research NBS **36,** 277 (1946) RP1703.

[16] M. D. Burdick, R. E. Moreland, and R. F. Geller, NACA Tech. Note 1561 (Apr. 18, 1948).

[17] R. F. Geller and M. D. Burdick, NACA, ARR 6D24 (July 1946).

[18] R. A. Heindl, BS J. Research **10,** 715 (1933) RP562.

[19] R. F. Geller and P. J. Yavorsky, J. Research NBS **35,** 87 (1945) RP1662.

[d] E. Ryschkewitsch data obtained by very rapid loading.

[e] These values are reciprocal, multiplied by 100, of the temperature drop through a 0.50-in. height of a specimen approximately ½ in. in diameter.

[f] Values given are for a composition in this system containing an addition of 2 weight percent of titanium oxide.

[g] Values given are for compositions in this system containing additions of 2 weight percent of calcium oxide.

and there was no correction factor applied for the percentage purity of the material at any time nor for any ignition loss at 1,200° C when that loss was less than 0.01 g of the various 30- to 400-g batches. Each oxide was weighed on a semi-analytical balance to ±0.005 g. Approximately 1.2 ml of distilled water per gram of batch was added to make a slip similar in consistency to a thick cream and one drop of a 10-percent water solution of Aerosol wetting agent was added for approximately each 10 g of dry batch. The slip was machine-blunged with a chemical laboratory-type variable-speed mixer with plastic stirrers for not less than 15 min, damp-dried under infrared lamps, and completely dried in an oven at 110° C for at least 15 hr. Between 8 and 10 weight percent of a 5-percent soluble starch solution was added as a binder, and the dampened batch was mixed and sieved a number of times through a No. 30 U. S. Standard Sieve. It was then prepressed at about three-fourths of the final forming pressure to promote agglomeration, and the resultant briquets were crushed to pass either the No. 20 or the No. 30 sieve. The dampened mixture was tamped and vibrated in the molds before the final pressing. This pressing was done in case-hardened steel, and in oil-hardened, nondeforming, tool-steel molds lightly lubricated with a water-emulsifying oil.

Specimens for the softening-range and fusion tests [5] were ground from $\frac{5}{16}$ by $\frac{1}{2}$ in. diameter plaques pressed at 13,000 lb/in.^{2}. Those for the preliminary investigation of the maturing range ($\frac{3}{8}$ in. high by $\frac{3}{4}$ in. in diameter) and for the compression tests ($1\frac{1}{4}$ in. high by $\frac{3}{4}$ in. in diameter) were pressed at 9,400 lb/in.^{2}. The thermal shock and strength test bars were pressed about $\frac{5}{16}$ in. thick in a $\frac{3}{4}$-in. by $6\frac{1}{2}$-in. mold at 6,500 lb/in.^{2}.

The special high-temperature thoria-resistor furnaces used in these studies for determining vitrification ranges, for maturing the compression specimens, and for the phase studies, have been described [7, 9], as have many of the test methods [5]. These are repeated both for the convenience of the reader and to give the details of those procedures that have been revised.

Briefly, the study of the phase relations was accomplished by noting the melting characteristics of small, four-sided pyramidal specimens with an optical pyrometer and by petrographic and X-ray examinations of the nonquenched heated specimens. It must be kept in mind that equilibrium conditions at the elevated temperatures may not have been established [5] and that the phase relations suggested were based primarily on the fusion behavior observations. Along with the inherent difficulties of petrographic examination and interpretation of powder slides and thin-sections of these nonquenched specimens with high refractive indices (2.08 and 2.15 for ZrO_2 and ThO_2, respectively), there were available only very small specimens for both the petrographic and X-ray examinations.

Absorption determinations were made on specimens boiled in carbon tetrachloride, and the results were converted to equivalent water absorption values. Mature bodies were those having less than one-tenth percent of equivalent water absorption.

The length-to-diameter ratio of all compression test specimens was approximately 2. All specimen ends were ground parallel on a Blanchard grinder using diamond wheels, and the specimens were crushed between parallel-ground, $\frac{5}{8}$-in. thick, cold-rolled steel blocks at a loading rate of about 31,000 lb/in.^{2} per minute.

Following maturing of the thermal shock and rupture test bars in a high-temperature gas-fired kiln, the specimens were ground on a Blanchard grinder using diamond wheels so that the bars would be approximately $\frac{1}{4}$-in. thick with parallel faces. Ten cycles of quenching from 1,700° F (931° C) to an air-blast constituted the thermal shock test. The arrangement of the equipment for this test is shown schematically in figure 1 at "*A*". At "*B*" is an enlarged view of the specimen holder with six test bars. The bars were placed in the hot furnace (1,700° F ±5° F), heated for 30 min (the furnace reached and maintained 1,709° F for about the last 15 min), and were rapidly withdrawn to the air-blast. The orifice of the blower, delivering 625 ft^3 of room-temperature air per minute, was 4 in. in diameter and was located 6 in. above the center of the group of specimens. After remaining in the air-blast for 15 min (the specimens were only warm after about 5 min), each bar was examined for failure. The order and position of the test bars were then changed according to a schedule and were replaced in the furnace to begin the next cycle.

The modulus of rupture values in bending were determined at room temperature for both the quenched and nonquenched bars [10].

The modulus of rupture and modulus of elasticity (Young's modulus) values at 1,800° F (982° C) for the compositions studied in this investigation were determined by using a furnace designed by M. D. Burdick of this Bureau and heated by means of Globar elements. The furnace is designed to accommodate six heating elements and is intended for use at temperatures up to 2,500° F (1,371° C). The quarter-point loading formulae used for calculating the values for the modulus of rupture (M/R) and the modulus of elasticity (M/E) in bending were:

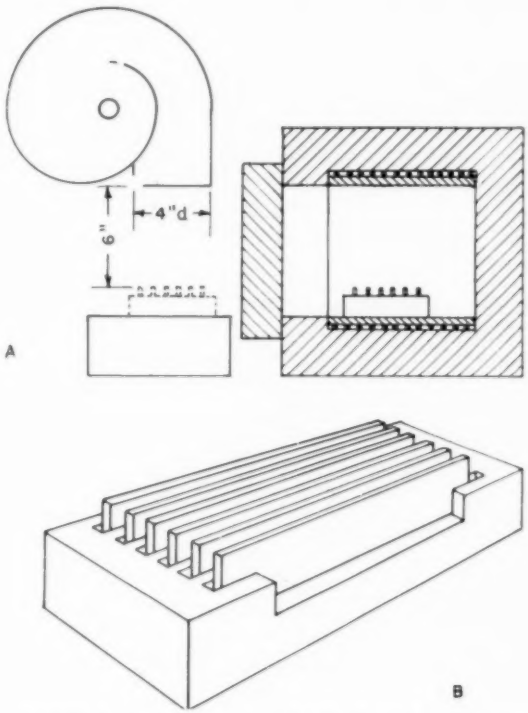

FIGURE 1. *Schematic set-up for the thermal-shock test.*

A schematic arrangement of the test specimens, furnace, and blower is shown at A, and an enlarged view of the test bars and the light-weight refractory holder is shown at B.

$$M/R=\frac{3P_1L}{4bd^2}, \tag{1}$$

and

$$M/E=\frac{P_2a(3L^2-4a^2)}{4\Delta bd^3}, \tag{2}$$

where P_1 is the total applied load, L is the span, b is the breadth at the breaking point, d is the depth at the breaking point, Δ is the deflection for any load P_2, and a is one-quarter of the span L.

The interior of the furnace is shown in figure 2. The specimen bar (A) was supported on free-titling refractory knife-edges (B), and the deflection at mid-span was measured with a ⅛-in. diameter artificial sapphire rod (C) and a calibrated gage reading to 0.0001 in. In order to eliminate any corrections due to the expansion or movement of the supporting knife-edges during the test, the gage and gage holder, outside of the furnace, were supported with two sapphire rods (D) resting on the specimen at the span points. The four elements with which the furnace was heated for these tests were spaced symmetrically about the specimen,

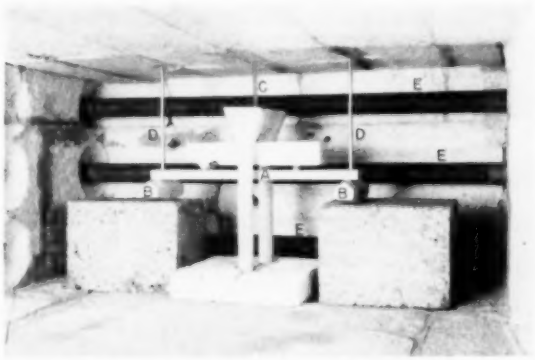

FIGURE 2. *Interior view of the furnace for rupture in bending tests.*

This photograph of the interior of the bending strength test furnace shows the test bar, A, in position for quarter-point loading. At B are shown the supporting knife-edges and the deflection at mid-span as measured with the sapphire rod, C, and a calibrated gage. This gage and the gage holder, outside of the furnace, are supported with two sapphire rods, D, resting on the specimen at the span points. Only the rear "Globar" heating elements, E, are shown.

and the temperatures were obtained with two chromel-alumel thermocouples; one located above and the other below the mid-span of the specimen. After having attained approximately equilibrium conditions in the furnace, the test bars were stressed in increments of 1,500 lb in.$^{-2}$ every 2 min, and gage deflection readings were taken every minute. When it was noted that the deflection following loading was practically constant by the end of the first minute, it was assumed that a permanent deformation, or "plastic flow", had not occurred.

IV. The System MgO-BeO-ZrO_2

1. The System MgO-BeO, Fields of Stability

The binary eutectic between MgO and BeO has been reported as being between 1,670° and 1,955° C and 50 and 48 percent of BeO [4] [11, 12, 13]. A more recent investigation [5] has shown the binary eutectic to be at 1,855° C and 48.2 percent of BeO. No compounds or mixed crystals were found.

2. The System BeO-ZrO_2, Fields of Stability

In the system BeO-ZrO_2 a simple eutectic was first reported at about 2,180° C and 65 percent of ZrO_2 [14]. The compound $3BeO.2ZrO_2$ and two eutectics at about 2,100° C and 65 and 85 percent of ZrO_2 were given in 1930 [15], but a year later a single eutectic at about 75 percent of ZrO_2 and 2,240° C was reported [16]. In the work at this Bureau [5] no evidence was found of a compound between BeO and ZrO_2.

3. The System MgO-ZrO_2

(a) Fields of Stability

The phase relations in this system are apparently complex, and many conflicting data have been given in the literature. Ruff and Ebert [17] reported two eutectics at about 26 and 80 mole percent of ZrO_2 and 1,600° and 1,550° C and the compound MgO-ZrO_2 melting at about 2,150° C. In addition, they indicated that a series of cubic mixed crystals exists between about 60 and 100 mole percent of zirconia. The first investigations of von Wartenburg and Werth produced similar results, but in a later report [15] they gave only one eutectic at about 50 mole percent of zirconia and 2,160° C and no compound formation. Ebert and Cohn [18] corroborated these later data, and in 1939 Zhirnova [19] further defined the simple eutectic at 50 mole percent (75.3 weight percent) of ZrO_2 and 2,070° C.

In the present investigation no attempt was made to redetermine the binary eutectic, but a considerable number of X-ray studies of various mixtures were made in the Constitution and Microstructure Section of this Bureau. In general, the results of this work indicate that the conclusions of Ruff and Ebert are correct in so far as the cubic isomorphous series between 60 and 100 mole percent (82 to 100%) of zirconia is concerned; but no compound of zirconia and magnesia was identified, which supports the work of Ebert and Cohn.

(b) Ceramic Bodies

Rieke and Ungewiss [20] made a number of ceramic bodies of MgO-ZrO_2 compositions, mainly for dielectric testing, and found that only one mixture (72.5% of MgO) in the range from 14 to 100 percent of magnesia showed a porosity of more than 0.1 percent at maturity. Shrinkage values were rather high, from 20 to 28 percent. The imperviousness of magnesia-zirconia compositions matured at high temperatures, 1,700° to 1,800° C, was noted also in a previous study of the thermal length changes of zirconia [9].

In this investigation only a few properties of selected body mixtures, ranging at about 10-percent intervals from 38 to 92 percent of zirconia, were determined, and these are given in table 2. All compositions between 50 and 92 percent of ZrO_2 could be matured to imperviousness at temperatures between 1,700° and 1,800° C. The 38 percent of zirconia mixture was overfired at 1,800° C and was not completely matured at 1,750° C (0.15% absorption). A complete study was not carried out because of the relatively high density of these bodies, although rather high values (29,000 to 30,000 lb/in.^{2}) were obtained for the modulus of rupture in bending at 1,800° F (982° C).

[4] All composition values are given in weight percentage, unless otherwise noted.

TABLE 2. *Some physical properties of compositions in the system* MgO-ZrO_2

Composition				Maturing range	Properties at maturity (less than 0.1 percent of water absorption)									
Mole		Weight			Properties at maximum density					Compressive strength (±5,000 lb/in.²)	Shrinkage [a]	Absorption [a]	Strength in bending at 1,800° F (982° C)	
MgO	ZrO_2	MgO	ZrO_2		Test No.	Temperature	Shrinkage	Absorption	Density				M.R.	M.E.
		%	%	°C		°C	%	%	g/cm³	lb/in.²	%	%	lb/in.²×10⁻³	lb/in.²×10⁻³
5	1	62.06	37.94	[b] 1,800	423–L	1,750	12.5	0.15						
3	1	49.54	50.46	1,700	490–L	1,700	14.9	.01	4.23	166,000	±17.93	±0.08	±28.8	±30.8
2	1	39.56	60.44	1,700 to 1,800	417–L	1,750	13.2	.00						
3	2	32.92	67.08	1,700 to 1,800	492–L	1,700	13.5	.00	4.64	208,000	±16.45	±.00		
1	1	24.65	75.35	1,700 to 1,800	451–L	1,800	15.1	.03						
1	2	14.07	85.93	1,750 to 1,800	495–L	1,750	13.8	.01	4.96	229,000	±16.60	±.03	±29.8	±23.0
1	4	7.56	92.44	1,800	422–L	1,800	12.5	.01						

[a] These values were determined for the strength in bending test bars.
[b] The composition was overfired at 1,800° C and was not completely matured at 1,750° C.
[c] These specimens were matured at 1,750° C for 1 hour in an oxy-gas furnace by the Linde Air Products Co.

4. The System MgO-BeO-ZrO_2

(a) Fields of Stability

The results of the fusion-point and softening-range determinations and of the petrographic and X-ray examinations of some of the 61 mixtures investigated are summarized in table 3. Only those considered essential to the establishment of the probable phase relations are reported. The recorded data for each mixture were obtained for the specimen that had been heated at or near the estimated liquidus or at the highest temperature when the liquidus was not reached. It must be emphasized that equilibrium may not have been attained and that the slow cooling (about 200° C per hour) in the furnace may have destroyed any evidence of the phases present at the higher temperatures.

Figure 3 is a graphic representation of the system as derived from the available data. This system is believed to be a simple one with the ternary eutectic at or near mole composition 4M:5B:3Z [5] and 1,669°±3° C. The primary phase boundaries (short-dash lines) are assumed to be essentially straight lines joining the various binary eutectics and the ternary eutectic. No evidence of compound formation was observed either with the fusion-point and softening-range determinations or with the petrographic and X-ray examinations.

The intimately mixed oxides were used without presintering for the initial observations of the melting characteristics in this system.

[5] This short form of indicating mole compositions mixtures in the ternary systems is used throughout the text. The code is M=MgO, B=BeO, Z=ZrO_2, and T=ThO_2. The short form, i.e., 4M:5B:3Z, then reads 4 moles of MgO plus 5 moles of BeO plus 3 moles of ZrO_2 and does not indicate a compound.

TABLE 3. *Results of fusion-point and softening-range observations and of petrographic and X-ray examinations of some compositions in the system* **MgO-BeO-ZrO_2**

Composition						Maximum temperature	Effect of heating *	Results of petrographic and X-ray examinations (Specimens examined were not quenched, and the phases observed may not be those in equilibrium at the maximum temperature of heating or at the liquidus)	Test No.
Mole			Weight						
MgO	BeO	ZrO_2	MgO	BeO	ZrO_2				
			%	%	%	°C	(All temperatures in °C)		
1	1	1	21.39	13.27	65.34	1,710	Fusion began at 1,688°, completed at less than 1,710°.	Cubic zirconia is the principal phase. Beryllia occurs as small angular crystals.	558
1	2	1	18.88	23.43	57.69	1,704	Fusion began at 1,689°, almost completed at 1,704°.	Beryllia occurs as blocky grains, zirconia as round grains usually cloudy from small intermixed magnesia particles.	583
1	3	1	16.90	31.46	51.64	1,765	Fusion began at 1,690°, completed at 1,765°.	Beryllia is the primary phase. Magnesia and cubic zirconia are present. X-ray: MgO, BeO, and ZrO_2—9:10 cubic.	540
1	4	2	10.42	25.87	63.71	1,886	Fusion began at 1,731°, nearly completed at 1,886°.	Beryllia is the primary phase, 40 microns and blocky, in a matrix of partially cloudy zirconia.	545
1	4	4	6.37	15.80	77.83	1,850	Fusion began at 1,770°, no noticeable change at 1,850°.	Large and small blocky beryllia crystals in a matrix of cubic and monoclinic zirconia. The ZrO_2 is cloudy from small particles, an exsolution texture. X-ray: weak MgO, BeO, and ZrO_2—9:10 cubic.	566
1	4	8	3.58	8.89	87.53	1,890	No noticeable fusion up to 1,890°.	Zirconia appears to be the primary phase.	527–L
1	5	1	13.97	43.34	42.69	1,825	Fusion began at 1,687°, completed at 1,825°.	The principal phase is beryllia. Very small inclusions in the zirconia are probably due to exsolution. X-ray: MgO, BeO, and ZrO_2—9:10 cubic.	542
1	6	3	7.20	26.80	66.00	1,850	Fusion began at 1,819°, no noticeable change at 1,850°.	Beryllia appears to be the primary phase. The zirconia has small inclusions probably having an exsolution texture.	533
1	9	2	7.88	43.99	48.13	1,925	Partial fusion at 1,925°	Beryllia is the primary phase, occurring as large as 100 microns, with cubic and monoclinic interstitial zirconia.	554–L
1	10	1	9.75	60.47	29.78	1,925	Advanced fusion at 1,925°	Large, blocky beryllia crystals occur with small interstitial zirconia grains. X-ray: MgO, BeO, and ZrO_2—2:3 cubic.	554–L
1	12	4	4.84	36.03	59.13	1,890	No noticeable fusion up to 1,890°.		528–L
1	24	1	5.28	78.59	16.13	1,890	Fusion began at 1694°, no noticeable change at 1,890°.	Principal phase is beryllia, 70 microns and blocky, with interstitial zirconia having very small inclusions. X-ray: very weak MgO, BeO, and cubic ZrO_2.	548
2	1	1	35.23	10.93	53.84	1,731	Fusion began at 1681°, completed at 1731°.	Magnesia is the primary phase occurring as flaky crystals. Zirconia crystals are cloudy and a few small beryllia crystals are seen.	565
2	5	1	24.52	38.03	37.45	1,715	Fusion began at 1,687°, almost completed at 1715°.	The principal phase is beryllia. Magnesia occurs as round grains. Interstitial zirconia occurs as small rod-shaped or as dendritic growths.	568
3	1	1	44.94	9.29	45.77	1,745	Fusion began at 1691°, almost completed at 1,745°.	Magnesia is the principal phase. Zirconia is all cubic.	571
3	5	0.4	40.96	42.36	16.68	1,800	Fusion began at 1689°, completed at 1,800°.	The principal phases are beryllia and magnesia with interstitial cubic zirconia.	559
3	5	1	32.76	33.88	33.36	1,715	Fusion began at 1689°, completed at 1715°.	Similar to composition $3MgO:5BeO:0.4ZrO_2$.	504–L
3	5	2	24.56	25.40	50.04	1,693	Fusion began at 1688°, completed at 1,693°.	Large magnesia and beryllia crystals occur in parts in a rosette matrix of dendritic zirconia and magnesia. In other parts a three-phase mosaic structure occurs. Near the eutectic but with an excess of zirconia.	552
3	5	3	19.65	20.32	60.03	1,695	Fusion began at 1690°, completed at 1695°.	The principal phases are beryllia and zirconia.	567
3	5	4	16.37	16.93	66.70	1,761	Fusion began at 1688°, completed at 1,761°.	The principal phase is zirconia. It occurs as both clear and cloudy cubic and monoclinic round crystals and as small amoeboid rods, and dendritic crystals with intermixed similarly shaped magnesia crystals.	563
3	5	8	9.82	10.16	80.02	1,890	Fusion began at 1688°, completed at 1,890°.	Zirconia occurs as the principal phase. The large round grains have an anisotropic center with the cubic form surrounding it and occasionally passing through as a band. X-ray: BeO and cubic ZrO_2.	544
3	10	1	24.47	50.61	24.92	1,777	Fusion began at 1692°, completed at 1777°.	Beryllia and magnesia occur with interstitial cubic zirconia. Beryllia appears to be the primary phase.	535
3	15	1	19.53	60.58	19.89	1,800	Fusion began at 1689°, completed at 1800°.	Beryllia is the primary phase with small interstitial magnesia and zirconia crystals.	543
3	24	1	14.32	71.09	14.59	1,915	Fusion began at 1,688°, nearly completed at 1915°.	Beryllia is the primary phase	550

See footnote at end of table.

TABLE 3. *Results of fusion-point and softening-range observations and of petrographic and X-ray examinations of some compositions in the system* MgO-BeO-ZrO_2—Continued

Composition						Maximum temperature	Effect of heating [a]	Results of petrographic and X-ray examinations (Specimens examined were not quenched, and the phases observed may not be those in equilibrium at the maximum temperature of heating or at the liquidus)	Test No.
Mole			Weight						
MgO	BeO	ZrO_2	MgO	BeO	ZrO_2				
			%	%	%	° C	(All temperatures in ° C)		
3	40	1	9.72	80.38	9.90	1,850	Fusion began at 1,680°, partial fusion up to 1850°.	Beryllia is the primary phase. X-ray: MgO, BeO, and cubic ZrO_2.	594
4	5	2	30.27	23.48	46.25	1,697	Fusion began at 1690°, completed at 1,697°.	The principal phases are magnesia and beryllia with small intergrowth crystals of magnesia and zirconia.	577
4	5	3	24.59	19.07	56.34	1,693	Fusion began at 1689°, completed at 1,693°.	Magnesia, beryllia, and zirconia occur as about 30 micron single crystals in a matrix of small, 5 micron and less, intermixed crystals of the same three phases. This is at or near the eutectic composition.	555
5	5	3	28.95	17.97	53.08	1,697	Fusion began at 1,690°, almost completed at 1,697°.	Magnesia occurs in parts in a rosette matrix of the three constituents. In other parts a three phase mosaic structure is present, near the eutectic but with an excess of magnesia.	585
5	24	1	21.79	64.89	13.32	1,911	Fusion began at less than 1,693°, partial fusion up to 1,911°.	Beryllia is the primary phase	572
5	48	1	13.22	78.705	8.075	1,855	Fusion began at 1,692°, partial fusion up to 1,855°.	Similar to composition 5MgO:24BeO:1ZrO_2	573
6	5	1	49.35	25.52	25.13	1,783	Fusion began at 1,690°, partial fusion up to 1,783°.	Magnesia and beryllia are the principal phases with rare interstitial small crystals of zirconia.	569
6	10	3	28.08	29.03	42.89	1,704	Fusion began at 1,689°, completed at 1,704°.	Round magnesia and blocky beryllia crystals occur in a matrix of small zirconia crystals intermixed with similar magnesia and beryllia crystals.	580
6	10	5	21.83	22.58	55.59	1,695	Fusion began at 1,688°, nearly completed at 1,695°	Beryllia is the principal phase in a matrix of small (5 microns and less) intermixed magnesia, beryllia, and ireonia crystals, near the eutectic and with an excess of beryllia.	575
15	5	1	70.89	14.67	14.44	1,860	Fusion began at 1,690°, partial fusion up to 1,860°.	Magnesia is the primary phase	570
0.28	10	1	3.00	65.00	32.00	1,925	No noticeable fusion up to 1,925°.	Beryllia occurs with interstitial cloudy zirconia grains. X-ray: very weak MgO, BeO, and ZrO_2—9/10 cubic.	554-L
1	10	3	5.00	50.00	45.00	1,925	No noticeable fusion up to 1,925°.	Very similar to weight composition 3MgO+65BeO+32ZrO_2	554-L
3	5	2	24.56	25.40	50.04	[b] 1,691	Fusion began at 1,679°, completed at 1,691°.[b]	Beryllia is the primary phase in a matrix of very small intermixed magnesia and zirconia crystals. X-ray: MgO, BeO, and cubic ZrO_2.	602[b]
4	5	3	24.59	19.07	56.34	[b] 1,683	Fusion began at 1,669°, completed at 1,683°.[b]	Same as composition 4MgO:5BeO:3ZrO_2 (Test No. 555)	617[b]

[a] In most cases, the beginning of fusion as indicated is for the test of the specimen described and is usually within 2° C of the average value obtained for three or more determinations of the same composition. The term "complete fusion" means that the pyramidal specimen had fused sufficiently to flow into a flat button shape and does not necessarily connote that the mixture had completely liquefied.

[b] These compositions were presintered at 1,670° C for 30 min, crushed, and reformed before the fusion-point and softening-range determinations were made.

An attempt to identify the ternary eutectic solely by microscopic examination and subsequent interpretation was only partially successful. The most that could be done was to identify an area in which the specimens examined contained no distinguishable primary phases and which were composed mainly of a regular mosaic type structure. The area (fig. 3) so defined is bounded by the compositions 3M:5B:2Z, 1M:2B:1Z, 3M:5B:4Z, 1M:1B:1Z, and 5M:5B:3Z.

In order to determine the ternary eutectic more accurately, a number of compositions were presintered at 1,670° C for 30 min and ground in mullite and boron carbide mortars to pass the No. 325 U. S. Standard Sieve. This finely divided material was then pressed, shaped, and tested according to the procedures given previously. The results of tests on two of these presintered compositions are included at the end of table 3. It was noted that the temperature at which fusion began for the presintered ternary eutectic mixture was 20° C lower than that for the unsintered mixture.

An area of possible solid solution is suggested for this system extending along the BeO-ZrO_2 join from about 5 percent to about 85 percent of BeO

and bounded by, but excluding, compositions 1M:24B:1Z, 1M:10B:1Z, 1M:5B:1Z, 3M:5B:4Z, and 3M:5B:8Z. This area is shown on the diagram enclosed by a long-dash line. In this area there may be at least two phases containing limited amounts of the end members in solid solution. The ends of the line approximate the limits of solid solubility. Although the differences in the refractive index values between MgO and BeO and ZrO_2 are appreciable, petrographic examination failed to reveal any changes in these values, and only occasionally were the indices of the cubic form of ZrO_2 [9] found. In the compositions 1M:6B:3Z and 1M:4B:4Z, however, a very definite exsolution texture was seen, although the crystals of lower refractive index than zirconia were too small to be sufficiently resolved by the microscope for complete optical identification. The appearance of this exsolution texture is similar to that seen in specimens of the MgO-BeO-ThO system, but the texture is of much finer grain size. The appearance of lines for cubic ZrO_2 in the X-ray patterns is not necessarily an indication of ternary solid solution, but rather the expected form of ZrO_2 in the presence of magnesia [9, 19].

(b) Ceramic Bodies

The only available literature information on ceramic bodies in this system [21, 22] is concerned mainly with modifying the thermal expansion characteristics of zirconia by the addition of small amounts of the other oxides.

Impervious bodies may be made from compositions in approximately one-half of the ternary diagram area. The compositions of these bodies

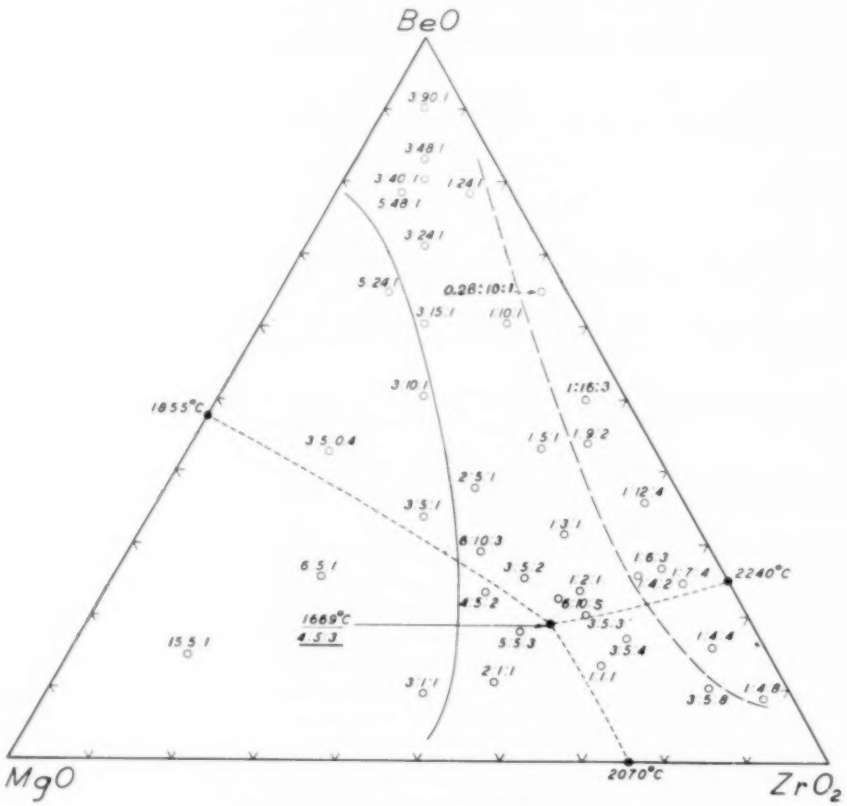

FIGURE 3. *The system* MgO–BeO–ZrO_2.

This figure gives the location of the primary phase boundaries (short-dash lines), a suggested area of solid solution (long-dash lines), and the range of compositions from which impervious porcelain bodies may be made (to the right of the solid line). Compositions are indicated in molar ratios but are graphically placed according to weight percentages. Twenty-two additional mixtures, not reported, were investigated in the eutectic area.

lie to the right of the solid line shown in figure 3 and could usually be matured between 1,450° and 1,600° C. Table 4 gives the results of the maturing range studies and the values of porosity and shrinkage at maximum density. Those bodies that could be matured to a practically impervious condition over a range of 50° C or more have absorption values averaging about 0.02 percent and shrinkage values ranging from 15 to 21 percent.

Compressive strength values (table 4) ranged from 164,000 to 264,000 lb/in.^{2} for these porcelains, and the outstanding body in these tests was 1M:24B:1Z (264,000 lb/in.^{2}). The maturing range of this porcelain was considerable (1,450° to 1,600° C), and its density (3.25 g/cm^3) was one of the lowest observed. The table gives some comparative compression results for three body compositions similarily fabricated but matured in a gas-fired furnace.

TABLE 4. *Maturing range studies and compressive strength results of some compositions in the system* MgO-BeO-ZrO_2

Composition						Maturing [a] [b] range	Properties [b]				Properties of compressive strength specimens [d]						
Mole			Weight				Test No.	Temperature	Shrinkage	Absorption	Test No.	Temperature	Shrinkage	Absorption	Density	Height/diameter [c]	Strength [e] at room temp. (±5,000 lb./in.^{2})
M	B	Z	MgO	BeO	ZrO_2												
			%	%	%	°C		°C	%	%		°C	%	%	g/cm^3		n X10^3
1	1	1	21.39	13.27	65.34	1,500 to 1,550	519–L	1,500	18.03	0.03	549–L	1,500	14.42	0.01	4.46	1.93	225
1	3	1	16.90	31.46	51.64	1,450 to 1,600	470–L	1,600	18.07	.00	507–L	1,600	14.61	.02	3.87	1.97	204
1	4	2	10.42	25.87	63.71	1,450 to 1,600	471–L	1,550	17.59	.00	508–L	1,550	17.94	.00	4.48	1.96	259
1	4	4	6.37	15.80	77.83	1,500 to 1,600	471–L	1,550	16.96	.00	509–L	1,550	16.98	.01	4.81	1.98	234
1	5	1	13.97	43.34	42.69	1,450 to 1,600	470–L	1,600	18.86	.00	510–L	1,600	18.42	.03	3.9	1.83	231
1	6	3	7.20	26.80	66.00	1,500 to 1,600	516–L	1,600	17.56	.01	530–L	1,600	16.35	.00	4.37	1.94	249
1	6	3	7.20	26.80	66.00	1,500 to 1,600	.....	.....	.....	...	6/16/44	1,600	.....	.01	4.37	1.08	[f] [g] 243
1	6	3	7.20	26.80	66.00	1,500 to 1,600	.....	.....	.....	...	7/25/44	1,550	.....	.00	4.30	1.93	[f] [g] 262
1	7	4	5.69	24.73	69.58	.....	.....	.....	.....	...	7/15/44	1,600	.....	.00	4.49	1.92	[f] [g] 207
1	7	4	5.69	24.73	69.58	.....	.....	.....	.....	...	7/25/44	1,550	.....	.05	4.22	1.90	[f] [g] 241
1	10	1	9.75	60.47	29.78	1,450 to 1,600	473–L	1,500	19.46	.01	512–L	1,500	18.91	.04	3.47	1.97	220
1	24	1	5.28	78.59	16.13	1,450 to 1,600	.....	1,500 to 1,600	19.4	.00	513–L	1,550	19.55	.01	3.25	1.91	264
2	1	1	35.23	10.93	53.84	1,550	517–L	1,550	17.24	.05	531–L	1,550	15.03	.01	4.40	1.86	206
2	5	1	24.52	38.03	37.45	1,500 to 1,550	519–L	1,500	18.19	.07	532–L	1,500	16.29	.02	3.73	1.95	215
3	5	2	24.56	25.40	50.04	1,500	519–L	1,500	17.56	.02	526–L	1,500	15.60	.02	4.05	1.96	208
3	5	3	19.65	20.32	60.03	1,500 to 1,600	313–L	1,600	15.2	.01	514–L	1,600	16.18	.01	4.38	1.92	202
3	5	8	9.82	10.16	80.02	1,550	475–L	1,550	15.56	.01	515–L	1,550	15.17	.01	4.80	1.92	220
3	5	8	9.82	10.16	80.02	1,550	.....	.....	.....	...	7/25/44	1,550	.....	.00	4.81	1.89	[f] [g] 238
3	15	1	19.53	60.58	19.89	1,500 to 1,600	319–L	1,550	19.1	.05	502–L	1,550	17.38	.05	3.31	1.97	164
3	24	1	14.32	71.09	14.59	1,450	491–L	1,450	17.4	.06	545–L	1,450	16.50	.05	3.23	1.95	242
3	40	1	9.72	80.38	9.90	1,500 to 1,600	313–L	1,600	20.6	.03	522–L	1,600	19.01	.01	3.18	2.00	222
3	48	1	8.37	83.10	8.53	1,450 to 1,550	493–L	1,500	19.15	...	550–L	1,500	18.20	.04	3.07	2.02	229
3	90	1	4.74	90.32	4.94	1,450 to 1,550	499–L	1,550	19.5	.02	524–L	1,550	19.07	.02	2.97	2.08	172
5	48	1	13.22	78.705	8.075	1,450 to 1,550	491–L	1,450	19.62	.05	.....	.....	.....	...	.....	.....	.....

[a] Overfiring and underfiring occurred at 50 deg C above and at 50 deg C below the temperature ranges given.
[b] Values obtained for specimens matured in an electric furnace for 1 hour at the temperature specified.
[c] Specimens about 1 in. high by ½ in. in diameter.
[d] Unless otherwise indicated, the values given are the averages for three test specimens.
[e] Compression testing was done at a constant loading rate of 31,250 lb/in.^{2} per min, using cold-rolled steel contact blocks.
[f] Values obtained for specimens matured in a gas-fired furnace.
[g] Value given is for one specimen only.

Nine body compositions were selected to represent the relative resistance to thermal shock, and strengths in bending at room and at elevated temperature, of the refactory porcelains in the system. Table 5 gives the data for these properties and also includes some values of the modulus of rupture and Young's modulus for a few bodies tested at 1,900° F (1,038° C) and 2,000° F (1,093° C). As expected, the high-beryllia bodies were the most resistant to thermal quenching, and the high-zirconia bodies either did not survive the heat-shock test or were very easily broken by finger pressure alone after testing. Generally, the rupture values of the high-beryllia bodies were slightly higher after shocking than those obtained for unshocked specimens. The values for the modulus of rupture in bending at room temperature for the high-beryllia bodies ranged from 13,000 to 20,000 lb/in.^{2}, and from 23,000 to 39,000 lb/in.^{2} for the high-zirconia bodies. Modulus of rupture and modulus of elasticity (Young's modulus) values in bending at 1,800° F for the high-beryllia bodies ranged from 13,000 to 18,000 lb/in.^{2} and 38,000,000 to 34,000,000 lb/in.^{2}, respectively, and for the high-zirconia bodies the values were from 21,000 to 35,000 lb/in.^{2} and from 31,000,000 to 15,000,000 lb/in.^{2}, respectively. It is interesting to note that, at 1,800° F, the Young's moduli values decrease as the moduli of rupture values increase.

TABLE 5. *Resistance to thermal shock and rupture and elastic strength values of some compositions in the system* MgO-BeO-ZrO_2

Composition						Maturing data [a]			Resistance to thermal shock [b] (2 bars each composition)	Strength in bending values [c]					
Mole			Weight			Test No.	Temperature	Absorption		M/R at room temperature [d] (±2,000 lb/in.^{2})	M/R at room temperature after shocking [e] (±2,000 lb/in.^{2})	M/R at elevated temperatures [f] (±2,000 lb/in.^{2})		Young's Modulus at elevated temperatures [f] (±3,000,000 lb/in.^{2})	
M	B	Z	MgO	BeO	ZrO_2							Temperature	Value	Temperature	Value
			Wt %	*Wt %*	*Wt %*		*° C*	*Wt %*		*n×10³ lb/in.²*	*n×10³ lb/in.²*	*° F*	*n×10³ lb/in.²*	*° F*	*n×10⁶ lb/in.²*
1	5	1	13.97	43.34	42.69	22–R	1,625	0.03	Cracked on 3d and 4th cycle.	23.1		1,800	20.7	1,800	31.3
1	6	3	7.20	26.80	66.00		1,600	[b] 0.00	Broke on 3d and 4th cycle.[b]	[b] 38.6		1,800	[bk]30.9	1,800	[bk]22.7
1	6	3	7.20	26.80	66.00		1,600	[b] 0.00				1,900	[b]34.1	1,900	[b]10.6
1	6	3	7.20	26.80	66.00		1,600	[b] 0.00				2,000	[bk]32.8	2,000	[bk]11.8
1	7	4	5.69	24.73	69.58		1,600	[b] 0.03	One of five test specimens [b] broke on 8th cycle	[b] 28.2		1,800	[bk]24.5	1,800	[bk]19.7
1	7	4	5.69	24.73	69.58		1,600	[b] 0.03				2,000	[b]28.9	2,000	[b]13.2
1	10	1	9.75	60.47	29.78	8–R	[g] 1,600	.02		21.7	23.3	1,800	18.9	1,800	33.8
3	5	3	19.65	20.32	60.03		1,600	[b] 0.02	Two of ten test specimens were easily broken after 10th cycle. [b]	[b] 26.3	[b] 29.2	1,800	[b]31.8	1,800	[b]16.9
3	5	3	19.65	20.32	60.03		1,600	[b] 0.01				1,900	[b]24.0	1,900	[b] 9.7
3	5	8	9.82	10.16	80.02		1,600	[b] 0.03	Two of eleven test specimens were easily broken after 10th cycle.[b]	[b] 24.5	[b] 25.6	1,800	[b]25.8	1,800	[b]19.6
3	5	8	9.82	10.16	80.02		1,600	[b] 0.00				1,900	[b]33.8	1,900	[b]14.4
3	5	8	9.82	10.16	80.02		1,600	[b] 0.00				2,000	[b]32.7	2,000	[b] 5.4
3	24	1	14.32	71.09	14.59	14–R	1,550	.15	No failure	20.1	20.4	1,800	18.4	1,800	34.1
3	40	1	9.72	80.38	9.90	13–R	[g] 1,650	.4	do	12.6	13.2	1,800	13.1	1,800	38.0
3	90	1	4.74	90.32	4.94	25–R	[h] 1,625 1,600	1.0	do	15.3	14.3	1,800	12.6	1,800	38.4

[a] All test specimens were matured in a gas-fired furnace at the temperature indicated for 1 hour unless otherwise specified.
[b] Ten cycles of test from 1,700 °F to room temperature air blast for two test specimens, about 5½ in. by ¾ in. by ¼ in., of each composition.
[c] M/R is the modulus of rupture.
[d] Two specimens, ca. 5½ in. by ¾ in. by ¼ in., of each composition were tested.
[e] Only those specimens that survived 10 cycles of heat shocking were tested.
[f] Three specimens, ca. 5½ in. by ¾ in. by ¼ in., of each composition were tested unless otherwise specified.
[g] Matured 2 hours.
[h] For preliminary report see reference [2].
[i] Quenched from 1,500 °F.
[j] One specimen tested.
[k] Two specimens tested.
[l] Matured for 1 hour at each of these temperatures.

V. The System MgO–BeO–ThO_2

1. The System MgO–ThO_2, Fields of Stability

Von Wartenburg and Prophet [11] describe the system MgO-ThO_2 as having no melting below 2,500° C.

2. The System BeO–ThO_2, Fields of Stability

A simple system of one eutectic at about 20 percent of BeO and 2,200° C was reported by von Wartenburg and coworkers [13].

3. The System MgO–BeO–ThO_2

(a) Fields of Stability

The results of the fusion-point and softening-range determinations and of the petrographic and X-ray examinations of some of the mixtures investigated are summarized in table 6. Only those considered essential to the establishment of the probable phase relations are reported. The recorded data for each mixture were obtained for the specimen that had been heated at or near the estimated liquidus or at the highest temperature when the liquidus was not reached. It will bear repeating that equilibrium may not have been attained and that the slow cooling (about 200° C per hour) in the furnace may have destroyed any evidence of the phases present at the higher temperatures.

Figure 4 is a graphic representation of the system as derived from the available data. This system is believed to be a simple one with the ternary eutectic at or near mole composition 5M:10B:1T and 1,797° ±5° C. The primary phase boundaries (short dash lines) are assumed to be essentially straight lines joining the various binary eutectics and the ternary eutectic. The boundary line between the ternary eutectic and the MgO-ThO_2 eutectic is shown partially drawn, approximating the results of this investigation. No evidence of compound formation was observed either with the fusion-point and softening-range determinations or with petrographic and X-ray examinations.

TABLE 6. *Results of fusion-point and softening-range observations and of petrographic and X-ray examinations of some compositions in the system* MgO-BeO-ThO_2

Composition						Maximum temperature	Effect of heating [a] (All temperatures in ° C)	Results of petrographic and X-ray examinations [b] (Specimens examined were not quenched and the phases observed may not be those in equilibrium at the maximum temperature of heating or at the liquidus)	Test No.
Mole			Weight						
MgO	BeO	ThO_2	MgO	BeO	ThO_2				
			%	%	%	°C			
2	7	1	15.51	33.69	50.80	1,832	Fusion began at 1,801°, completed at 1,832°.	Beryllia is the primary phase and occurs with interstitial cubic and rounded magnesia and thoria. Some thoria occurs as exsolution from beryllia. X-ray: weak MgO and BeO and very strong ThO_2.	653
2	10	1	13.56	42.05	44.39	1,871	Fusion began at 1,798°, advanced fusion at 1,871°.	Similar to composition 2MgO:7BeO:1ThO_2, except that the X-ray shows medium strong ThO_2.	654
2	15	1	11.20	52.12	36.68	1,870	Fusion began at 1,790°, slight fusion at 1,870°.	Similar to composition 2MgO:7BeO:1ThO_2, except for relative amount of beryllia by petrographic examination.	658
2	25	1	8.31	64.47	27.22	1,910	Fusion began at 1,801°, slight fusion at 1,910°.	Beryllia occurs as round grains with thoria as exsolution in major amounts in a restricted portion of the grain. Thoria also occurs interstitially. X-ray: medium strong ThO_2, strong BeO, and very weak MgO.	677
3	28	4	6.44	37.31	56.25	1,900	Fusion began at about 1,795° to 1,800°, no further fusion up to 1,900°.	An exsolution texture of thoria from beryllia in practically all beryllia crystals. X-ray: strong ThO_2, weak BeO, and very weak MgO.	659
5	10	1	28.16	34.95	36.89	1,814	Fusion began at 1,797°, completed at 1,814°.	Beryllia crystals contain both magnesia and thoria inclusions as spheres and dendritic crystals mostly as an intergrowth structure. This is near the ternary eutectic. X-ray: strong ThO_2 and weak MgO and BeO.	671
6	4	1	39.92	16.51	43.57	1,839	Fusion began at 1,813°, completed at less than 1,839°.	Magnesia is the primary phase. Thoria occurs as dendritic inclusions in very large, 300 micron, beryllia crystals.	645
6	9	2	24.31	22.62	53.07	1,818	Fusion began at 1,802°, almost completed at 1,815°.	Thoria appears to be the principal phase. It also occurs occasionally as an exsolution from beryllia. See photomicrograph of a selected section of this specimen in figure 5.	635

See footnotes at end of table.

TABLE 6. *Results of fusion-point and softening-range observations and of petrographic and X-ray examinations of some compositions in the system* MgO-BeO-ThO_2—Continued

Composition						Maximum temperature	Effect of heating [a] (All temperatures in ° C)	Results of petrographic and X-ray examinations [b] (Specimens examined were not quenched and the phases observed may not be those in equilibrium at the maximum temperature of heating or at the liquidus)	Test No.
Mole			Weight						
MgO	BeO	ThO_2	MgO	BeO	ThO_2				
			%	%	%	°C			
6	10	1	31.99	33.09	34.92	1,822	Fusion began at 1,803°, almost completed at 1,822°.	The primary phase could not be determined. Beryllia occurs as large crystals, some with intergrowth of dendritic thoria, magnesia as round or cube-shaped crystals, and thoria as small spheres and dendritic crystals.	646
6	10	3	18.83	19.48	61.69	1,819	Fusion began at 1,805°, completed at about 1,819°.	The primary phase, thoria, occurs as spheres and as dendritic rods in a matrix of beryllia.	636
6	20	1	24.04	49.72	26.24	1,814	Fusion began at 1,803°, completed at 1,814°.	Beryllia appears to be the primary phase. The interstitial material consists of dendritic thoria in an intergrowth texture with small magnesia and beryllia crystals.	638
6	42	1	15.54	67.50	16.96	1,916	Fusion began at 1,790°, nearly completed at 1,916°.	Beryllia is the primary phase and occurs with thoria inclusions clustered in one area of each crystal as an exsolution texture (fig. 5). X-ray: strong BeO, medium strong ThO_2, and weak MgO.	657
6	78	1	9.84	79.41	10.75	1,902	Fusion began at about 1,792°, slight fusion at 1,902°.	Similar to composition $6MgO{:}42BeO{:}1ThO_2$. The beryllia crystals are larger. X-ray: very weak MgO, others are the same as above.	675
7	10	1	35.43	31.41	33.16	1,823	Fusion begun at 1,799°, almost completed at 1,823°.	Magnesia appears to be the primary phase	638-I.
12	10	1	48.47	25.07	26.46	1,826	Fusion began at 1,797°, completed at 1,826°.	Magnesia is the primary phase. The crystal sizes of the three components average about 40 microns.	666
12	42	1	26.90	58.42	14.68	1,820	Fusion began at 1,797°, completed at 1,820°.	Beryllia is the primary phase and contains an intergrowth of dendritic thoria. Magnesia appears interstitially and as inclusions in some beryllia crystals. X-ray: strong ThO_2, medium strong BeO, and very weak MgO.	669
12	78	1	17.93	72.29	9.78	1,860	Fusion nearly completed at 1,860°.	The principal phase is beryllia occuring as round grains having exsolution thoria inclusions in selected areas of the crystal. X-ray: medium strong BeO and weak MgO and ThO_2.	663
30	42	1	47.91	41.63	10.46	1,848	Fusion began at 1,802°, completed at 1,848°.	Magnesia occurs as large cubes and as striations across and through some beryllia crystals indicating proximity to a phase boundary with magnesia as the probable principal phase.	667
30	120	1	27.02	67.08	5.90	1,842	Fusion began at 1,801°, completed at 1,842°.	Beryllia is the principal phase and occurs as large round and blocky crystals usually having exsolution thoria inclusions. X-ray: medium strong MgO and BeO and weak ThO_2.	674

[a] In most cases the beginning of fusion as indicated is for the test of the specimen described and is usually within 2° C of the average value obtained for three or more determinations of the same composition. The term "complete fusion" means that the pyramidal specimens had fused sufficiently to flow into a flat button shape and does not necessarily connote that the mixture had completely liquefied.

[b] Many of the petrographic descriptions given are illustrated in the photomicrographs of figure 5.

All compositions for the fusion-point and softening-range determinations reported in this system were presintered at 1,750° C for 30 min and ground in mullite and boron carbide mortars to pass the No. 325 U. S. Standard Sieve. This finely divided material was then pressed, shaped, and tested according to the procedures previously described.

The location and temperature of the ternary eutectic of this system were based almost entirely upon the data obtained from the fusion-point and softening-range observations, because petrographic examinations failed to reveal even an area surrounding the probable ternary eutectic as was found for the zirconia system. In addition, many of the specimen compositions in all sections of the diagram showed both a mosaic and a dendritic type structure as seen in the photomicrographs, *A* and *B* of figure 5. The dendritic structure practically always occurred at an unmeasured depth in those surfaces exposed to the furnace atmosphere, and the mosaic structure usually constituted the remainder of the thin-section specimen. The photomicrographs also give an indication of the relative difficulty in distinguishing small or large crystals of either magnesia or beryllia without polarized light.

FIGURE 4. *The system* MgO-BeO-ThO_2.

This figure gives the location of the primary phase boundaries (short-dash lines), a suggested area of solid solution (long-dash lines enclosing the BeO apex area), and the range of compositions from which impervious bodies may be made (similar to the solid solution area). Compositions are indicated on the figure in molar ratios but are graphically placed according to weight percentages. Eight additional mixtures, not reported, were investigated in the eutectic area.

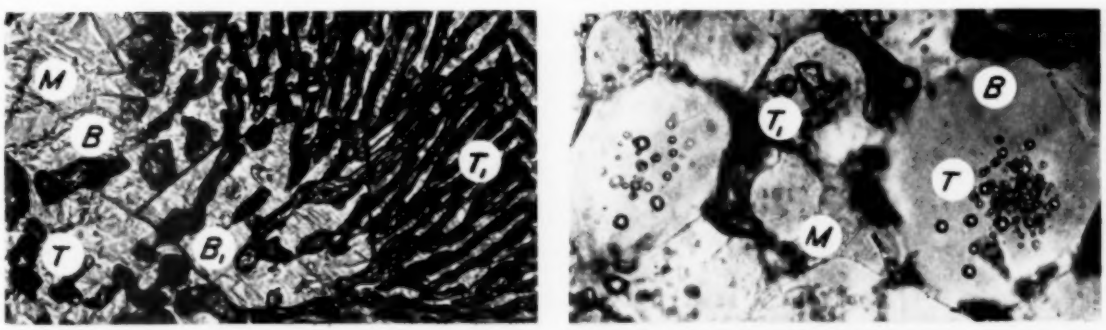

FIGURE 5. *Thin-section photomicrographs of two fused compositions of the system* MgO-BeO-ThO_2.

Photomicrograph A of mole composition 6MgO:9BeO:2ThO_2, ×300, Test No. 635—1,818° C, shows typical thoria crystals at T, the high relief dendritic thoria at T_1, a typical beryllia crystal at B, the dendritic thoria inclusion structure in a large beryllia crystal at B_1 (outlined), and the typical appearance of magnesia at M. In photomicrograph B of mole composition 6MgO:42BeO:1ThO_2, ×340, Test No. 657—1,916° C, the high relief material T is a typical thoria exsolution texture from beryllia (the large, almost clear round crystal B). Shown also are a magnesia crystal M and a few high relief thoria crystals T_1.

Because of the apparent highly viscous nature of compositions in this system at high temperatures, there still remains considerable doubt whether the ternary eutectic may be located more accurately than in the area (fig. 4) bounded by the compositions 7M:10B:1T, 5M:10B:1T, and 6M:9B:2T. The fusion-point and softening-range tests, however, indicate it to be near mole composition 5M:10B:1T and 1,797° ±5° C.

An area of possible solid solution is suggested for this system to be bounded by and to include compositions 12M:78B:1T, 6M:42B:1T, 2M:10B:1T, and 3M:28B:4T. This area is shown on the diagram enclosed by a long-dash line. The X-ray examinations failed to reveal any shift in the *d*-spacing values, and the petrographic examinations failed to reveal any differences in refractive index values of the component oxides, although a definite exsolution texture (photomicrograph *B* of fig. 5) was noted in all compositions within the area. Examination of the softening-range observations (not all of which are included in table 6) shows that the liquidus temperatures of the compositions located in the central portion of the diagram are between 1,814° and 1,840° C and that, at the proposed solid solution boundary, there occurs a large increase in these temperatures. Within the solid solution area, the mixtures of the compositions 12M:78B:1T, 6M:42B:1T, 2M:15B:1T, 2M:10B:1T, and 3M:28B:4T show only very limited melting in the temperature range from 1,870° to 1,915° C, whereas those mixtures just outside of the area, 30M:120B:1T, 12M:42B:1T, 6M:30B:1T, 6M:20B:1T, and 2M:7B:1T, are completely melted in the temperature range from 1,812° to 1,842° C.

It is believed that the very viscous nature at high temperatures of the mixtures in this region has obscured to an appreciable extent the expected increase in the solidus temperatures associated with the solid solution phenomena. All of the available data seems to indicate that the suggested solid solution area is one that exists only at high temperatures, and that the solid solution is not present after slow cooling, which apparently destroys all evidence of the existence in the specimens of the high-temperature form.

(b) Ceramic Bodies

It is possible to produce impervious porcelains from compositions in approximately one-half of the beryllia field of this system. These bodies, whose compositions are confined to the solid solution area, could usually be matured between 1,500° and 1,750° C. Table 7 gives the results of the maturing range studies and the values of absorption and shrinkage at maximum density. Those porcelains that could be matured to a practically impervious condition over a range of 50° C or more have shrinkage values ranging from 18 to 21 percent and absorption values averaging about 0.02 percent.

Compressive strength values (table 7) ranged from 165,000 to 265,000 lb/in.^{2} for these bodies. The outstanding porcelain from the standpoint of compressive strength was 3M:28B:4T (265,700 lb/in.^{2}), but its maturing range is relatively short (1,600° to 1,650° C) and its density (4.91g/cm^3) was the highest observed.

It had been found previously [5] that thoria-containing bodies were extremely brittle and usually possessed rather poor heat-shock resistance. For practical purposes it was, therefore, considered sufficient to determine the relative thermal-shock resistance and the strength in bending at room and at elevated temperatures for only a few body compositions selected to represent the maturable area of the system.

As had been expected, none of the bodies tested (table 8) were satisfactory in their resistance to thermal shocking (all were either cracked or could easily be broken after testing) nor could their strengths in bending at room temperature (9,000 to 14,000 lb/in.^{2}) be considered as more than fair to poor. Modulus of rupture and modulus of elasticity (Young's modulus) values in bending at 1,800° F (982° C), ranged from 13,000 to 16,000 lb/in.^{2} and from 40,000,000 to 32,000,000 lb/in.^{2}, respectively. The higher values for the tests at 1,800° F as compared to those obtained for the room-temperature tests may have been due to the incomplete maturing of all but one of the test bars. The values obtained for body composition 2M:42B:1T, which was completely matured, were slightly lower for the 1,800° F test.

TABLE 7. *Maturing range studies and compressive strength results of some compositions in the system* MgO-BeO-ThO_2

Composition						Maturing [a, b] range	Properties [b]				Properties of compressive strength specimens [b, c]						
Mole			Weight				Test No.	Temperature	Shrinkage	Absorption	Test No.	Temperature	Shrinkage	Absorption	Density	Height/diameter [d]	Strength [e] at room temperature (±5,000 lb/in.²)
M	B	Z	MgO	BeO	ZrO_2												
			%	%	%	°C		°C	%	%		°C	%	%	g/cm³		n×10³ lb/in.²
2	10	1	13.56	42.05	44.39	1,650 to 1,750	323–L	1,700	18.7	0.02	626–L	1,700	18.47	0.05	4.42	1.91	203
2	15	1	11.20	52.12	36.68	1,600 to 1,750	329–L	1,750	19.8	.00	618–L	1,750	18.25	.06	3.96	1.96	187
2	25	1	8.31	64.47	27.22	1,500 to 1,700	487–L	1,600	19.46	.01	610–L	1,625	19.10	.01	3.66	1.97	253
2	42	1	5.78	75.30	18.92	1,500 to 1,650	584–L	1,600	19.36	.02	616–L	1,625	19.42	.01	3.40	1.94	185
3	28	4	6.44	37.31	56.25	1,600 to 1,650	585–L	1,650	17.28	.01	611–L	1,675	17.99	.01	4.91	1.88	206
6	42	1	15.54	67.50	16.96	1,550 to 1,700	487–L	1,600	19.30	.01	609–L	1,625	19.3	.01	3.43	2.00	230
6	78	1	9.84	79.41	10.75	1,550 to 1,750	323–L	1,700	21.1	.02	613–L	1,700	19.90	.01	3.25	1.97	250
6	120	1	6.89	85.58	7.53	1,650 to 1,750	....	1,700 to 1,750	20.6	.00	615–L	1,725	19.6	.01	3.15	1.99	235
6	200	1	4.39	90.82	4.79	1,450 to 1,700	575–L	1,600	19.20	.01	619–L	1,625	19.8	.01	3.03	1.99	251
12	78	1	17.93	72.29	9.78	1,550 to 1,700	578–L	1,600	17.92	.02							
30	200	1	18.67	77.25	4.08	1,550 to 1,700	578–L	1,600	18.08	.02	614–L	1,625	19.5	.03	3.10	1.95	166
30	300	1	13.47	83.59	2.94	1,500 to 1,700	571–L	1,650	18.40	.01	612–L	1,675	19.8	.01	3.07	1.93	242

[a] Overfiring and underfiring occurred at 50 deg C above and 50 deg C below the temperature ranges given.
[b] Values obtained for specimens matured in an electric furnace for one hour at the temperature given.
[c] The values given are the averages for three test specimens.
[d] Specimens about 1 in. high by ½ in. in diameter.
[e] Compression testing was done at a constant loading rate of 31,250 lb/in.² per min until failure, using cold-rolled steel contact blocks.

TABLE 8. *Resistance to thermal shock and rupture and elastic strength values of some compositions in the system* MgO-BeO-ThO_2

Composition						Maturing data [a]			Resistance to thermal shock [b] (2 bars each composition) [c]	Strength in bending values [c]			
Mole			Weight			Test No.	Temperature	Absorption		M/R at room temperature [d] (±2,000 lb/in.²)	M/R at room temperature after shocking (±2,000 lb/in.²)	M/R at 1,800° F [e] (±2,000 lb/in.²)	Young's Modulus at 1,800° F [e] (±3,000,000 lb/in.²)
M	B	T	MgO	BeO	ThO_2								
			%	%	%		°C	%		n×10³ lb/in.²	n×10³ lb/in.²	n×10³ lb/in.²	n×10⁶ lb/in.²
2	15	1	11.20	52.12	36.68	21–R	1,800	0.40	Cracked on 2d cycle	11.7		15.6	31.9
2	42	1	5.78	75.30	18.92	23–R	1,700	.07	Cracked on 3rd cycle	13.8		13.3	34.9
6	78	1	9.84	79.41	10.75	....	Cone 31	[g] 5.9	....	....	....	[g, f] 7.3	[g, b] 15.4
6	120	1	6.89	85.58	7.53	21–R	1,800	.54	Cracked on 5th cycle	9.1	....	15.0	40.0
6	120	1	6.89	85.58	7.53	....	1,600	[g] 6.0	Survived 10 cycles from 1,500° F to still air. [g]	....	[f] 11.0	....	....
30	200	1	18.67	77.25	4.08	23–R	1,700	.79	Cracked on 5th cycle	12.6	....	14.8	36.7

[a] All specimens were matured in a gas-fired furnace at the temperature indicated for 1 hour.
[b] Ten cycles of test from 1,700° F to room temperature air blast for two test specimens, about 5½ in. by ¾ in. by ¼ in., of each composition.
[c] M/R is the modulus of rupture.
[d] Two specimens, about 5½ in. by ¾ in. by ¼ in., of each composition were tested.
[e] Three specimens, about 5½ in. by ¾ in. by ¼ in., of each composition were tested unless otherwise specified.
[f] See column on resistance to thermal shock.
[g] For preliminary report see reference [2].
[h] One specimen tested.

VI. Conclusions

No outstanding porcelain-type bodies were found in either of the systems studied, which combine all of the desirable high-temperature properties required for their use as components of heat engines, although a number of bodies are now available for various high-strength and high-temperature services where thermal-shock conditions are not of prime importance.

The limited study of the phase equilibrium relations suggests that the system MgO-BeO-ZrO_2

be considered as a simple one with the ternary eutectic at composition $4MgO:5BeO:3ZrO_2$ and 1,669° ± 3° C. No evidence of binary or ternary compound formation was observed, and an area of solid solution is suggested to extend along the $BeO\text{-}ZrO_2$ join. Ceramic bodies in this system may be matured at temperatures ranging from 1,450° to 1,600° C in approximately one-half of the ternary diagram area. The values of the physical properties of these bodies are summarized in table 9.

The summary table of these physical properties is included in order that the general properties of these porcelain bodies may be readily compared with the properties of other refractory bodies, such as are given in table 1.

TABLE 9. *Summary table of the general physical properties of some matured two- and three-oxide porcelain bodies* [a]

Physical properties	Two-oxide bodies	Three-oxide bodies	
	$MgO\text{-}ZrO_2$ [f]	$MgO\text{-}BeO\text{-}ZrO_2$	$MgO\text{-}BeO\text{-}ThO_2$
Maturing range, °C	1,700 to 1,800	1,450 to 1,600	1,500 to 1,750
Density, g/cm³	4 to 5.5	2.9 to 4.8	3.0 to 4.9
Shrinkage, percent	12.5 to 17.9	15.2 to 20.6	17.2 to 21.1
Compressive strength[b] at room temperature, $n\times10^3$ lb/in.²	166 to 229	163 to 263	166 to 266
Modulus of rupture at room temperature, $n\times10^3$ lb/in.²		13 to 39	• 9 to 14
Modulus of rupture at 1,800° F (982° C), $n\times10^3$ lb/in.²	29	13 to 32	• 13 to 16
Modulus of elasticity at 1,800° F (982° C), $n\times10^6$ lb/in.²	31 to 23	38 to 31	• 40 to 32
Thermal shock resistance.[c]		Fair to Good	Poor
Modulus of rupture at room temperature after heat shocking,[d] $n\times10^3$ lb/in.²		13 to 23	

[a] Matured bodies are those having less than 0.1 percent water absorption.
[b] Crushed at a length-to-diameter ratio of 2 between cold-rolled steel blocks, ½ in. thick, at about 31,000 lb/in.² per min.
[c] Relative values of 10 cycle test, 1,700° F ⇄ room temperature air blast. Failure before five cycles is considered as being poor.
[d] Tests made only on those specimens surviving 10 cycles of thermal shocking without cracking or spalling.
[e] Some test bars were not completely matured.
[f] Data based on a very limited number of tests.

Some limited data were determined for a few porcelains in the binary system $MgO\text{-}ZrO_2$, and these are included in the summary table.

The phase relations and the location of the primary phase boundaries in the system $MgO\text{-}BeO\text{-}ThO_2$ are similar to those in the previous system, although this is a distinctly high-temperature one with the ternary eutectic at about mole composition $5MgO:10BeO:1ThO_2$ and 1,797° ± 5° C. No evidence of compound formation was observed; and an area of solid solution is suggested, bounded by an S-shaped curve extending from about 25 percent of MgO on the MgO-BeO join along the line of 20 percent of MgO to about 70 percent of ThO_2 on the $BeO\text{-}ThO_2$ join. Ceramic bodies in this system may be matured at temperatures ranging from 1,500° to 1,750° C in approximately one-half of the beryllia field of the system bounded by the same line describing the suggested area of solid solution. The range of values determined for the various physical properties of these matured bodies is summarized in table 9.

It is of interest to note that the maturing ranges of the porcelains of each of the systems are such that all of those studied in the system $MgO\text{-}BeO\text{-}ZrO_2$, some of those studied in the system $MgO\text{-}BeO\text{-}ThO_2$, and none of those studied in the system $MgO\text{-}ZrO_2$ can be matured in the commercial kilns currently being used in the porcelain industry.

The authors are grateful to H. M. McMurdie and E. Golovato of the Bureau's Microstructure Section for the preparation and interpretation of the X-ray powder patterns and to P. J. Yavorsky, formerly of the Bureau staff, for a portion of the preliminary investigation of the system $MgO\text{-}BeO\text{-}ZrO_2$.

VII. References

[1] Gas Turbines and Jet Propulsion, NBS Letter Circular LC872 (Aug. 6, 1947), and semiannual supplements.
[2] R. F. Geller and M. D. Burdick, NACA ARR6D24 (1946).
[3] J. R. Bressman, J. Am. Ceram. Soc. **30,** 145 (1947).
[4] H. C. Cross and W. F. Simmons, OSRD No. 4717, Ser. No. M-477, NDRC, OSDR, War Metallurgy Committee.
[5] R. F. Geller, P. J. Yavorsky, B. L. Steirman, and A. S. Creamer, J. Research NBS **36,** 277 (1946) RP1703.
[6] F. P. Hall and H. Insley, J. Am. Ceram. Soc. **30,** (11) Part II (1947).
[7] R. F. Geller, J. Research NBS **27,** 555 (1941) RP1443. See also U. S. Patent No. 2,356,237.

[8] National Bureau of Standards Miscellaneous Publication M183 (April 10, 1947).
[9] R. F. Geller and P. J. Yavorsky, J. Research NBS **35,** 87 (1943) RP1662.
[10] Apparatus described by A. C. Harrison, J. Am. Ceram. Soc. **8,** 774 (1925).
[11] H. von Wartenburg and E. Prophet, Z. anorg. Chem. **208,** 369 (1932).
[12] O. Ruff, F. Ebert, and Krawczynski, Z. anorg. allgem. Chem. **213,** 333 (1933).
[13] H. von Wartenburg, H. J. Reusch, and E. Zaran, Z. anorg. allgem. Chem. **230,** 257 (1937).
[14] O. Ruff, F. Ebert, and E. Stephan, Z. anorg. allgem. Chem. **185,** 221 (1929).
[15] H. von Wartenburg and H. Werth, Z. anorg. Chem. **190,** 178 (1930); **213,** 321 (1933).
[16] H. von Wartenburg and W. Gurr, Z. anorg. allgem. Chem. **196,** 374 (1931).
[17] O. Ruff and F. Ebert, Z. anorg. allgem. Chem. **180,** 19 (1929); **87,** 198 (1914); **88,** 398 (1914); and **133,** 193 (1924).
[18] F. Ebert and E. Cohn, Z. anorg. allgem. Chem. **213,** 321 (1933).
[19] N. A. Zhirnova, J. Applied Chem. (USSR) **12,** 1279 (1939).
[20] R. Rieke and A. Ungewiss, Ber. Deut. keram. Ges. **17,** 237 (1936).
[21] E. Ryschewitsch, U. S. Patent No. 1,969,099 (August 7, 1934); see also German Patent No. 525,620 (Apr. 8, 1930).
[22] C. E. Curtis, J. Am. Ceram. Soc. **30,** 180 (1947).

Washington, April 22, 1949.

U. S. Department of Commerce
National Bureau of Standards

Research Paper RP2035
Volume 43, November 1949

Part of the Journal of Research of the National Bureau of Standards

Laboratory Flow Tests of Fixed Spray Nozzles with Hydrocarbons and with Air

By M. R. Shafer and H. L. Bovey

The metering characteristics of fixed spray nozzles of the type used in some turbo-jet engines have been investigated. Some of the nozzles supplied by the Navy Department contained burrs, metal particles, and improper machining, which caused erratic fluid metering. After being reconditioned, a group of 26 nozzles was flow-tested with five different fluids to determine the effects of fluid density, viscosity, and supply pressure upon the rate of discharge of the nozzles. The results indicate that it is impracticable to correct for differences in the physical properties of the test fluid. A comparative method of flow-testing fixed nozzles with air is described. Although this method leaves much to be desired, it appears useful for safe and rapid sizing of nozzles to within ±3 percent of their actual flow.

I. Introduction

For several years the Bureau of Aeronautics, Department of the Navy, has sponsored at the National Bureau of Standards a program of testing and research on devices for handling and metering fuels for aircraft. A recent phase of this program is concerned with the flow characteristics of fixed spray nozzles of the type that have been used in some turbo-jet engines. Depending upon the supplier, these may be designated as Monarch nozzles, Hago nozzles, etc., and for the present purpose all are essentially alike.

For the present work, three sets of sixty nozzles each were procured. Each set bore a color designation indicating that all of the nozzles of each set had been matched in flow to within ±2.5 percent at a pressure of 100 lb/in.^{2}

As a first step, all nozzles were flow-tested as received with Varsol at five different pressures. It was found that a large proportion exhibited significant changes in flow characteristics before and after being tested at a pressure of 250 lb/in.^{2} Subsequent disassembly showed that these changes were caused by burrs, metal particles, and poor machining.

From the lot of 180 nozzles, 26 were selected, cleaned, reconditioned, and assembled for use in the remainder of the tests. The flow characteristics of the 26 have remained constant over several months. In order to study the effects of the density and viscosity of the test fluid, they have been tested repeatedly over the pressure range of 5 to 250 lb/in.^{2} with the following liquid hydrocarbons: Varsol, pure *n*-heptane, Apco–467 oil, a commercial mixture of isooctanes, and Soltrol–100.

In addition, an attempt has been made to develop a method using air, instead of a flammable hydrocarbon, as the test fluid. This report presents the results that have been obtained to date with the six different test media.

II. Description of Nozzles

As shown in figure 1, the nozzles consist essentially of a body, an insert, and a strainer. They are designated by Navy Parts List No. 14G320–4.

After passing through the strainer, the fuel is directed by tangential slits in the insert into the swirl chamber formed between the end of the insert and the body. The kinetic energy of the fuel in the swirl chamber is effective in atomizing it as it escapes through the orifice in the body. The dimensions and relative locations of the tangential slits, the swirl chamber, and the orifice determine the pressure-flow characteristics, the spray angle and distribution, and the drizzle point of the nozzle. The latter may be defined as the lowest fuel pressure at which the nozzle produces

a spray, and below which it discharges large drops or a stream of fuel.

III. Flow Tests with Varsol of 180 Nozzles as Received

Figure 2 is a diagram of the apparatus used for flow-testing the three sets of 60 nozzles each, as they were received. The Varsol was circulated by a pump through a low-pressure circuit from a storage tank, through a heat exchanger, and back to the tank at a constant rate of about 200 gal/hr. Fuel to the nozzle was bled from this line, and passed through a Rotameter to a second pump having appropriate valves in a by-pass and in the discharge line. From this pump the Varsol passed through a 10-micron filter to the fitting bearing the nozzle. Fuel pressure was measured at this fitting.

The Rotameter was calibrated with the fluid used for the tests and at the temperature of the tests. Observed values of flow are believed accurate to within at least ± 0.25 percent. The pressure gages were also calibrated at intervals and are believed to be accurate to within ± 0.5 lb/in.^{2} over the range from 98 to 250 lb/in.^{2}.

The 180 nozzles were tested as received with Varsol having a kinematic viscosity of 1.102 centistokes and a specific gravity of 0.779 at the test temperature of 80° F. The flow of each was measured at the following pressures and in the order stated: 98, 150, 250, 50, 98, and 5 lb/in.^{2} gage. The results, except for the initial values at 98 lb/in.^{2}, are shown in figures 3, 4, and 5 for the sets of 60 nozzles color-coded red, green, and purple, respectively. The flows shown at 98 lb/in.^{2} were observed after the nozzle had been subjected once to the higher pressures.

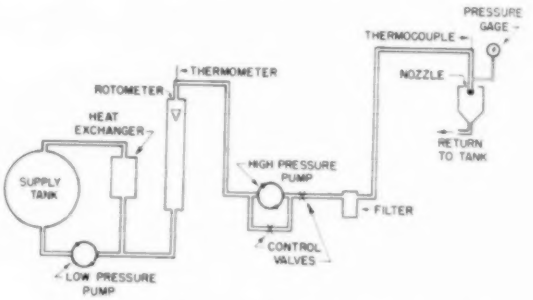

FIGURE 2. *Schematic diagram of nozzle fuel test.*

FIGURE 1. *Spray nozzle, parts list No. 14G320-4.*

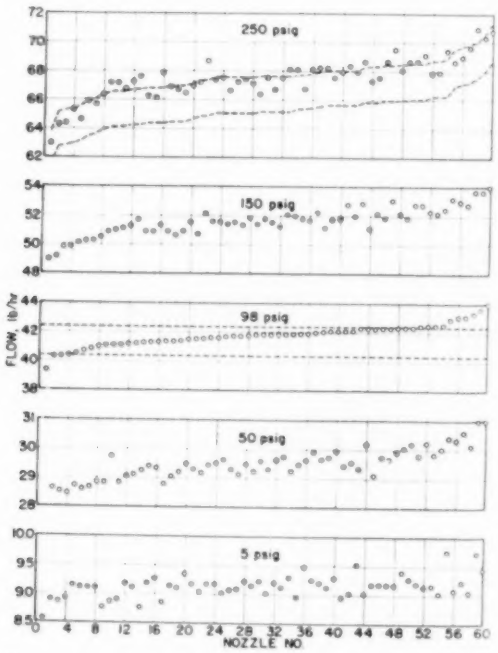

FIGURE 3. *Flow test of 60 red nozzles with Varsol.*

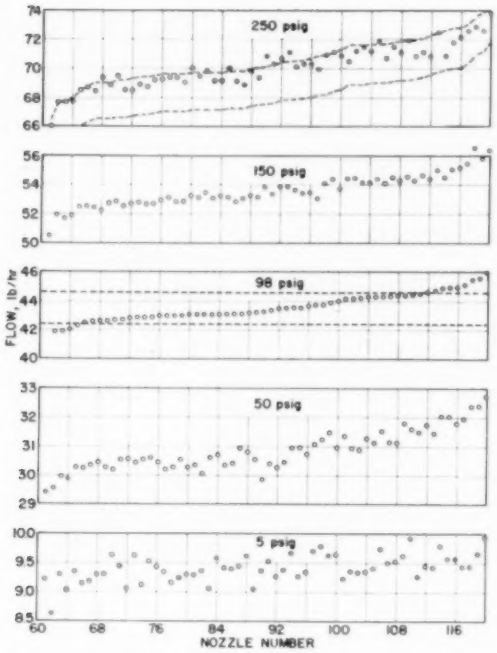

FIGURE 4. *Flow test of 60 green nozzles with Varsol.*

Specifications for these nozzles state that the flow at 250 lb/in.^{2} shall be in the range from 154 to 160 percent of the flow at 100 lb/in^2. Correcting these limits to the pressure of 98 lb/in.^{2} used in the present tests, the limits become 156 and 162 percent of the flow at the test pressure. Specified flow limits for these nozzles at 98 and 250 lb/in.^{2} are indicated by dashed lines.

It will be noted that some of the nozzles failed to flow within the specified limits, particularly the red group (fig. 3) at 250 lb/in.^{2} It is also apparent that nozzles that are matched in flow at one pressure frequently are unmatched at other pressures.

Many of the nozzles flowed differently at 98 lb/in.^{2} before and after being subjected to higher pressures. As will be seen in figure 6, this change continued for many pressure cycles with certain nozzles. The zero lines represent the flows at 98 lb/in.^{2} shown in the previous three figures. Flows at this pressure changed by more than 1 percent for 46 of the nozzles as a result of subjecting them to pressure cycling. This indicated that something must have been moved about within the nozzles during the tests.

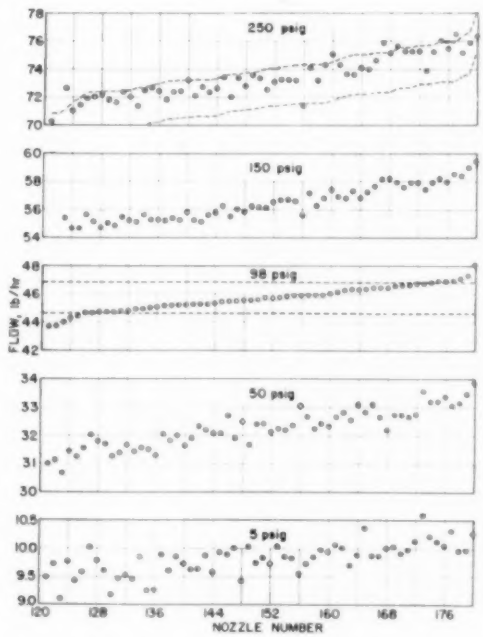

FIGURE 5. *Flow test of 60 purple nozzles with Varsol.*

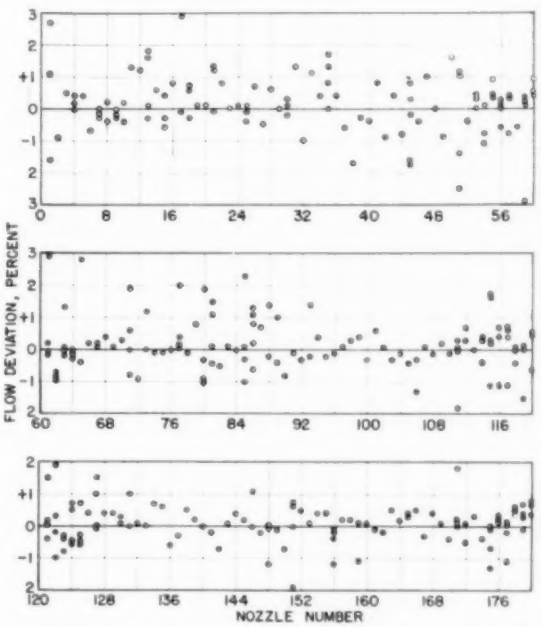

FIGURE 6. *Nozzle flow reproducibility with Varsol at 98 psig as received.*

IV. Reconditioning of 26 Nozzles

Following the above tests 26 of the nozzles were taken apart, and the following defects were found in all to varying extents:

1. There were metal chips resembling filings in the tangential slits and swirl chambers; 2. Many of the seals between inserts and bodies seemed imperfect; 3. Most of the inserts were not properly finished on the sealing end, and the edges of the slits were ragged; 4. Large burrs left in cutting the slits remained attached and caused partial blocking of the swirl chambers.

In the enlarged photograph shown in figure 7 such burrs are visible, as are the rough surface of the insert and the ragged edges of the slits.

The burrs and chips were removed, and each nozzle was reassembled with its original insert and strainer. No significant change in flow has occurred subsequently, so that it seems safe to state that initial changes were due to movements of burrs and chips by the test fluid. It is obvious that the presence of such foreign particles cannot be tolerated in a metering device.

V. Flow Tests of 26 Reconditioned Nozzles with Hydrocarbons

The 26 reconditioned nozzles, renumbered in the order of increasing flow capacity with Varsol at 98 lb/in.^{2}, were next flow-tested at pressures of 98 and 250 lb/in.^{2} with five different hydrocarbons having the following properties:

Test fluid No.	Name	Test temperature	Properties at test temperature		Equivalent sp. gr. at 60°/60° F*
			Sp. g.	Kinematic viscosity	
		°F		*Centistokes*	
1	Varsol	80	0.779	1.102	0.787
2	ASTM *n*-Heptane	80	.679	.566	.689
3	Apco-467	80	.802	2.282	.810
4	Commercial isooctanes	70	.743	.747	.747
5	Soltrol-100	75	.743	1.435	.750

* Values in this column obtained by the aid of table 3 in NBS Circular C410.

Test fluid No. 1, designated as Varsol, is a general utility solvent, stocked as a storeroom item at this Bureau. It is similar to cleaner's naphtha, made by many companies.

FIGURE 7. *Defective nozzle insert.*

Test fluids No. 2, 4, and 5 were supplied through the courtesy of the Phillips Petroleum Co., and test fluid No. 3 through the courtesy of the Anderson-Prichard Oil Corp.

Fluids No. 1, 2, and 3 were selected because each is thought to be under consideration as a standard fluid for testing jet engine auxiliaries. Fluids No. 4 and 5 were selected because they have the same density but widely different viscosities. Of the five, *n*-heptane and the mixture of isooctanes have properties approximating those of aviation gasoline, whereas Varsol and Apco resemble kerosene more closely.

The results obtained with 26 nozzles at pressures of 98 and 250 lb/in.^{2} for each of the five liquid hydrocarbons are presented in table 1.

Figure 8 is presented to show the reproducibility of the flow measurements and of the nozzles subsequent to reconditioning. Each point represents the deviation of one observation made with Varsol from the average of all observations made with the same nozzle, fluid, and test pressure. The maximum deviation does not exceed ± 0.5 percent, and only 5 of 100 observations deviate from the mean by more than ± 0.25 percent. Thus the nozzles themselves, as well as the measurements, appear satisfactory for present purposes.

The changes effected by reconditioning the nozzles are shown in figure 9. As will be seen,

TABLE 1. *Flow capacity (pounds per hour) of 26 nozzles for 5 liquid hydrocarbons*

Nozzle number	Test fluid number									
	[a] 1	2	3	4	5	[b] 1	2	3	4	5
1	38.97	39.67	38.47	39.90	37.97	62.45	58.10	62.10	59.00	60.65
2	40.00	38.45	39.50	39.40	39.00	65.50	61.20	63.80	63.25	63.35
3	40.14	37.65	39.97	38.57	39.32	64.12	60.05	65.30	61.50	62.00
4	40.26	38.20	39.92	38.80	38.95	65.45	61.50	64.25	62.70	62.70
5	41.30	38.62	40.93	40.02	40.06	66.85	61.25	66.60	63.50	64.20
6	41.52	39.00	41.80	40.41	40.45	66.85	62.65	67.25	64.65	64.58
7	41.57	39.80	40.27	40.67	40.35	67.45	63.75	66.50	66.00	64.70
8	41.57	38.37	41.46	39.57	40.12	66.05	61.70	67.25	63.45	63.45
9	41.63	38.82	40.45	41.13	39.95	66.85	61.05	66.50	64.95	64.35
10	42.07	39.05	41.10	40.55	40.70	67.30	62.10	67.60	64.60	65.10
11	42.34	41.39	41.47	41.93	41.25	69.45	66.00	67.00	67.35	66.70
12	42.40	39.52	41.47	41.16	40.75	67.55	62.85	67.95	65.15	64.85
13	42.44	40.03	42.17	41.73	40.95	69.05	63.85	68.15	66.15	66.20
14	42.60	40.33	41.98	41.42	40.74	69.20	67.30	67.90	65.85	65.85
15	42.64	40.42	42.34	41.92	41.87	69.28	63.70	68.75	66.15	66.65
16	42.67	39.92	42.64	41.30	41.22	68.55	63.60	68.85	65.90	65.85
17	43.16	41.00	43.82	42.12	41.73	70.10	65.80	70.10	67.55	67.30
18	43.67	40.77	42.92	42.13	41.86	69.65	65.25	69.80	67.35	67.05
19	44.02	40.87	42.53	42.54	42.45	70.50	64.55	70.30	67.00	67.90
20	44.73	41.37	43.87	42.83	42.77	71.10	65.70	71.60	68.05	68.45
21	45.07	41.05	43.20	43.64	43.87	72.08	66.30	72.00	68.90	69.80
22	45.20	42.08	43.72	43.59	43.03	71.85	66.10	70.60	68.55	69.40
23	45.53	42.57	45.13	43.90	44.20	72.73	68.05	73.65	70.45	70.05
24	45.66	41.83	43.97	44.45	43.97	72.05	66.85	72.95	70.50	71.20
25	46.10	42.43	44.13	44.48	44.64	72.60	65.80	73.45	68.50	70.90
26	47.60	45.07	45.83	46.42	45.79	76.88	71.30	76.00	73.45	74.10

[a] Test pressure in first five columns is 98 lb/in².
[b] Test pressure in last five columns is 250 lb/in².

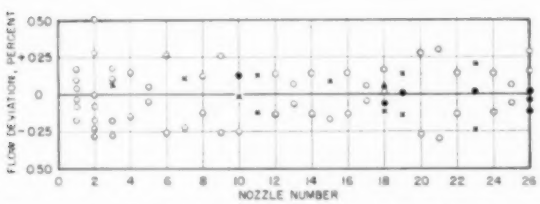

FIGURE 8. *Nozzle flow reproducibility with Varsol at 98 psig after cleaning. Number of identical readings: ○, one; x, two; ●, three; ▲, five.*

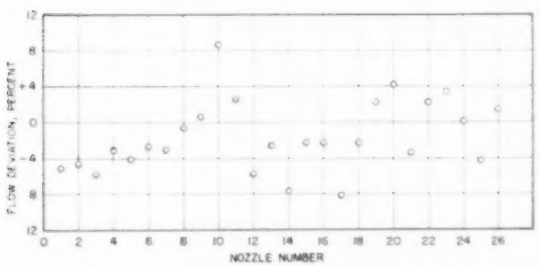

FIGURE 9. *Comparison of flows before and after cleaning nozzles. Varsol at 98 psig.*

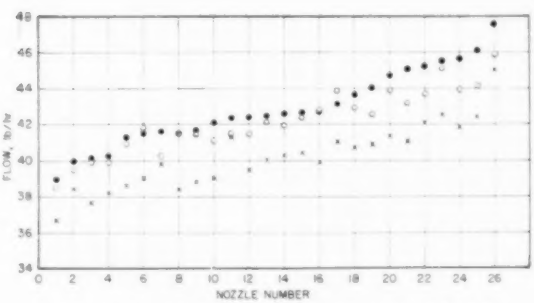

FIGURE 10. *Flow of 26 cleaned nozzles at 98 psig.* ○, Apco; ●, Varsol; x, *n*-heptane.

the changes in flow ranged from +8 to −8 percent, and only three of the 26 nozzles changed less than 1 percent.

The data of table 1 for Varsol, Apco, and *n*-heptane at a pressure of 98 lb/in.² are compared in figure 10. The nozzles were numbered arbitrarily in the order of increasing flow with Varsol, so that a relatively smooth curve is obtained for this fluid. However the corresponding curves for the other

two fluids are not smooth, indicating that nozzles matched for one fluid are not necessarily matched for fluids having different properties, and showing the need for caution in selecting a standard test fluid.

To further emphasize this point, consider the example furnished by nozzles 6, 7, 8, and 9. With Varsol these nozzles show an average flow of 41.57 lb/hr and a total spread of 0.25 percent. With *n*-heptane the order is different, the average flow 6.2 percent lower, and the spread is 3.7 percent. With Apco the flows are in a still different order, the average flow is 1.4 percent lower, and the spread is 3.7 percent. There are many other similar examples in the data of figure 10.

From the data of table 1, the ratio of the flow at 250 lb/in.^{2} to that at 98 lb/in.^{2} can be calculated for each nozzle and for each test fluid. For fluids No. 1, 2, and 3 this observed ratio is as follows:

Varsol, ranging from 157 to 164 percent, averaging 160.2 percent; *n*-heptane, ranging from 156 to 161 percent, averaging 158.7 percent; and Apco, ranging from 160 to 167 percent, averaging 163.2 percent.

As a further illustration, the ratios are plotted in figure 11 in the form of a frequency curve with

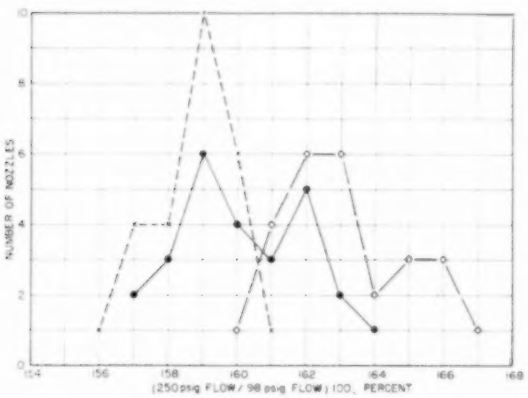

FIGURE 11. $\frac{250\ psig}{98\ psig}$ *flow ratio with different hydrocarbons*

○, Apco; ●, Varsol; ×, *n*-heptane.

each point showing the number of nozzles having a given ratio. It will be apparent from these results that the characteristics of the test fluid must be known before the ratio can be specified.

As stated previously, fluids No. 4 and 5 have the same density and were chosen to show the effects of viscosity on nozzle performance. Figure 12 shows how the results obtained with Soltrol varied from those obtained with the mixture of isooctanes. It is at once apparent that the effect of viscosity varies in both magnitude and direction from nozzle to nozzle. Hence it does not seem possible to develop any means of correcting for the viscosity of the test fluid.

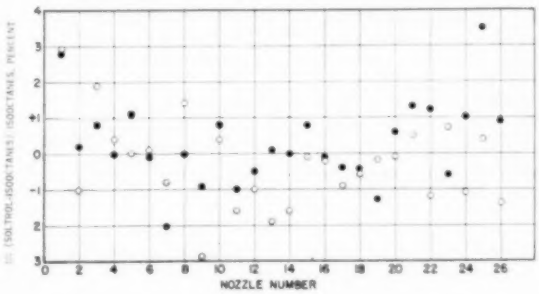

FIGURE 12. *Viscosity effect on spray nozzles.*

○, 98 psig; ●, 250 psig.

VI. Flow Tests With Air

Early in this nozzle test program it appeared desirable to attempt the development of equipment using air instead of a flammable hydrocarbon as a test fluid. Such development seemed a logical extension of the previous successful evolution of the Navy Orifice Comparator, in which air is used to flow-test metering jets of aircraft carburetors with greater speed, accuracy, and safety than could be attained by other methods.

In applying the method to spray nozzles, the apparatus shown diagrammatically in figure 13 was investigated. Briefly, air compressed to 50 lb/in.^{2} or more is passed through a pressure regulator and a filter to a test fixture consisting essentially of two chambers, each about 1¼ in. in diameter by 4 in. in length, separated by a small orifice or bleed. The second chamber serves as a mounting for the nozzle, through which all of the regulated air escapes to the atmosphere. Pressure taps and manometers provide for observing the pressure in the second chamber and the drop in pressure between the two chambers.

In operation, the pressure in the second chamber is held constant, which means that the drop in pressure across the nozzle is also constant, and the drop in pressure across the bleed between the two chambers is observed. The latter is determined by

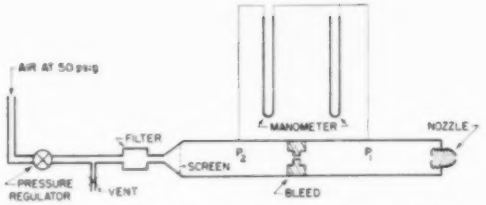

FIGURE 13. *Schematic diagram of nozzle air test.*

the volume rate of flow between chambers, which, in turn, is a function of the flow characteristics of the test nozzle.

Obviously the method is comparative rather than absolute, so that a set of nozzles calibrated by some other method is required for the calibration of the equipment using air. For nozzles having a flow capacity in the range 40 to 50 lb/hr at 100 lb/in.^{2}, it has been found by experiment that the air-test method gives best results when the bleed between the two chambers consists of a single hole made by a No. 76 drill (diameter=0.019 in.), and when the pressure in the second chamber is from 1.2 to 2 times the pressure drop across the bleed.

In developing the air-test method, the 26 nozzles mentioned previously were tested with various constant pressures in the second chamber throughout the range from 10 in. of water to 50 in. of mercury. The best correlation between results with air and with liquid hydrocarbons is obtained in the range 25 to 35 in. of mercury. An example of this correlation is given in figure 14, in which the pressure in the second chamber (P_1) was 30 in. of mercury, and the observed drop in pressure across the bleed (P_2-P_1) is plotted against the observed flow of Varsol at a pressure of 98 lb/in^2. The best smooth curve through the observed points seems to be a straight line, from which the maximum deviation is less than 2 percent and the average deviation is less than 1 percent. The sensitivity of this air apparatus was about 1 in. of mercury per pound of fuel discharged through the nozzle per hour.

The dashed lines in figure 14 are the limits of flow specified for nozzles coded red, green, and purple. On the basis of the results shown in this figure it might be concluded that the air-test method was satisfactory for flow-testing spray nozzles. If this were true, it is certainly to be preferred from the standpoint of speed and safety.

As already stated, figure 14 compares the results obtained with air and those obtained with Varsol. Similarly figure 15 shows a comparison of results with air and Apco, and figure 16 shows a comparison of those with air and *n*-heptane, all data for liquid fuels being for a pressure of 98 lb/in^2. Deviations from the straight lines are all within ± 3 percent except for one nozzle in figure 16. Considering that the nozzles do not perform consistently with the three liquid test fluids, as was shown in figure 10, the correlation of the results with air and those with liquids is better than might have been expected.

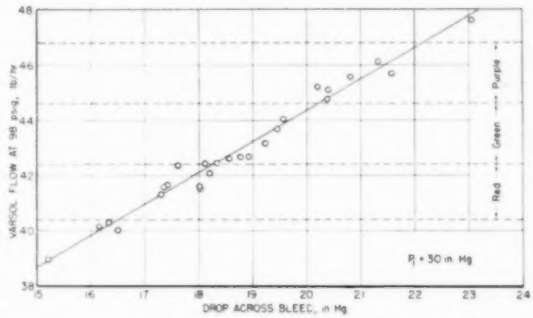

FIGURE 14. *Correlation of nozzle tests with air and Varsol.*

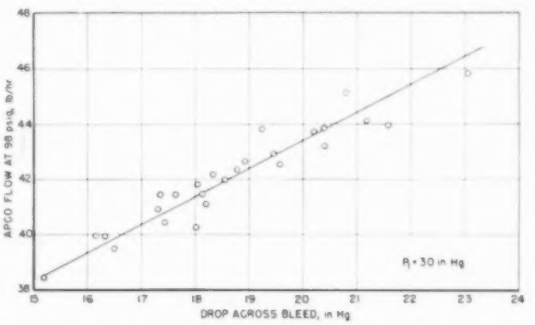

FIGURE 15. *Correlation of nozzle tests with air and Apco.*

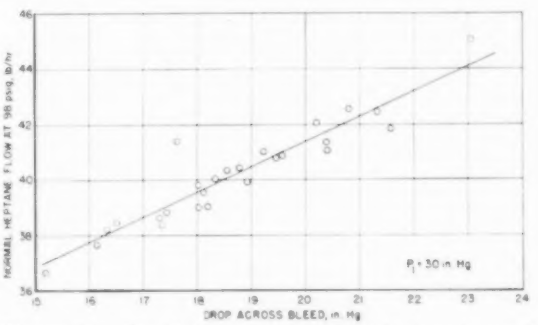

FIGURE 16. *Correlation of nozzle tests with air and normal heptane.*

In its present state, the air-test method would seem to have considerable merit for preliminary tests of nozzles, particularly in production and after overhaul. It would certainly be valuable in rejecting nozzles that flow so far from the design value that tests with liquid would be a waste of time, and in grouping nozzles within reasonably narrow flow limits. It might also be useful in the matching of nozzle bodies and inserts to get desired performance.

As a matter of fact, the uncertainties in the performance of nozzles determined with air are probably little, if any, greater than the present uncertainties in the actual performance of nozzles in engines. Consequently the further development of the air-test method will be carried along as rapidly as the resolution of the over-all problem of nozzle performance seems to warrant.

VII. Discussion and Conclusions

The nozzles used in these tests were received late in 1947, and are believed typical of nozzles of this type in production at that time. The presence of chips, burrs, and inadequate finish on certain parts were pointed out months ago, and it seems probable that such easily remedied faults may no longer be a matter of concern.

A fixed nozzle performs two important functions, namely the production of a spray and the metering of fuel. This report deals only with fuel metering. In nozzles of the type tested, this is accomplished primarily at two locations within the nozzle. These are at the four tangential slits that operate in parallel, and at the discharge orifice in the nozzle body, which is in series with the four slits. It is not surprising, therefore, that the simple law of discharge through an orifice does not hold exactly for the nozzle as a whole. As examples, the relation between pressure and flow for one nozzle may differ somewhat from that of another, and the effect of a given change in viscosity of the test fluid may be in one direction for one nozzle and in the opposite direction for another.

Examined from this point of view, it is surprising that the results obtained with six different test fluids including air agree as well as they do.

Perhaps the most obvious conclusion from these studies involves the choice of a fluid suitable for testing fuel nozzles and other engine auxiliaries. It is believed that a fluid chosen as a standard for this purpose should have as many of the following characteristics as may be found attainable:

(a) It should be cheap and free from highly strategic ingredients; (b) It should be available in quantity from many sources, and its physical properties should be readily reproducible from a production standpoint; (c) It should be safe, noncorrosive, and should have the same effects as engine fuels on packings, diaphragms, etc.; (d) Its physical properties should be the same as those of engine fuels and should not change with use by evaporation of light ends; (e) When exceptions are made to the above requirements, it must be possible to interpret data obtained with the test fluid in terms of performance in engines.

If the test fluid differs in density and/or viscosity from the fuel used in the engine, the present results show that:

(a) The actual rate of fuel delivery to the engine at any pressure may differ by several percent from the rate predicted from the test data; (b) Nozzles matched for the test fluid at a particular pressure may not be matched at this or any other pressure in the engine; and (c) it will not be practicable to develop corrections which are generally applicable for differences between physical properties of the test fluid and the engine fuel.

Both density and viscosity of the fuel being metered by a nozzle are important in determining its rate of discharge at a given pressure. Both those properties change considerably with temperature. Thus it seems likely that turbo-jet operation might be improved by giving more attention to the temperature of the fuel entering the individual nozzles, and to possible methods for its control.

Much additional thought and experimentation are warranted in the development of nozzle test data that will be truly indicative of the performance of nozzles in operating engines. Even though some fluid is selected as a standard for test purposes, there remains the development of satisfactory test methods and the evolution of significant test specifications. An obvious first step toward the latter is the determination of tolerances in flow that can be allowed in engines, and more particularly of the unavoidable differences encountered in operating engines.

Thus the over-all problem of determining, by means of bench tests, whether a given set of spray

nozzles will give optimum performance in an engine is highly complex. Equally difficult is the testing of a set of replacement nozzles so there will be no question that they will perform as well as the original set.

So long as spray nozzles are used in engines, there is no doubt that solution of the aforementioned problems will pay dividends in improved engine performance, particularly at high altitudes. Employment of spray nozzles requires that the general level of fuel pressure be high, which in turn involves mechanical difficulties with fuel pumps, lines, manifolds, and seals, and increases the fire hazard in case a fuel line is broken. It, therefore, seems legitimate to raise a question as to the relative merits of expending research effort on the further development of the various components of high-pressure fuel systems, or on the development of combustion chambers that will function with low-pressure fuel and without spray nozzles.

WASHINGTON, January 10, 1949.

U. S. Department of Commerce
National Bureau of Standards

Research Paper RP2036
Volume 43, November 1949

Part of the Journal of Research of the National Bureau of Standards

Mechanical Production of Very Thin Oscillator Plates

By Leland T. Sogn and Walter J. Howard

To produce quartz oscillator plates thinner than 0.005 inch, it has been necessary to modify the usual lapping methods and machinery. The thickness at which the crystal carrier (nest) stretches or buckles is the limiting factor in the conventional apparatus. The modifications described in this report consist of replacements for the conventional top lapping plate with corresponding changes in the crystal carrier. The development is presented in chronological order from the simple pressure block method to the more elaborate forms using automatic truing. The improved equipment is capable of producing 0.001-inch-thick quartz crystals and can be used for producing equally thin wafers from a variety of other materials.

I. Introduction

In order to manufacture crystals that are thin enough and have the proper contour to give the high fundamental frequencies now being sought, it has been necessary to modify the usual lapping procedure and to design appropriate apparatus. Various modifications have been tested; the most desirable features have been retained and obvious weaknesses corrected (as far as possible) in evolving each subsequent model. The apparently defective units have not been abandoned; reexaminations and alterations in the light of added experience have been made whenever time and funds have permitted. The most successful machines developed in this laboratory produce crystals 0.001 in. thick. Further improvements are expected, and the ultimate thickness will depend more on problems related to the handling of such fragile crystals than on the mechanical limitations of the finishing equipment.

II. Conventional Method

Usually blanks to be lapped are placed in the apertures of a metal or plastic nest, which carries them through a curved path between the laps—two heavy flat plates charged with abrasive. A modified drill press drives the nest by means of an adjustable eccentric and a bushing (fig. 1). Since the nest must be thinner than the crystals to permit their abrasion, the thickness of the nest is the limiting factor. Because of the stretching and buckling that occur, this limit is about 0.005 in. for most available materials, and quartz crystals with such a thickness have maximum fundamental frequencies of not more than 14 and 20 mc for AT and BT cuts, respectively. These cuts are most generally used for high-frequency oscillators.

FIGURE 1. *Conventional lapping equipment.*

The thin carrier (nest) with its pentagonal openings may be seen projecting from its position between the upper and lower laps.

855498—49——3

III. Cemented Block Method

The final thickness of the crystal was made independent of the nest thickness by putting the plane of pressure application below the upper surface of the nest. In the first modification this was accomplished by cementing a ⅜-in.-high by ½-in.-square steel block to each ½-in.-square crystal. The cemented units were placed in a nest (0.025 in. thick) and driven in the usual curved path over the lower lapping plate only, the individual blocks furnishing pressure previously supplied by the top plate. Blanks of less than 0.002-in. thickness were produced in this manner, but they were too wedge-shaped to oscillate.

This method of mounting had important disadvantages. Each crystal had to be mounted parallel to the block edges, without strain, precisely in the center of the base with the normal to the geometric center of the major crystal surface passing through the geometric center of the block. Such conditions were difficult to more than approximate. Furthermore, it was necessary to detach the crystal to check thickness, contour, and frequency. For these reasons other schemes were tried.

IV. Free Block Method

In the next experiment the same apparatus was used, but the block was permitted to rest freely on the crystal (fig. 2). Slight movements of the block relative to the crystal constantly redistributed the abrasive mixture between the block and crystal, thus preventing accumulations that would cause unequal distribution of pressure by the block. However, wedge-shaped crystals again resulted and crystals tended to slip under the nest, so this procedure was suspended while other paths were pursued.

During the reinvestigation it was observed that the movements of both blocks and crystals were violent and irregular at the lowest pulley speed, so the motor speed was reduced by means of a variable autotransformer until, at 40 rpm, the motion appeared to be satisfactory. Regularly, at quarter- or half-hour intervals each block was turned 90° with respect to its crystal in order to compensate for minor variations, such as the overhand of the block. Crystals 0.011 in. in thickness were brought down to 0.0025 in. without breakage, using the relatively coarse size 400 silicon carbide.

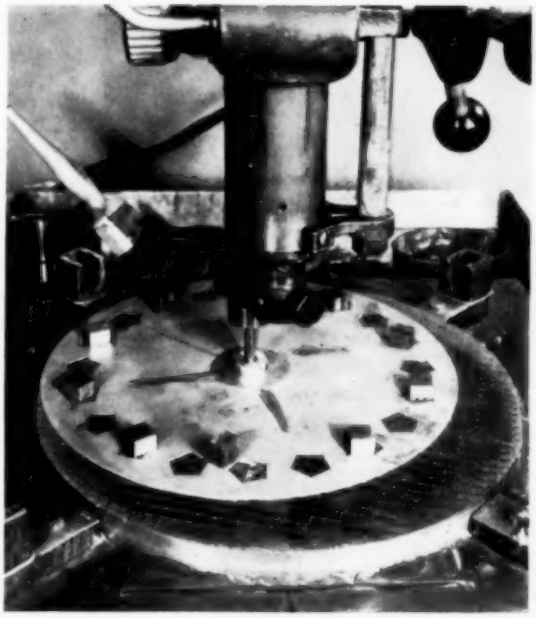

FIGURE 2. *Free block apparatus.*

Here a block of the foreground has been turned up to show both the channeling on its undersurface and the crystal that is normally beneath it. The upper surface of the lower lap is also channeled to reduce sticking.

To keep crystals from slipping beneath the thin (0.020-in.) zinc nest, small weights were placed around the loaded openings. A heavier nest would have made this unnecessary.

Crystals so processed were almost flat, being only slightly and equally high at the corners. The high corners were removed by edge-grinding to a lesser dimension.

Major advantages of the method are: The apparatus is simple; the lapping is so gentle that breakage is virtually eliminated; individual crystals may be removed from the nest easily, permitting more frequent and more satisfactory inspection; crystals of widely varying thicknesses may be simultaneously lapped. On the other hand, the rate of lapping is slow, and the crystal faces must be parallel at the start, as the block is resting on and parallel to the upper surface of the crystal rather than to the lapping plate.

V. Square Block and Cell Method

As a means of more effectively controlling the movement of the crystal and pressure block relative to each other, both were confined in the ½-in.

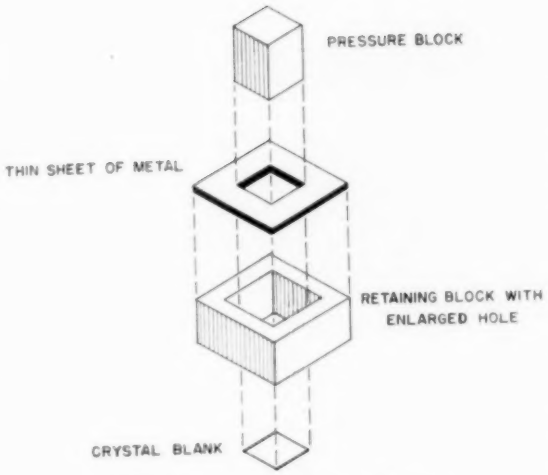

FIGURE 3. *Square block and cell—parts.*

This exploded diagram shows the relation of the various parts to each other. In operation, the pressure block rests on the crystal and passes through the thin sheet that is cemented to the retaining block.

FIGURE 4. *Square block and cell apparatus assembled.*

Here the parts shown in the previous figure have been assembled and are ready to be driven by the nest over the lap. Blocks in background are counterweights.

square opening made through the center of a 1-in. square by ¼-in.-thick steel plate. This unit was then placed in a nest that had pentagonal openings suitable for lapping inch square blanks. Counterweights were placed in the other nest openings to give more uniform motion.

Because the abrasive that worked into the narrow clearances between the block and plate caused binding, the opening in the plate was enlarged to about ⅝ in. square. A thin zinc sheet with a ½-in. square hole was cemented to its upper surface to hold the pressure block in position while permitting the crystal to move relative to it (fig. 3). Channels across the block surface facilitated this movement by reducing the area of adhesion between it and the crystal. This modified cell assembly was lapped in the same nest and manner used above as shown in figure 4. Crystals produced by this method were wedge-shaped. However, the process seemed to hold so much promise that a modification that eliminated binding and permitted automatic truing was designed. This unit, which employs a cylinder and plunger, has been put into operation recently. Its performance is described later in the article.

VI. Pentagonal Block and Ring Method

In a somewhat more elaborate apparatus (fig. 5), pentagonal blocks were rigidly attached to a lapped ring. The blocks fitted snugly in the openings of the nest, which was driven by the eccentric as before. Because this arrangement permitted truing of the pentagonal blocks until the lower surfaces were coplanar and parallel to the lap, wedge-shaped crystals could be corrected to parallelism, an important feature. Adhesion between blanks and blocks was reduced by channeling the under surface of the blocks. Springs between the ring and nest forced the nest into closer contact with the lap, thereby eliminating the breakage due to crystals slipping beneath the nest. Weights could be used in place of springs but have not yet been tried.

In this method, as in all the modified procedures, the greater part of the abrasion took place on the under surface of the crystals, the top surface being more polished than abraded. To insure equal wear and similar contours on both surfaces, the crystals were inverted at regular intervals. Since the contours of the crystals were dependent on the trueness of the pentagonal blocks, the blocks (still attached to the ring) were lapped before and at suitable intervals during each run.

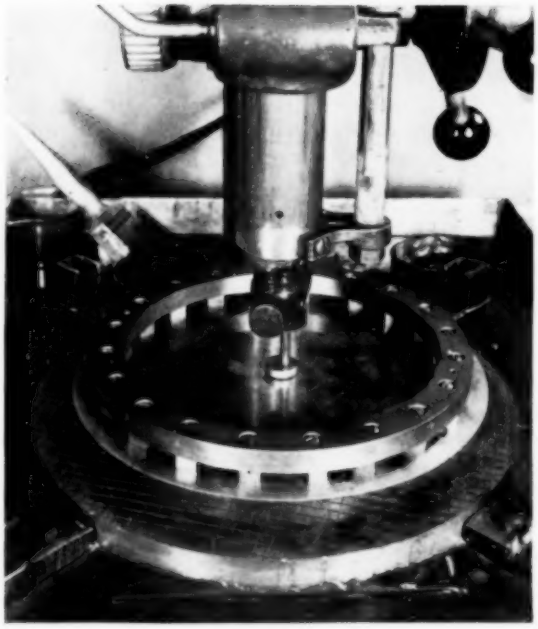

FIGURE 5. *Pentagonal block apparatus.*

Twenty pentagonal blocks, rigidly attached to a steel ring are shown resting on crystals (hidden) in the corresponding nest openings. Some of the springs that force the nest into close contact with the lap may be seen.

Results achieved by the use of the pentagonal block system were encouraging. Deviations from flatness were radial rather than wedge-like. The variation did not exceed 0.00004 in. and was, for the most part, concentrated in a rim-like bulge, the enclosed area being very nearly flat and parallel. BT crystals with a thickness of about 0.0025 in. and a fundamental frequency of 43 mc were produced. Such crystals could be etched to even higher frequencies.

Experience with the pentagonal block system suggested two modified procedures. In one, the nest was eliminated; in the other, a thick nest with circular holes was used.

VII. Driven Ring Method

The nest-less apparatus consisted of a flat ring upon which were mounted cylindrical blocks, each with an encircling ring or collar to retain the crystal (fig. 6). The collars and the under surfaces of the blocks were channeled to improve circulation of the abrasive mixture. An eccentric, acting through four rigid spokes, drove this assembly over the lower lap. Because the ring

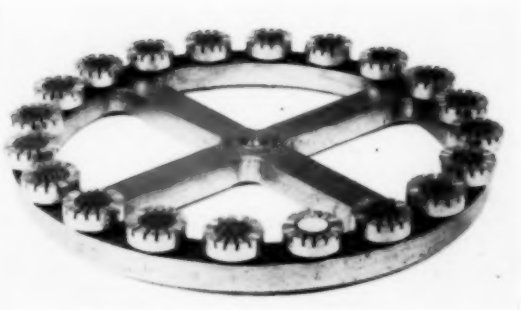

FIGURE 6. *Driven ring apparatus.*

The apparatus has been inverted to show more clearly the relationship of the parts. A round crystal is shown resting on one of the lapping plugs and in contact with its confining collar. The collars have been slotted to permit freer circulation of abrasive.

and spokes were of thick steel, the load on the crystals was quite heavy. As a result, crystals began to break when approximately 0.004 in. thick. The investigation has been discontinued until a ring of lighter metal can be made.

VIII. Ring and Thick Nest Method

This modification made use of the same type of ring as above but without the spokes, since the ring was carried by the nest (fig. 7.) Cylindrical plugs were used without collars. Instead, holes were carefully drilled and reamed in a thick and rigid nest. Each hole was a sliding fit on any plug of the ring. (Indeed the main advantage of using the circular rather than the pentagonal

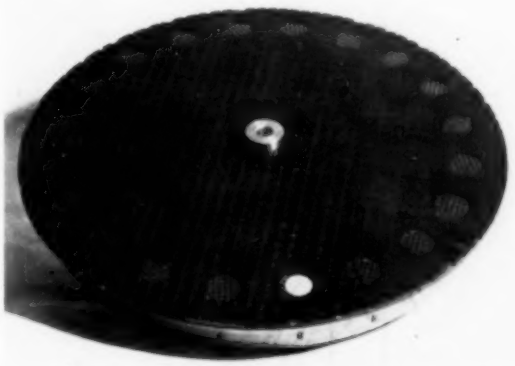

FIGURE 7. *Ring and thick nest apparatus.*

The apparatus is inverted to show the relationship of the parts. The crystal is resting on one of the round plugs and within the nest aperture that confines it during lapping. The plugs fit the apertures very closely to prevent the formation of rims on the crystals.

openings lay in the ease with which apertures and plugs could be made to close tolerances). As in the pentagonal block method, the nest served both to retain the crystals and to adjust the pressure on them. This latter effect was accomplished by the use of small conical springs, the apex ends of which fitted tightly over studs located midway between the lapping blocks and the base ends of which pressed the nest into closer contact with the lapping plate. Changing the number of springs adjusted the pressure on the crystals, permitting heavier pressure and faster lapping on the thicker crystals and similarly, lower pressure and slower lapping on the thinner ones. Cross-channeling the under side of the nest with grooves $\frac{1}{32}$ in. wide by $\frac{1}{16}$ in. deep at $\frac{1}{4}$-in. intervals allowed freer circulation of the abrasive and reduced adhesion between the lap and the nest.

Although this method is still under investigation, some conclusions have been drawn. Since the nests were thicker than those available commercially, the apertures maintained their size and shape much better than did the openings in the thin nests. Consequently, the clearance between each plug and its respective hole remained small and the resulting rim was much less pronounced. In the case of square crystals, the rimming was confined to the corners where its effect on performance appeared to be negligible. So far, crystals have been ground to a thickness of 0.002 in. by this method.

Although no definite limit was imposed on the final thickness of crystals produced with the equipment last described, the hazards connected with removing the ring and nest in order to inspect crystals less than 0.002 in. thick made another method seem more desirable for the final stage of lapping.

IX. "Inkwell" Method

As mentioned earlier, a cylinder and plunger modification has been designed on the basis of experience with the square block and cell unit. In the improved form (fig. 8) the retaining cell consists of a circular aperture in a heavy-walled brass block, approximating an inkwell in size and shape. The conical shape is a compromise between height and stability, and the base is broad to maintain its true surface. The bottom part of the block is a detachable annular disk, the central

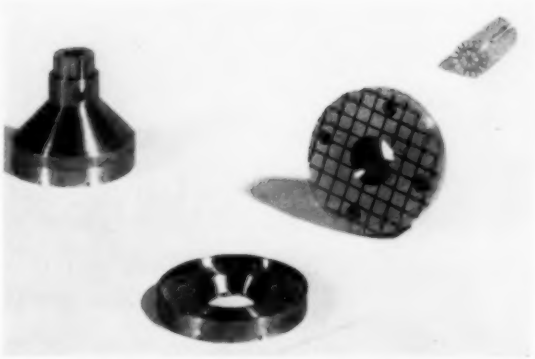

FIGURE 8. *Inkwell apparatus—parts.*

The keyed plunger, conical body, and annular disk are shown assembled at the left. In the foreground may be seen the upper surface, chamfer, and bore of the disk part. The lower surface and its relation to the bore is evident in the unit slightly to the right, while the plunger may be seen in the right background.

hole of which contains the crystal during lapping. The diameter of this hole is just enough larger than the plunger to prevent binding by the abrasive. For the same reason the cell is quite shallow. A recess on the upper block together with the chamfered upper surface of the disk prevents abrasive from reaching the more closely machined upper bore. Since the disk is detachable, it can be replaced easily when wear renders it unusable.

The cylinder bore is a smooth fit for $\frac{3}{4}$-in. drill rod. For lighter pressure, hollow aluminum plungers are being used. Close fit (especially in the upper bore) is essential to keep the plunger from wobbling. The plunger and block base are trued with respect to each other against the lap. A pin in the block wall engages a keyway in the upper part of the plunger thereby preventing its rotation while permitting vertical motion. In this manner the trued surfaces of the plunger and base remain parallel (except for the factor of prolonged wear). It is customary to true these surfaces at about 8-hour intervals. As in previous lapping units, the working surfaces are channeled to improve circulation of the abrasive and to reduce adhesion.

To operate, the loaded unit (cell block with plunger and crystal) is placed in one of the circular apertures of a heavy nest and carried over the lower lap in the usual curved path (fig. 9). Since the aperture is 0.015 in. larger than the cell block and the cell aperture is considerably larger than the enclosed crystal, all three—crystal, block, and

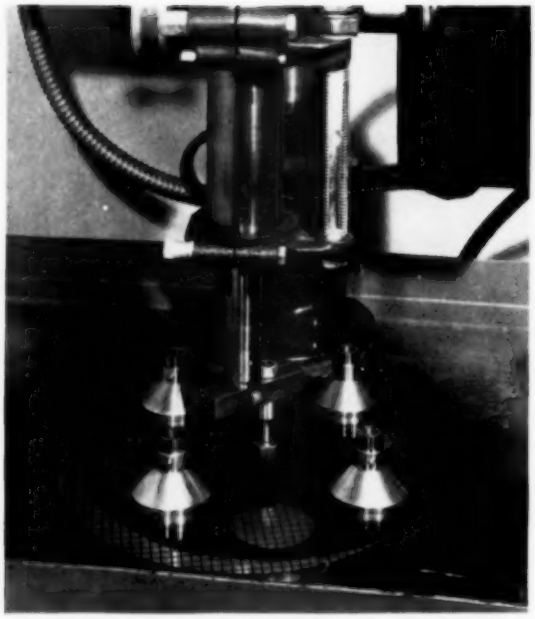

FIGURE 9. *Lapping set-up with inkwell units.*

The assembled units are shown ready to be driven over the lap in the usual manner.

nest—execute different eccentric motions. The present lap and nest can accommodate eight units. The crystal in any one of these units can be easily examined without disturbing any other crystal, a very useful feature.

Using this apparatus crystals have been lapped to about 0.001 in. with practically no breakage. The edges were smooth and free from radial cracks, and the faces were, in general, satisfactorily flat. Naturally crystals so thin are fragile and handling them in the usual routines of cleaning, measurement, plating, and mounting gives rise to important new problems. These problems, rather than the method of lapping, may set the ultimate limit for crystal thickness.

X. Tall Plunger Method

With the intention of regulating the piston wobble, a modification of the above unit has just been completed. In the new unit the plunger is taller and bears on rounded points rather than on a wall. Twelve screws with rounded ends serve as the bearing points, six being equally spaced around the piston near its top and another six

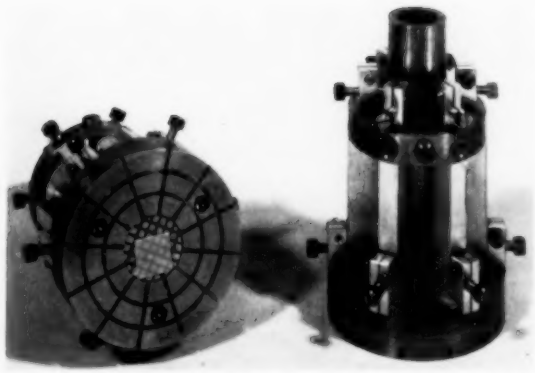

FIGURE 10. *Tall plunger apparatus.*

Bearing point screws replace the close fitting bore in this modification of the inkwell model. Slots in the uprights permit the transverse screws to lock the bearing point screws in position.

similarly spaced near the bottom (fig. 10). After these screws have been adjusted to permit sliding without lateral play, the transverse screws are tightened to maintain the fit. This modification has yet to be tested.

XI. Conclusion

Of the ten methods described the last three were the most satisfactory. Although they have been developed primarily for the production of thin quartz oscillator plates they can be used for lapping a variety of mineral and ceramic materials. For example, plates of a ceramic dielectric have been lapped by the inkwell apparatus to 0.0015-in. thickness. In such experimental work the individual plunger and block units are especially useful, since only a minimum of the test material is needed. As previously mentioned, a number of such units may be used with one driving nest to lap test specimens of various thicknesses simultaneously. However, since the driven nest with ring-mounted plugs accommodates more crystals on the same size lap it is more economical when many plates of the same thickness are to be made. Both methods have their special features, and it is likely that development will continue along two paths to provide machines that will better serve, on the one hand, for production of experimental or special orders, and on the other hand, for commercial quantities.

WASHINGTON, June 14, 1949.

U. S. Department of Commerce
National Bureau of Standards

Research Paper RP2037
Volume 43, November 1949

Part of the Journal of Research of the National Bureau of Standards

Instability in Shear of Simply Supported Square Plates With Reinforced Hole

By Wilhelmina D. Kroll

The critical shear stresses were determined for five elastic, simply supported square plates with central circular holes of diameter one-eight and one-fourth the length of a side. Comparison of the numerical results obtained with those computed for plates without holes shows that, although an unreinforced hole may cause a large reduction in the critical shear stress of the plate, reinforcement of the hole by a circular doubler plate causes a substantial increase in the shear buckling load.

I. Introduction

Holes must frequently be cut in the stressed skin surfaces of airplane wings or fuselages to provide access to the interior of the wing or fuselage. To prevent weakening of the entire structure thereby, the hole is usually reinforced by a circular doubler plate riveted to the inner surface of the sheet.

The present report is one of a series of studies undertaken for the Bureau of Aeronautics, Navy Department, in order to understand more fully the effect of reinforcements in strengthening and stabilizing the structure around a hole. In reference [1],[1] a theoretical investigation was presented of the effect of various reinforcements on the stresses and displacements near a small circular hole in a plane sheet under uniform tension in all directions. Numerical values of stress concentration and of radial displacement at the edge of the hole for various doubler plates indicated that the greatest reduction in stress concentration for a given volume of reinforcing material occurs when the outer radius of the reinforcement is smallest and that the reduction in distortion of the hole depends principally upon the volume of the reinforcement.

Tests were made on plates with reinforced circular holes, under uniform tension in one direction only, reference [1], to check the theoretical analysis, and it was found that, if the reinforcements were attached to the sheet with two concentric rows of rivets or bonded to the sheet, the theoretical analysis gave a sufficiently accurate description of the stresses and displacements in the neighborhood of the hole.

In reference [2], results of compressive tests of curved panels with circular holes unreinforced or reinforced with doubler plates are given, which show that curvature has no appreciable effect on the median fiber strain distribution around a hole and that the plane stress theory can be used to reliably predict the stress distribution in the unreinforced regions of curved panels with holes.

A theoretical analysis for the stress distribution in a flat plate near a reinforced circular hole loaded by a pin was presented in reference [3]. Results obtained in the theoretical analysis and those from a test of a plate of sandwich construction showed good agreement.

A method is presented in reference [4] for determining the instability under edge compression of a rectangular plate with a reinforced circular hole. The values of critical compressive stresses of square plates obtained by this method indicated that, although the buckling stress of a plate is reduced only a small amount by the presence of an unreinforced hole, reinforcement of the hole causes a substantial increase in the buckling stress. Reinforcement of a hole, therefore, can be expected to stabilize as well as strengthen the structure in the neighborhood of a hole when the structure is under compressive load.

[1] Figures in brackets indicate the literature references at the end of this paper.

Using the method of reference [4], a study is made in this report of the effect of the reinforcement of a circular hole in a square plate on the stability of the plate under shearing loads uniformly distributed along the edges of the plate.

II. Method of Analysis

In reference [4], an energy method was presented for computing the compressive buckling load of a simply supported elastic rectangular plate having a central circular hole reinforced by a circular doubler plate. This method can also be used to determine the critical shearing stress for simply supported rectangular plates having a central circular hole.

The integrals I_1 and I_2, which must be evaluated for the plate are:

$$\left.\begin{aligned} I_1 &= \int\int_{\text{surface}} D\left\{\left(\frac{\partial^2 w}{\partial x^2}+\frac{\partial^2 w}{\partial y^2}\right)^2 - 2(1-\mu)\left[\frac{\partial^2 w}{\partial x^2}\frac{\partial^2 w}{\partial y^2}-\left(\frac{\partial^2 w}{\partial x \partial y}\right)^2\right]\right\} dx\,dy \\ I_2 &= \int\int_{\text{surface}} h\left[\frac{\sigma_x}{\tau_\infty}\left(\frac{\partial w}{\partial x}\right)^2+\frac{\sigma_y}{\tau_\infty}\left(\frac{\partial w}{\partial y}\right)^2+2\frac{\tau_{xy}}{\tau_\infty}\frac{\partial w}{\partial x}\frac{\partial w}{\partial y}\right] dx\,dy \end{aligned}\right\} \quad (1)$$

where h = plate thickness, function of x and y;
x, y = rectangular coordinates with origin at center of plate;
w = lateral deflection of plate;
$D = Eh^3/12(1-\mu^2)$, flexural rigidity of plate, function of x and y;
μ = Poisson's ratio, 0.3;
σ_x = tensile stress in x direction;
σ_y = tensile stress in y direction;
τ_{xy} = shear stress in x and y directions;
τ_∞ = shear stress in x and y directions far from the hole.

The stress ratios σ_x/τ_∞, σ_y/τ_∞ and τ_{xy}/τ_∞ just prior to buckling may be obtained from reference [4] in the following way. If the origin of coordinates is taken as shown in figure 1, shear stresses along the edges of the plate will be equivalent to tensile stresses acting at the edge of the plate at $\theta = 45°$ and equal compressive stresses acting at the edge of the plate at $\theta = -45°$. The constants F and K of reference [4] are zero in the case of shear loading. The stresses σ_r/τ_∞, $\sigma_\theta/\tau_\infty$, and $\tau_{r\theta}/\tau_\infty$ referred to polar coordinates r, θ are then given as

$$\left.\begin{aligned} \sigma_r/\tau_\infty &= -(A+3CR^4/r^4+2DR^2/r^2)\cos 2\left(\theta+\frac{\pi}{4}\right) \\ \sigma_\theta/\tau_\infty &= (A+6Br^2/R^2+3CR^4/r^4)\cos 2\left(\theta+\frac{\pi}{4}\right) \\ \tau_{r\theta}/\tau_\infty &= (A+3Br^2/R^2-3CR^4/r^4-DR^2/r^2)\sin 2\left(\theta+\frac{\pi}{4}\right) \end{aligned}\right\} \quad (2)$$

where r, θ = polar coordinates with origin at center of hole (see fig. 1);
θ = angle between radius r to point and positive horizontal axis. Positive θ measured in counter clockwise direction;
R = radius of hole;
A, B, C, D = coefficients with different values in sheet and reinforced region.

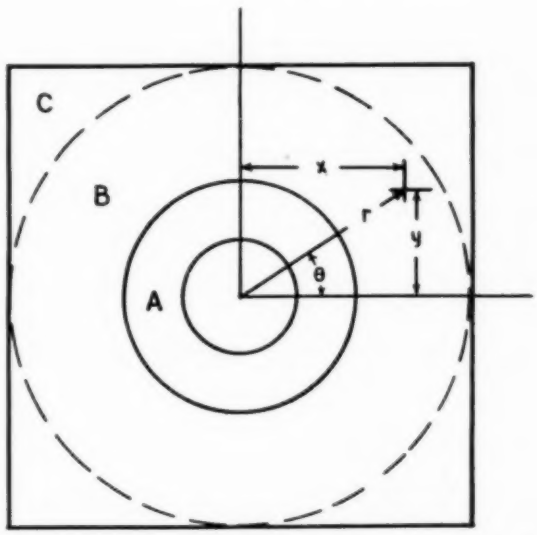

FIGURE 1. *Subdivision of plate into three portions A, B, and C, in evaluating I_2*

The values of A, B, C, and D may be determined as outlined in reference [4]. The stresses in rectangular coordinates may be computed from the

stresses in polar coordinates, eq 2, by use of the conversion formulas:

$$\left.\begin{aligned}\sigma_x &= \sigma_r \cos^2\theta + \sigma_\theta \sin^2\theta - \tau_{r\theta} \sin 2\theta \\ \sigma_y &= \sigma_r \sin^2\theta + \sigma_\theta \cos^2\theta + \tau_{r\theta} \sin 2\theta \\ \tau_{xy} &= \frac{\sigma_r - \sigma_\theta}{2} \sin 2\theta + \tau_{r\theta} \cos 2\theta\end{aligned}\right\} \quad (3)$$

The lateral deflection, w, of a simply supported rectangular plate of length a and width b can be approximated by the first terms in the trigonometric series

$$w = a_{11} \cos\frac{\pi x}{a} \cos\frac{\pi y}{b} + a_{22} \sin\frac{2\pi x}{a} \sin\frac{2\pi y}{b} + a_{13} \cos\frac{\pi x}{a} \cos\frac{3\pi y}{b} + a_{31} \cos\frac{3\pi x}{a} \cos\frac{\pi y}{b} + a_{24} \sin\frac{2\pi x}{a} \sin\frac{4\pi y}{b} + \ldots \quad (4)$$

After substituting eq 4 into eq 1 and performing the indicated integration by a numerical procedure, the integrals I_1 and I_2 become quadratic expressions in terms of the coefficients a_{11}, a_{22}, a_{13}, ... The critical value of τ_∞, the shear stress far from the hole, at which buckling of the plate occurs is that value of τ_∞ which reduces to zero the determinant of the coefficients of a_{11}, a_{22}, a_{13}, etc. in the set of simultaneous equations

$$\left.\begin{aligned}\frac{\partial I_1}{\partial a_{11}} + \tau_\infty \frac{\partial I_2}{\partial a_{11}} &= 0 \\ \frac{\partial I_1}{\partial a_{22}} + \tau_\infty \frac{\partial I_2}{\partial a_{22}} &= 0 \\ \frac{\partial I_1}{\partial a_{13}} + \tau_\infty \frac{\partial I_2}{\partial a_{13}} &= 0 \\ \ldots\ldots\ldots\ldots\end{aligned}\right\} \quad (5)$$

III. Numerical Integration

The evaluation of the integrals in eq 1 over the surface of the plate could not be done directly, since the plates have a rectangular outer boundary and a circular inner boundary and involve a stress that is a complicated function when expressed in rectangular coordinates.

The integral I_1, eq 1, was taken as

$$I_1 = I_{1a} + I_{1b} - I_{1c}, \quad (6)$$

where I_{1a} = the integral I_1 for the surface enclosed by the outer rectangular boundary of the plate, taking the flexural rigidity $D = D_1$, the value of D in the unreinforced portion of the plate;

I_{1b} = the integral I_1 for the surface enclosed by the outer circular boundary of the reinforcement taking $D = D_2 - D_1$, where D_2 is the value of D in the reinforcement;

I_{1c} = the integral I_1 for the surface enclosed by the circular boundary of the hole taking $D = D_2$.

The double integration necessary to evaluate I_{1a} could always be done directly, but this was not possible in evaluating I_{1b} and I_{1c}. The integrals I_{1b} and I_{1c} were obtained by integrating directly with respect to x and using Gauss' method of numerical integration, reference [5], for integrating with respect to y. In all cases except case 2, five Gauss points were used in this numerical integration as computations showed that, in increasing the number of points used from three to five, the value of the critical stress was changed only 2 percent. If more than five points had been used, the change in the value of the critical stress would have been even less. For case 2, three Gauss points were used in evaluating I_{1c} because the circular area over which I_{1c} was evaluated had a much smaller radius for case 2 than for the other cases.

The integral I_2 was evaluated as the sum of three integrals

$$I_2 = I_{2a} + I_{2b} + I_{2c}, \quad (7)$$

where I_{2a} = the integral I_2 for the circular disk of the reinforced area (A, fig. 1);

I_{2b} = the integral I_2 for the circular disk between the outer boundary of the reinforcement and the largest inscribed circle in the plate (B, fig. 1;

I_{2c} = the integral I_2 for the remainder of the plate (C, fig. 1).

The integral for each circular portion was determined, using Gauss' method of numerical inte-

gration, by first integrating numerically in a circumferential direction and then in a radial direction. The integral for the remainder of the plate was obtained also by using Gauss' method, first integrating numerically in the x-direction and then in the y-direction.

A typical distribution of Gauss points for computing I_2 is shown in figure 2 for one-eighth of a square plate with a central circular hole. For this distribution, the integral of a function F over the portion of the plate surface enclosed by heavy lines in figure 2 is

$$\left.\begin{aligned}\iint F dA = \frac{a^2}{8}\,[&0.0481444F_1+0.0770310F_2+0.0481444F_3+0.0380048F_4+0.0571868F_5+\\ &0.0914988F_6+0.0571868F_7+0.0727220F_8+0.116355F_9+0.0727220F_{10}+\\ &0.0337158F_{11}+0.0539452F_{12}+0.0337158F_{13}+0.0142967F_{14}+0.0228747F_{15}+\\ &0.0142967F_{16}+0.0181805F_{17}+0.0290888F_{18}+0.0181805F_{19}+0.00842899F_{20}+\\ &0.0134864F_{21}+0.00842899F_{22}]\end{aligned}\right\} \quad (8)$$

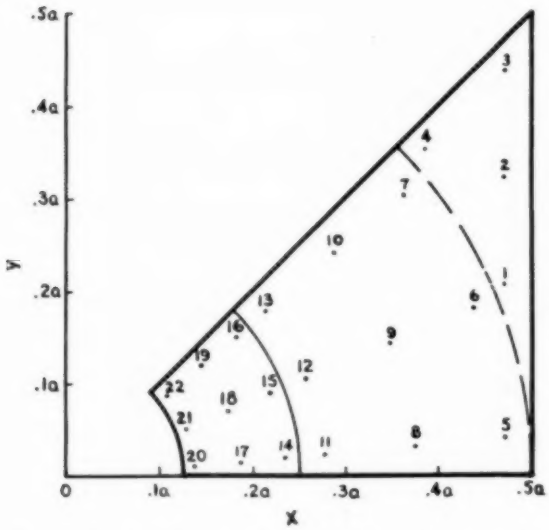

FIGURE 2. *Distribution of Gauss points for computing I_2 for case 3.*

Coordinates of points

Point	x/a	y/a	Point	x/a	y/a
1	0.469052	0.206523	12	0.257000	0.106453
2	.469052	.321115	13	.213318	.178541
3	.469052	.435706	14	.234988	.020855
4	.384501	.352062	15	.217954	.080280
5	.469978	.041709	16	.189008	.151415
6	.435910	.180559	17	.186766	.016575
7	.361818	.302851	18	.173228	.071753
8	.373532	.033150	19	.143784	.120343
9	.340455	.143506	20	.138543	.012285
10	.287568	.240986	21	.128501	.053227
11	.277066	.024591	22	.106659	.089271

where $F_1, F_2, F_3, \ldots F_{22}$ are values of the function F at the positions shown in Figure 2.

In each case a sufficient number of Gauss points was used to reduce the estimated error to less than 5 percent. Twenty-two points for each octant of the plate were used for cases 1, 3, and 4; twenty-eight points for case 2; and twenty-five points for case 5.

As an indication of the adequacy of the numerical integration methods used, the critical shear stress of a square plate without a hole was determined by approximating the deflection by

$$w = a_{11}\cos\frac{\pi x}{a}\cos\frac{\pi y}{a} + a_{22}\sin\frac{2\pi x}{a}\sin\frac{2\pi y}{a},$$

integrating for I_1, eq 1, exactly and integrating for I_2, eq 1, both exactly and by numerical integration with 22 points in one-eighth of the plate as shown in figure 3. The resulting critical stresses differed by 0.8 percent. In the case of a plate with a reinforced hole, it is probable that the more complicated stress distribution and the use and prominence of higher order terms in the series used for the deflection will cause the error to be somewhat higher.

IV. Convergence of Deflection Function

The correct value of τ_∞ for buckling of the plate is that value of τ_∞ which reduces the determinant of the coefficients of $a_{11}, a_{22}, a_{13}, \ldots$, in the infinite set of eq 5 to zero. In order to limit the work of computing τ_∞ to a finite amount, preliminary computations were made to deter-

mine which terms in the deflection function, eq 4, were most important in evaluating τ_∞. The computations were made for the plate of case 3, table 1.

TABLE 1. *Dimensions for square plates investigated*

Case	Length of side	Radius of hole, R	Outer radius of reinforcement	Thickness	
				Reinforced region	Unreinforced region
1	a	0.125 a	(*)	(*)	h
2	a	.0625 a	(*)	(*)	h
3	a	.125 a	0.25 a	2.0 h	h
4	a	.125 a	.25 a	1.5 h	h
5	a	.125 a	.1875 a	3.4 h	h

* Hole in plate not reinforced.

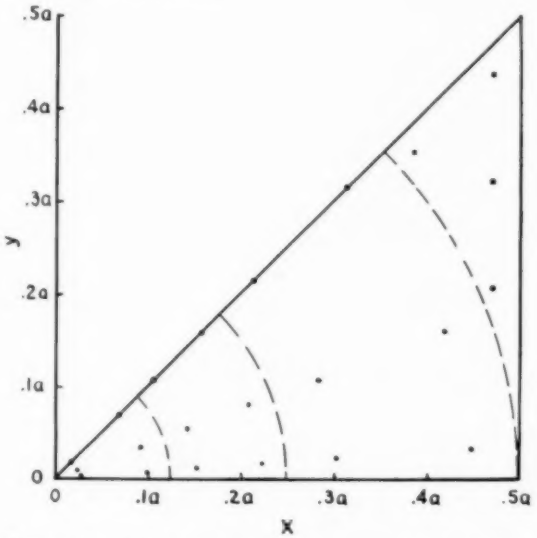

FIGURE 3. *Distribution of Gauss points for computing I_2 for case of plate without a hole.*

Using the distribution of points shown in figure 4 to carry out the numerical integration for I_2, the critical shear stress τ_∞ was 18.78 Eh^2/a^2 using only the first two terms of eq 4,

$$w=a_{11}\cos\frac{\pi x}{a}\cos\frac{\pi y}{a}+a_{22}\cos\frac{2\pi x}{a}\cos\frac{2\pi y}{a}.$$

Using as the deflection function

$$w=a_{11}\cos\frac{\pi x}{a}\cos\frac{\pi y}{a}+a_{22}\sin\frac{2\pi x}{a}\sin\frac{2\pi y}{a}+$$

$$a_{13}\cos\frac{\pi x}{a}\cos\frac{3\pi y}{a}+a_{31}\cos\frac{3\pi x}{a}\cos\frac{\pi y}{a},$$

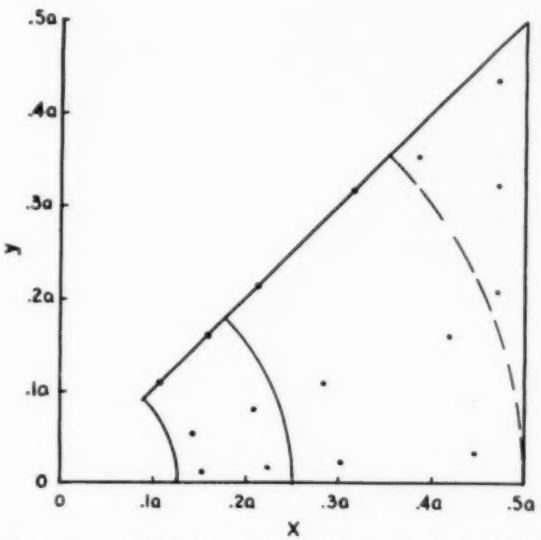

FIGURE 4. *Distribution of Gauss points for evaluating I_2 in study of convergence of deflection function.*

τ_∞ was 18.10 Eh^2/a^2, a decrease of 3.6 percent. Using

$$w=a_{11}\cos\frac{\pi x}{a}\cos\frac{\pi y}{a}+a_{22}\sin\frac{2\pi x}{a}\sin\frac{2\pi y}{a}+$$

$$a_{33}\cos\frac{3\pi x}{a}\cos\frac{3\pi y}{a},$$

τ_∞ was 17.46 Eh^2/a^2, a decrease of 7.0 percent. Using

$$w=a_{11}\cos\frac{\pi x}{a}\cos\frac{\pi y}{a}+a_{22}\sin\frac{2\pi x}{a}\sin\frac{2\pi y}{a}+$$

$$a_{24}\sin\frac{2\pi x}{a}\sin\frac{4\pi y}{a}+a_{42}\sin\frac{4\pi x}{a}\sin\frac{2\pi y}{a},$$

τ_∞ was 17.37 Eh^2/a^2, a decrease of 7.5 percent. Using

$$w=a_{11}\cos\frac{\pi x}{a}\cos\frac{\pi y}{a}+a_{22}\sin\frac{2\pi x}{a}\sin\frac{2\pi y}{a}+$$

$$a_{35}\cos\frac{3\pi x}{a}\cos\frac{5\pi y}{a}+a_{53}\cos\frac{5\pi x}{a}\cos\frac{3\pi y}{a},$$

τ_∞ was 18.50 Eh^2/a^2, a decrease of 1.5 percent. Using

$$w=a_{11}\cos\frac{\pi x}{a}\cos\frac{\pi y}{a}+a_{22}\sin\frac{2\pi x}{a}\sin\frac{2\pi y}{a}+$$

$$a_{44}\sin\frac{4\pi x}{a}\sin\frac{4\pi y}{a},$$

τ_∞ was 18.58 Eh^2/a^2, a decrease of 1.1 percent.

The use of additional terms of the trigonometric series with the first two terms probably would have shown a proportionately smaller decrease in the buckling load. Therefore, it is believed that the function

$$w=a_{11}\cos\frac{\pi x}{a}\cos\frac{\pi y}{a}+a_{22}\sin\frac{2\pi x}{a}\sin\frac{2\pi y}{a}+$$
$$a_{33}\cos\frac{3\pi x}{a}\cos\frac{3\pi y}{a}+a_{24}\sin\frac{2\pi x}{a}\sin\frac{4\pi y}{a}+$$
$$a_{42}\sin\frac{4\pi x}{a}\sin\frac{2\pi y}{a},$$

approximated the lateral deflection of a square plate with simply supported edges under shearing loads with sufficient accuracy. This deflection function was used in the computations of the critical shearing stresses.

After the critical shearing stresses had been computed for the five square plates considered in this report, the relative importance of the various terms in the deflection function was determined. Values of a_{22} were 25 to 42 percent of a_{11}; coefficients a_{33}, a_{24}, and a_{42} were 0.4 to 5.0 percent of a_{11}. It seems reasonable to assume that higher order terms would have been even smaller as compared to a_{11} and that the most important terms were used for the deflection in all cases.

The number of points used in the numerical integration for I_2 has an effect on the accuracy of the determination of the critical stress. To carry out a complete investigation of convergence, as more points are used, was not possible because of the amount of work involved. To obtain a partial indication of the accuracy to be expected, however, the critical stress for case 3, table 1, was computed using various deflection functions and using both the distribution of points in figure 2 and that in figure 4 for computing I_2. The results are given in table 2.

TABLE 2. *Values of critical stress obtained from the spacings of Gauss points investigated*

Terms in deflection function eq 4	Critical stress using points in figure 4 for I_2 τ_{cr}	Critical stress using points in figure 2 for I_2 τ_{cr}	Difference
			Percent
a_{11},a_{22}	18.78 Eh^2/a^2	20.05 Eh^2/a^2	7
a_{11},a_{22},a_{33}	17.46 Eh^2/a^2	18.56 Eh^2/a^2	6
$a_{11},a_{22},a_{24},a_{42}$	17.37 Eh^2/a^2	18.21 Eh^2/a^2	5
$a_{11},a_{22},a_{33},a_{55}$	18.50 Eh^2/a^2	19.58 Eh^2/a^2	6

It was decided on the basis of these computations that the use of the point distribution in figure 2 would be acceptable.

The over-all accuracy of the computations of critical stress are estimated to be such that the critical stresses are within 7 percent of the exact values for the cases investigated.

V. Results and Discussion

The critical shear stress was determined for five square plates with reinforced and unreinforced holes, figure 5. The dimensions for the plates are given in table 1.

The analysis gave the critical shear stress far from the hole τ_∞, corresponding to the stress distribution for a plate under uniform shear at an infinite distance from the hole. The shear stress τ_∞ is larger than the average shear stress on the

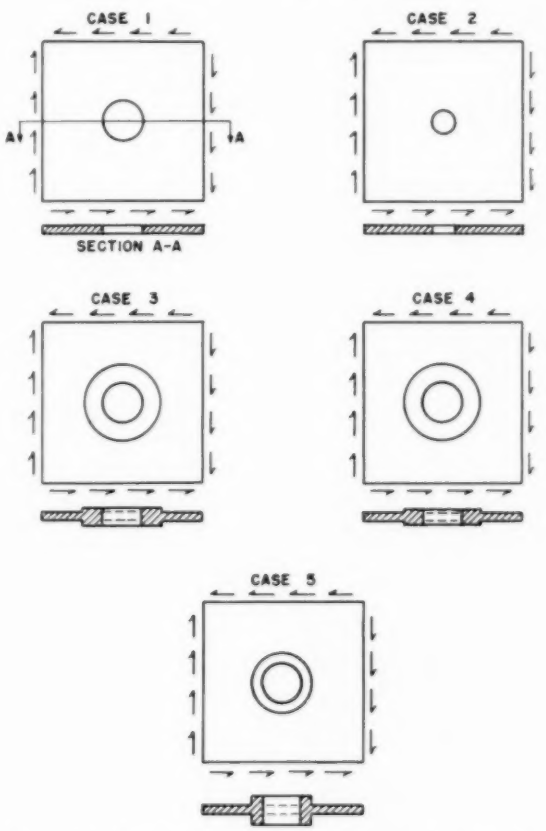

FIGURE 5. *Loading of square plates with simply supported edges. (Dimensions in table 1.)*

center cross section obtained by dividing the load on that section by ah. A better value of the average buckling stress τ_{cr} of the plate was obtained from

$$\tau_{cr}=\frac{1}{2}\frac{P_1+P_2}{ah}, \tag{9}$$

where P_1 = shearing force acting on edge of plate;
P_2 = shearing force transmitted across center section, $y=0$.

The value of P_1 was obtained by numerical integration and the value of P_2 by direct integration of the stresses τ_{xy} given by eq 3. Values of τ_∞, $\tau_1=P_1/ah$, $\tau_2=P_2/ah$, and τ_{cr} are given in table 3.

TABLE 3. *Critical shear stress for plates investigated*

Case	τ_∞	τ_1	τ_2	τ_{cr}
0	.....	.....	.....	$8.44\frac{Eh^2}{a^2}$
1	$6.95\frac{Eh^2}{a^2}$	$6.94\frac{Eh^2}{a^2}$	$6.11\frac{Eh^2}{a^2}$	$6.53\frac{Eh^2}{a^2}$
2	$8.55\frac{Eh^2}{a^2}$	$8.55\frac{Eh^2}{a^2}$	$8.29\frac{Eh^2}{a^2}$	$8.42\frac{Eh^2}{a^2}$
3	$17.47\frac{Eh^2}{a^2}$	$17.52\frac{Eh^2}{a^2}$	$17.01\frac{Eh^2}{a^2}$	$17.27\frac{Eh^2}{a^2}$
4	$10.45\frac{Eh^2}{a^2}$	$10.46\frac{Eh^2}{a^2}$	$9.78\frac{Eh^2}{a^2}$	$10.12\frac{Eh^2}{a^2}$
5	$28.83\frac{Eh^2}{a^2}$	$28.86\frac{Eh^2}{a^2}$	$27.80\frac{Eh^2}{a^2}$	$28.33\frac{Eh^2}{a^2}$

It was assumed that the boundaries of the square plates were sufficiently far from the hole so that only a uniform shear was acting on the boundaries. Numerical integration of the stresses σ_x as given by eq 3 on the boundary of the plate showed that there was an average compressive stress on half the side of the plate and a tensile stress on the other half equal to 3 to 12 percent of the shear stress. This accounts for the small differences in the values of τ_1 and τ_2.

The shear buckling stress of a simply supported square plate of constant thickness is given on page 360 of reference [6] (taking Poisson's ratio as 0.3) as

$$\tau_{cr}=8.44\ Eh^2/a^2. \tag{10}$$

Comparison of this value, case 0, table 3, with the values of the critical stresses for cases 1 and 2 shows that the unreinforced holes of diameter one-fourth and one-eighth the length of a side reduced the buckling stresses by 22.6 and 0.2 percent, respectively. Comparison of the value for case 0 with the values for cases 3 to 5 of table 3 shows that reinforcement of the hole increased the shear buckling stress of the plate over that for a plate without a hole from 20 to 236 percent. These percentages are to be taken only as indications of the order of magnitude since the accuracy of the present determination of critical stresses is estimated to be 7 percent.

The effect of thickness of the reinforcement on the buckling load is seen by comparing cases 3 and 4, table 3. In these cases, the hole size and area of the reinforcing material is the same, but the thickness of the reinforcement of case 4 is only one-half the thickness of the reinforcement of case 3. The buckling load for case 3 is 71 percent higher than that for case 4.

The effect of shape of reinforcement on the critical shear stress is indicated by comparing cases 3 and 5, table 3. The volume of material reinforcing the holes in these two cases is the same, but the reinforcing material is concentrated nearer the edge of the hole in case 5 than it is in case 3. The buckling stress is 64 percent greater for case 5 than for case 3.

Comparison of the values for case 1 and cases 3 to 5 shows that reinforcement of the hole raises the critical shear stress from 55 to 334 percent, depending on the thickness and shape of the reinforcement.

VI. Conclusions

Using a numerical procedure for evaluating the integrals for the energy stored in a plate, the critical shear stress can be estimated for plates with circular holes and doubler plate reinforcement.

The critical shearing stress of plates may be reduced considerably by the presence of unreinforced holes. A square plate with a hole diameter one-eighth the length of a side showed practically no reduction in critical shearing stress, but a square plate with a hole diameter twice as long showed a reduction of 23 percent.

Reinforcement of the doubler plate type causes marked increases in the critical shear stress. The critical shearing stresses were 55 to 334 percent higher than that for a plate with the same size unreinforced hole.

The volume and shape of the reinforcement has a marked effect on the critical shearing stress. The critical stresses for two plates with the same size hole and same area of reinforcement, but different thickness, were compared. The critical stress increased from 10.12 Eh^2/a^2 to 17.27 Eh^2/a^2, an increase of 71 percent, when the thickness of the reinforced region was increased from 1.5 h to 2.0 h. The critical stresses for two plates with the same size hole and same volume of reinforcing material were compared. The plate with the material concentrated closer to the edge of the hole had a 64 percent larger critical shearing stress.

VII. References

[1] Samuel Levy, A. E. McPherson, and F. C. Smith, Reinforcement of a small circular hole in a plane sheet under tension, J. Applied Mechanics, ASME **15,** No. 2 (June 1948).

[2] Wilhelmina D. Kroll, and A. E. McPherson, Compression tests of curved panels with circular hole reinforced with doubler plates, J. Aeronautical Sci. **16,** No. 6 (June 1949).

[3] Samuel Levy, and Frank C. Smith, Stress distribution near reinforced circular hole loaded by pin, J. Research NBS **42,** 397 (1949) RP1979.

[4] Samuel Levy, Ruth M. Woolley, and Wilhelmina D Kroll, Instability of simply supported square plate with reinforced circular hole in edge compression, J. Research NBS **39,** 571 (1947) RP1849.

[5] E. T. Whittaker, and G. Robinson, Calculus of observations (Blackie and Son, Ltd., London, 1944).

[6] S. Timoshenko, Theory of elastic stability (McGraw-Hill Book Co., New York, N. Y., 1936).

Washington, May 18, 1949.

U. S. Department of Commerce
National Bureau of Standards

Research Paper RP2038
Volume 43, November 1949

Part of the Journal of Research of the National Bureau of Standards

Physical Properties of Sixty API-NBS Hydrocarbons [1]

By Alphonse F. Forziati [2] and Frederick D. Rossini

The results of experimental determinations of the density at 20°, 25°, and 30° C, the refractive index, n_D, at 20°, 25°, and 30° C, and the boiling point and pressure coefficient of the boiling point, at 1 atmosphere, are reported for 60 hydrocarbons of the API-NBS series, including 17 paraffins, 14 alkylcyclopentanes, 8 alkylcyclohexanes, and 21 alkylbenzenes.

I. Introduction

As part of the work of the American Petroleum Institute Research Project 6 on the fractionation, analysis, purification, and properties of hydrocarbons, measurements are being made of the physical properties of the API-NBS series of highly purified hydrocarbons. This paper gives the results of measurements of refractive index, density, and boiling point of 60 API-NBS hydrocarbons, including 17 paraffins, 14 alkylcyclopentanes, 8 alkylcyclohexanes, and 21 alkylbenzenes.

II. Compounds Investigated

The compounds whose properties were measured in the present investigation were samples from the API-NBS series of highly purified hydrocarbons, which are being prepared through a cooperative undertaking of the American Petroleum Institute and the National Bureau of Standards.

These samples of API-NBS hydrocarbons have been made available by the American Petroleum Institute and the National Bureau of Standards through the API Research Project 44 on the "Collection, Analysis, Calculation, and Compilation of Data on the Properties of Hydrocarbons". The samples were purified at the National Bureau of Standards by the API Research Project 6 on the "Analysis, Purification, and Properties of Hydrocarbons", from material supplied by the following laboratories:

n-Heptane, 2,4-dimethylpentane, *n*-nonane, 2,2,5-trimethylhexane, benzene, 1,2,3-trimethylbenzene, and 1,2,4-trimethylbenzene, by the American Petroleum Institute Research Project 6 at the National Bureau of Standards.

2-Methylhexane and 3-methylhexane, by the Ethyl Corporation, Detroit, Mich.

3-Ethylpentane, 3,3-dimethylpentane, 3,3-diethylpentane, 2,2,3,3-tetramethylpentane, *cis*-1,3-dimethylcyclopentane, *trans*-1,3-dimethylcyclopentane, *n*-propylcyclopentane, isopropylcyclopentane, 1,1-dimethylcyclohexane, *n*-propylcyclohexane, isopropylcyclohexane, 1,1,3-trimethylcyclohexane, *n*-butylcyclohexane, isobutylcyclohexane, sec-butylcyclohexane, tert-butylcyclohexane, 1,3-dimethylbenzene, 1,4-dimethylbenzene, 1-methyl-2-ethylbenzene, 1-methyl-3-ethylbenzene, 1,3,5-trimethylbenzene, *n*-butylbenzene, isobutylbenzene, sec-butylbenzene, and tert-butylbenzene, by the American Petroleum Institute Research Project 45, at the Ohio State University, Columbus, Ohio, under the supervision of C. E. Boord.

2,2-Dimethylpentane, by the Socony-Vacuum Laboratories, Paulsboro, N. J.

2,3-Dimethylpentane and 2,2,3-trimethylbutane, by General Motors Corporation, Detroit, Mich.

2,4,4-Trimethylhexane, 1,1-dimethylcyclopentane, *cis*-1,2-dimethylcyclopentane, *trans*-1,2-dimethylcyclopentane, 1,1,2-trimethylcyclopentane, *cis,cis,trans*-1,2,4-trimethylcyclopentane, *cis,trans,cis*-1,2,4-trimethylcyclopentane, 1-methyl-1-ethylcyclopentane, and 1-methyl-*cis*-2-ethylcyclopentane, by the Hydrocarbon Laboratory, Pennsylvania State College, State College, Pa.

[1] This investigation was performed at the National Bureau of Standards as part of the work of the American Petroleum Institute Research Project 6 on the "Analysis, Purification, and Properties of Hydrocarbons."

[2] Research Associate on the American Petroleum Institute Research Project 6 at the National Bureau of Standards.

2,2,3,4-Tetramethylpentane, 2,2,4,4-tetramethylpentane, 2,3,3,4-tetramethylpentane, 1-methyl-4-ethylbenzene, 1,2-diethylbenzene, and 1,4-diethylbenzene, by the National Advisory Committee for Aeronautics, Flight Propulsion Research Laboratory, Cleveland, Ohio.

1,1,3-Trimethylcyclopentane, by the American Petroleum Institute Research Project 45, at the Ohio State University, Columbus, Ohio, and the Gulf Oil Company Fellowship, at the Mellon Institute of Industrial Research, Pittsburgh, Pa.

Ethylcyclopentane, by the American Petroleum Institute Research Project 45, Ohio State University, Columbus, Ohio, and the Hydrocarbon Laboratory, Pennsylvania State College, State College, Pa.

Methylbenzene, by the Humble Oil and Refining Company, Houston, Tex.

Ethylbenzene and isopropylbenzene, by the Monsanto Chemical Company, Dayton, Ohio.

1,2-Dimethylbenzene, by the Standard Oil Development Company, Elizabeth, N. J.

n-Propylbenzene, by the Dow Chemical Company, Midland, Mich.

1,3-Diethylbenzene, by the National Advisory Committee for Aeronautics, Flight Propulsion Research Laboratory, Cleveland, Ohio, and the American Petroleum Institute Research Project 45 at the Ohio State University, Columbus, Ohio.

The purification and determination of purity and freezing points of these compounds are described in references [1, 2, 3, 4, 5].[3]

[3] Figures in brackets indicate the literature references at the end of this paper.

It is believed that in each case the impurity was of such nature and present in such small amount that the properties measured were not affected beyond the indicated limits of uncertainty.

III. Refractive Indices

The measurements of refractive index were made with a precision refractometer,[4] by reference to the three hydrocarbons, 2,2,4-trimethylpentane, methylcyclohexane, and methylbenzene (toluene), for which the values of refractive index were determined on a spectrometer with hollow prism by L. W. Tilton, of the Optical Instruments Section of the National Bureau of Standards. These three hydrocarbons are NBS Standard Samples of hydrocarbons certified with respect to refractive index at 20°, 25°, and 30° C. The values of refractive index for the three reference hydrocarbons were reported with an accuracy of ± 0.00001, and were used as follows: 2,2,4-trimethylpentane for the paraffin hydrocarbons, methylcyclohexane for the cycloparaffin hydrocarbons, and methylbenzene for the alkylbenzene hydrocarbons. By this procedure, the refractometer was actually used only to determine the difference in refractive index, n_D, between the reference compound and the hydrocarbon under investigation. The experimental results on refractive index are given in table 1. Individual measurements were reproducible within ± 0.00002 to ± 0.00003. The accuracy of the tabulated values, including the effect of impurities, is estimated to be ± 0.00005 to ± 0.00008.

[4] Modified Abbe-type, Bausch and Lomb.

TABLE 1. *Values of refractive index, density, and boiling point for sixty API–NBS hydrocarbons*

Compound	Formula	Boiling point at 760 mm Hg	Pressure coefficient of boiling point at 760 mm Hg dt/dP	Refractive index n_D			Temperature coefficient of refractive index (n_D) at 25° C	Density			Temperature coefficient of density at 25° C
				20° C	25° C	30° C		20° C	25° C	30° C	
PARAFFINS											
		° C	°C/mmHg				1/° C	g/ml	g/ml	g/ml	g/ml °C
n-Heptane	C_7H_{16}	98.427	0.04481	1.38764	1.38511	1.38258	0.000506	0.68376	0.67951	0.67526	0.000850
2-Methylhexane	C_7H_{16}	90.052	.04431	1.38485	1.38227	1.37969	.000516	.67859	.67439	.67001	.000858
3-Methylhexane	C_7H_{16}	91.850	.04459	1.38864	1.38609	1.38354	.000510	.68713	.68295	.67852	.000861
3-Ethylpentane	C_7H_{16}	93.475	.04482	1.39339	1.39084	1.38829	.000510	.69816	.69395	.68948	.000868
2,2-Dimethylpentane	C_7H_{16}	79.197	.04394	1.38215	1.37955	1.37695	.000520	.67385	.66953	.66508	.000877
2,3-Dimethylpentane	C_7H_{16}	89.784	.04482	1.39196	1.38945	1.38694	.000502	.69508	.69091	.68650	.000858
2,4-Dimethylpentane	C_7H_{16}	80.500	.04376	1.38145	1.37882	1.37619	.000526	.67270	.66832	.66383	.000887
3,3-Dimethylpentane	C_7H_{16}	86.064	.04509	1.38982	1.38842	1.38592	.000500	.69327	.68908	.68481	.000846
2,2,3-Trimethylbutane	C_7H_{16}	80.882	.04484	1.38944	1.38692	1.38440	.000504	.69011	.68588	.68154	.000857
n-Nonane	C_9H_{20}	150.798	.04967	1.40542	1.40311	1.40080	.000462	.71763	.71381	.70994	.000768
2,2,5-Trimethylhexane	C_9H_{20}	124.084	.04838	1.39972	1.39728	1.39484	.000488	.70721	.70322	.69905	.000816
2,4,4-Trimethylhexane	C_9H_{20}	130.648	.04960	1.40745	1.40515	1.40285	.000460	.72381	.72007	.71612	.000769
3,3-Diethylpentane	C_9H_{20}	146.168	.05109	1.42051	1.41837	1.41623	.000428	.75359	.75000	.74634	.000725
2,2,3,3-Tetramethylpentane	C_9H_{20}	140.274	.05124	1.42360	1.42140	1.41920	.000440	.75666	.75299	.74925	.000741
2,2,3,4-Tetramethylpentane	C_9H_{20}	133.016	.05030	1.41472	1.41246	1.41020	.000452	.73895	.73524	.73144	.000751
2,2,4,4-Tetramethylpentane	C_9H_{20}	122.284	.04937	1.40694	1.40459	1.40224	.000470	.71947	.71563	.71167	.000780
2,3,3,4-Tetramethylpentane	C_9H_{20}	141.551	.04223	1.42222	1.42003	1.41784	.000438	.75473	.75113	.74740	.000733
ALKYLCYCLOPENTANES											
Ethylcyclopentane	C_7H_{14}	103.466	0.04623	1.41981	1.41730	1.41479	0.000502	0.76947	0.76217	0.75780	0.000867
1,1-Dimethycyclopentane	C_7H_{14}	87.846	.04497	1.41356	1.41091	1.40826	.000530	.75448	.74991	.74532	.000916
cis-1,2-Dimethylcyclopentane	C_7H_{14}	99.532	.04603	1.42217	1.41963	1.41709	.000508	.77262	.76807	.76364	.000898
trans-1,2-Dimethylcyclopentane	C_7H_{14}	91.899	.04521	1.41200	1.40941	1.40682	.000518	.75144	.74686	.74241	.000903
cis-1,3-Dimethylcyclopentane	C_7H_{14}	91.725	.04525	1.41074	1.40813	1.40552	.000522	.74980	.74435	.73985	.000895
trans-1,3-Dimethylcyclopentane	C_7H_{14}	90.773	.04518	1.40894	1.40633	1.40372	.000522	.74479	.74025	.73573	.000906
n-Propylcyclopentane	C_8H_{16}	130.949	.04888	1.42626	1.42389	1.42152	.000474	.77633	.77229	.76811	.000822
Isopropycyclopentane	C_8H_{16}	126.419	.04913	1.42582	1.42350	1.42118	.000464	.77653	.77259	.76851	.000802
1-Methyl-1-ethylcyclopentane	C_8H_{16}	121.522	.04863	1.42718	1.42476	1.42234	.000484	.78093	.77670	.77260	.000833
1-Methyl-*cis*-2-ethycyclopentane	C_8H_{16}	128.050	.04897	1.42933	1.42695	1.42457	.000476	.78522	.78113	.77698	.000824
1-1-2,Trimethylcyclopentane	C_8H_{16}	113.729	.04818	1.42298	1.42051	1.41804	.000494	.77252	.76817	.76399	.000853
1,1,3-Trimethylcyclopentane	C_8H_{16}	104.893	.04724	1.41119	1.40870	1.40621	.000498	.74825	.74392	.73958	.000867
cis, cis, trans-1,2,4-Trimethylcyclopentane	C_8H_{16}	116.731	.04827	1.41855	1.41612	1.41369	.000486	.76345	.75920	.75504	.000841
cis, trans, cis-1,2,4-Trimethylcyclopentane	C_8H_{16}	109.290	.04738	1.41060	1.40812	1.40564	.000496	.74727	.74302	.73873	.000854
ALKYLCYCLOHEXANES											
1,1-Dimethylcyclohexane	C_8H_{16}	119.543	0.04920	1.42900	1.42662	1.42424	0.000476	0.78094	0.77677	0.77276	0.000818
n-Propylcyclohexane	C_9H_{18}	156.724	.05200	1.43705	1.43478	1.43251	.000454	.79890	.79477	.78781	.000779
Isopropylcyclohexane	C_9H_{18}	154.563	.05210	1.44087	1.43861	1.43635	.000452	.80221	.79833	.79444	.000777
1,1,3-Trimethylcyclohexane	C_9H_{18}	136.626	.05089	1.42955	1.42725	1.42495	.000460	.77883	.77497	.77100	.000783
n-Butylcyclohexane	$C_{10}H_{20}$	180.947	.05412	1.44075	1.43855	1.43635	.000440	.79918	.79551	.79176	.000742
Isobutylcyclohexane	$C_{10}H_{20}$	171.321	.05307	1.43861	1.43636	1.43411	.000450	.79521	.79141	.78750	.000771
sec-Butylcyclohexane	$C_{10}H_{20}$	179.335	.05440	1.44673	1.44454	1.44235	.000438	.81314	.80935	.80565	.000749
tert-Butylcyclohexane	$C_{10}H_{20}$	171.591	.05429	1.44694	1.44473	1.44252	.000442	.81267	.80880	.80513	.000754
ALKYLBENZENES											
Benzene	C_6H_6	80.099	0.04271	1.50112	1.49792	1.49478	0.000635	0.87901	0.87370	0.86846	0.001055
Methylbenzene (Toluene)	C_7H_8	110.626	.04630	1.49683	1.49414	1.49126	.000567	.89094	.88520	.85770	.000924
Ethylbenzene	C_8H_{10}	136.186	.04808	1.49588	1.49320	1.49050	.000534	.86702	.86264	.85828	.000874
1,2-Dimethylbenzene (*o*-Xylene)	C_8H_{10}	144.411	.04969	1.50545	1.50285	1.50032	.000513	.88020	.87586	.87186	.000831
1,3-Dimethylbenzene (*m*-Xylene)	C_8H_{10}	139.104	.04903	1.49722	1.49464	1.49198	.000518	.86417	.85980	.85565	.000852
1,4-Dimethylbenzene (*p*-Xylene)	C_8H_{10}	138.351	.04917	1.49582	1.49325	1.49054	.000537	.86105	.85660	.85246	.000859
n-Propylbenzene	C_9H_{12}	159.218	.05143	1.49202	1.48951	1.48702	.000500	.86204	.85780	.85370	.000834

See footnote at end of table.

TABLE 1. *Values of refractive index, density, and boiling point for sixty API–NBS hydrocarbons*—Continued

Compound	Formula	Boiling point at 760 mm Hg	Pressure coefficient of boiling point at 760 mm Hg dt/dP	Refractive index [a] n_D			Temperature coefficient of refractive index (n_D) at 25° C	Density [a]			Temperature coefficient of density at 25° C
				20° C	25° C	30° C		20° C	25° C	30° C	
ALKYLBENZENES—Continued											
		°C	°C/mmHg				1/° C	g/ml	g/ml	g/ml	g/ml/° C
Isopropylbenzene (Cumene)	C_9H_{12}	152.392	.05074	1.49145	1.48890	1.48646	.000499	.86179	.85751	.85335	.000844
1-Methyl-2-ethylbenzene	C_9H_{12}	165.153	.05163	1.50456	1.50208	1.49963	.000493	.88069	.87657	.87252	.000817
1-Methyl-3-ethylbenzene	C_9H_{12}	161.305	.05111	1.49660	1.49406	1.49154	.000511	.86452	.86040	.85630	.000822
1-Methyl-4-ethylbenzene	C_9H_{12}	161.989	.05148	1.49500	1.49244	1.48989	.000497	.86118	.85702	.85290	.000819
1,2,3-Trimethylbenzene (Hemimellitene)	C_9H_{12}	176.084	.05263	1.51393	1.51150	1.50911	.000482	.89438	.89044	.88652	.000786
1,2,4-Trimethylbenzene (Pseudocumene)	C_9H_{12}	169.351	.05187	1.50484	1.50237	1.49980	.000493	.87582	.87180	.86782	.000800
1,3,5-Trimethylbenzene (Mesitylene)	C_9H_{12}	164.716	.05100	1.49937	1.49684	1.49437	.000500	.86518	.86111	.85707	.000811
n-Butylbenzene (1-Phenylbutane)	$C_{10}H_{14}$	183.270	.05358	1.48979	1.48742	1.48502	.000477	.86013	.85607	.85218	.000795
Isobutylbenzene (1-Phenyl-2-methylpropane)	$C_{10}H_{14}$	172.759	.05319	1.48646	1.48400	1.48157	.000492	.85321	.84907	.84512	.000809
sec-Butylbenzene (2-Phenylbutane	$C_{10}H_{14}$	173.305	.05313	1.49020	1.48779	1.48537	.000482	.86207	.85797	.85405	.000802
tert-Butylbenzene (2-Phenyl-2-methylpropane)	$C_{10}H_{14}$	169.119	.05269	1.49266	1.49024	1.48776	.000490	.86650	.86240	.85834	.000816
1,2-Diethylbenzene	$C_{10}H_{14}$	183.423	.05340	1.50346	1.50106	1.49865	.000481	.87996	.87592	.87197	.000799
1,3-Diethylbenzene	$C_{10}H_{14}$	181.102	.05293	1.49552	1.49310	1.49067	.000485	.86394	.85983	.85580	.000804
1,4-Diethylbenzene	$C_{10}H_{14}$	183.752	.05351	1.49483	1.49245	1.49003	.000480	.86196	.85794	.85402	.000794

[a] For air-saturated hydrocarbon in the liquid state at 1 atmosphere.

IV. Densities

The measurements of density were made with a density balance, the assembly, calibration, and operation of which has been previously described [6]. The experimental results on density are given in table 1. Individual measurements were reproducible within ±0.00002 to ±0.00003 g/ml. The accuracy of the tabulated values, including the effect of impurities, is estimated to be ±0.00005 to ±0.00010 g/ml.

V. Boiling Points

The normal boiling points of these compounds were determined as part of another investigation on their vapor pressure, and the values reported in table 1 for the normal boiling point and the pressure coefficient of the boiling point at 1 atmosphere are taken directly from the report of that investigation [7]. Individual measurements of the normal boiling point were reproducible within ±0.002 deg to ±0.003 deg C. The accuracy of the tabulated values of the normal boiling point, including the effect of impurities, is estimated to be ±0.005 deg to ±0.010 deg C.

VI. References

[1] A. R. Glasgow, Jr., E. T. Murphy, C. B. Willingham, and F. D. Rossini, J. Research NBS **37,** 141 (1946) RP1734.

[2] A. J. Streiff, E. T. Murphy, V. A. Sedlak, C. B. Willingham, and F. D. Rossini, J. Research NBS **37,** 331 (1946) RP1752.

[3] A. J. Streiff, E. T. Murphy, J. C. Cahill, H. F. Flanagan, V. A. Sedlak, C. B. Willingham, and F. D. Rossini, J. Research NBS **38,** 53 (1947) RP1760

[4] A. J. Streiff, E. T. Murphy, J. C. Zimmerman, L. F. Soule, V. A. Sedlak, C. B. Willingham, and F. D. Rossini, J. Research NBS **39,** 321 (1947) RP1833.

[5] A. J. Streiff, J. C. Zimmerman, L. F. Soule, M. T. Butt, V. A. Sedlak, C. B. Willingham, and F. D. Rossini, J. Research NBS **41,** 323 (1948) RP1929.

[6] A. F. Forziati, B. J. Mair, and F. D. Rossini, J. Research NBS **35,** 513 (1945) RP1685.

[7] A. F. Forziati, W. R. Norris, and F. D. Rossini, Bureau of Standards (publication pending).

WASHINGTON, June 3, 1949.

U. S. Department of Commerce
National Bureau of Standards

Research Paper RP2039
Volume 43, November 1949

Part of the Journal of Research of the National Bureau of Standards

Fatigue Characteristics of Electroformed Sheets with and without Iron Backing

By Harry K. Herschman and Carroll Thomas[1]

The flexural fatigue properties were determined for electroformed sheets of iron-nicke. and iron-nickel-chromium, and of plates composed of electroformed iron nickel sheets bonded with solder or a plastic adhesive to open-hearth iron. The fatigue limit of the iron-nickel composite was decreased when a thin deposit of chromium was applied to the nickel face. Heating the iron-nickel-chromium sheets at 260° C (500° F) before machining improved their fatigue properties. Apparent further beneficial effects resulted by heating after machining. The fatigue limits of the plates bonded with the plastic adhesive were significantly higher than those joined by soldering. Two brushed coats of the plastic adhesive applied to the mating surfaces of the composite layers of the plates appeared somewhat more favorable to higher fatigue limits than a combination one brushed and one sprayed coat procedure.

I. Introduction

Structures or segments of structures frequently are prepared by bonding a metal or alloy having certain properties to another metal or nonmetallic material having wholly different properties. Such composites usually will have a combination of desired characteristics that no single material possesses. The joining of the constituent parts may be accomplished by various means, such as soldering, fusion welding, or adhesive cementing. Many of the intaglio printing plates used at the Bureau of Engraving and Printing are prepared by bonding an electroformed face shell composed of a layer of iron and a layer of nickel to a backing of open-hearth iron. Previously, soldering supplemented by spot welding was employed for joining these two segments. Because of failures in the solder-bonded plates, plastic adhesives have been replacing this method for securing the required bond between the electrolytic shell and the iron back.

The manner of affixing a plate on the printing-press bed causes a slight convexity of the printing surface when the plate is not in operation. The loading of the plate as it passes under the roll while printing tends to flatten the printing surface, resulting in a repeated flexing of the plate. It is this flexing action that causes failure by fatigue in some of the constituent layers of the electrolytically "built-up" shell, which is the portion of the plate subjected to the maximum tensile stresses. This has occurred particularly in the plates bonded with tin-lead solders. A number of factors, such as residual stress in the electroformed shell, the nature of the bonding agent, and brittle constituents at the interface of the iron layer of the electroplated shell and the solder may influence the fatigue properties of these composite plates. In order to ascertain how these factors affect the fatigue characteristics of the electroformed shells alone and as bonded to fabricated iron backs, their behavior under controlled fatigue stressing was investigated.

A review of the literature dealing with the fatigue properties of electroformed metals and of structures bonded with plastic adhesives or solders revealed only scant information on these subjects. A Navy report [2] on the mechanical properties of structures bonded with a plastic adhesive stated that a magnesium assembly joined with this adhesive still carried 100 percent of the design load after 10×10^6 cycles, whereas a similar structure assembled with rivets failed in 3×10^6 cycles. Similar results were reported by Westbrook [3] for

[1] Foreman, Electrolytic Section, Bureau of Engraving and Printing.

[2] Naval Air Experimental Station, Philadelphia Report (April 1, 1944).

[3] Adhesives for gluing thin metal sheets, F. A. Westbrook, Steel Processing 34, 26 (Jan. 1948).

lap joints secured both by riveting and adhesive cementing respectively. Grover and Jackson [4] found that lap joints of magnesium sheet secured with "Cycleweld" were stronger both statically and in fatigue than joints made by riveting and spot welding and were comparable in these respects with "Heliarc" welded joints. However, data showing the comparative fatigue properties of joints bonded with solders and adhesive cements respectively, do not appear to be available.

Most of the reports discussing the fatigue properties of electroplated metals consider them in connection with their influence as a coating on other metals or alloys. An unpublished report of Oberg and Powers [5] indicates that the flexural fatigue limit of 0.1-in. sheets of electroformed nickel "as deposited" is about 43,000 lb/in^2. Heating this sheet at 400° F for 2 hr increased the fatigue limit to 46,000 lb/in^2.

II. Materials and Specimens

The test specimens used in the first phase of this investigation were prepared from electroformed sheets (fig. 1) consisting of a layer each of iron and nickel and iron, nickel, and chromium. Those employed for the second part of the study were cut from plates prepared by bonding electroformed shells composed of a layer each of iron and nickel to open hearth iron backs (fig. 2).

The electroformed composite sheets of iron-nickel were prepared by first depositing a layer of nickel about 0.005 in. thick on a nickel-faced cathode, approximately 13 by 15 in. in area, the surface of which was covered with a very thin film of flake graphite to facilitate separation of the electroformed sheet. The cathode was then transferred to the iron bath, from which an iron layer about 0.1 in. thick was plated on the nickel deposit formed in the first step. The nickel-iron composite then was separated from the cathode, following which the sheet was ground on the iron surface to a finished thickness of approximately 0.075 in. In preparing the iron-nickel-chromium composites, the nickel and iron were plated as previously described. Then the nickel surface was electrolytically cleaned with a solution of 45 g of sodium hydroxide and 25 g of trisodium phosphate per liter of water, scrubbed with pumice moistened with 20 percent of hydrochloric acid and finally

[4] The fatigue strength of lap joints in some magnesium sheet alloys, H. J. Grover and L. R. Jackson, ASTM Tech. Pub. No. 72 (Symposium on testing parts and assemblies.)

[5] Private communication, T. T. Oberg and J. B. Powers, Wright, Patterson Air Force Base, Dayton, Ohio.

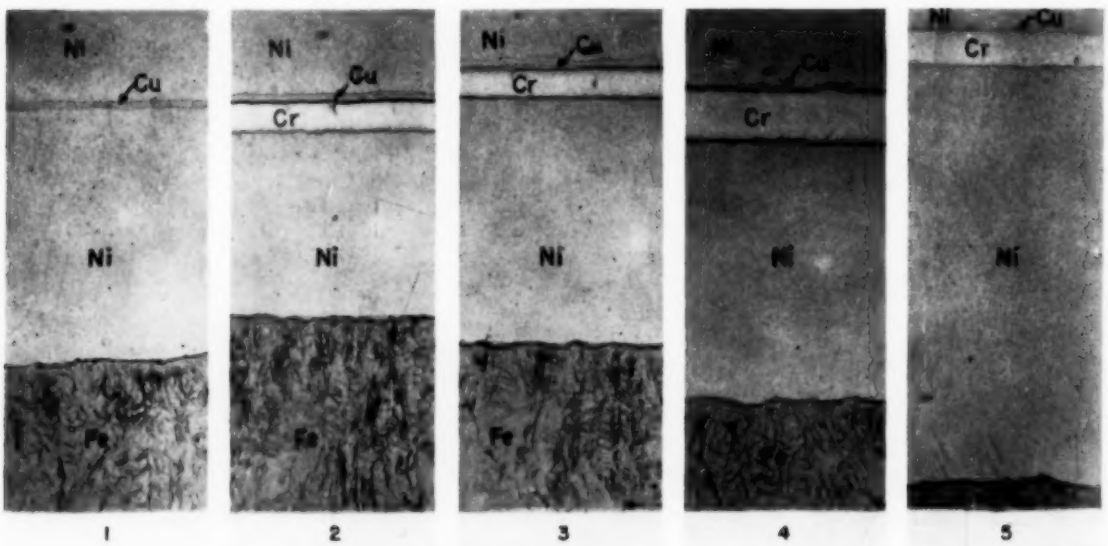

FIGURE 1. *Sections of fatigue specimens of electroformed sheet showing thickness of the nickel and chromium layers respectively.*

The layers of copper and nickel indicated at the top of the micrographs were applied to the metallographic specimens to prevent rounding of the adjacent edges of the specimens during polishing. Number designations of micrographs correspond to sheet numbers in table 1. Etched in 5 percent picral. Magnification ×500.

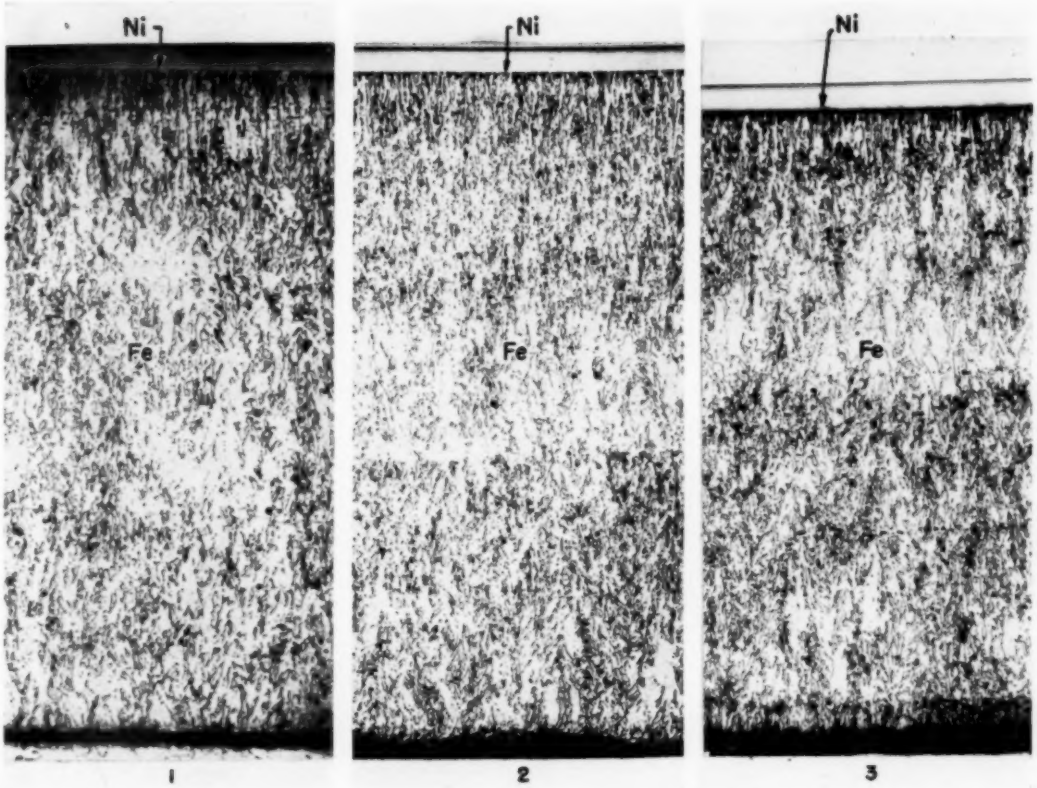

FIGURE 2. *Sections of fatigue specimens of printing plate composed of an electroformed portion of a layer each of iron and nickel bonded to a backing of open hearth iron.*

Number designations of micrographs correspond to plate numbers in table 2. Magnification ×50.

rinsed with water immediately prior to immersing the sheet in the chromium plating bath.

The conditions of plating and the compositions for the different electroplating baths employed were as follows:

(1) Nickel bath

$NiSO_4.7H_2O$	200 g/liter
$NiCl_2.6H_2O$	40 g/liter
H_3BO_3	20 g/liter

Current density=2 amp/square decimeter;
pH=5.1;
Temperature=40° C;
Time of plating=6 hr.

(2) Iron bath

$FeCl_2.4H_2O$	450 g/liter
$CaCl_2$	200 g/liter

Current density=7 amp/square decimeter;
pH=1.0;
Temperature=95° C;
Time of plating=36 hr.

(3) Chromium bath

CrO_3	250 g/liter
H_2SO_4	2.5 g/liter

Current density=27 amp/square decimeter;
Temperature=50° C;
Time of plating=40 min.

The thickness of each component layer of the electroformed composites, tested as such, are listed in table 1. The test specimens prepared from this sheet material were of the form and dimensions shown in figure 3. A number of the specimens prepared from the composite sheets 2 and 3 (table 1) (Numbers 2B and 3A, table 1) were tinned at 260° C (500° F) on the iron face in some cases and others (number 2A, table 1) were heated at this temperature without tinning. The edges of the specimens within their gage length were polished with 3/0 fine emery paper to remove

surface irregularities that might serve as centers of stress concentration and thereby act as nuclei for fatigue failures.

TABLE 1. *Fatigue limits of electroformed composite sheets of iron-nickel and iron-nickel-chromium*

Sheet No.	Electroformed of layers of	Thickness of layer *			Treatment	Fatigue limit (10^7 cycles)
		Iron	Nickel	Chromium		
		In.	*In.*	*In.*		*lb/in.²*
1	Iron-nickel	0.075	0.003	None	"As deposited"	45,000
2	Iron-nickel-chromium.	.074	0.0025	0.0003	do	41,500
2A	do	.074	.0025	.0003	Heated at 500° F for 5 min after machining.	44,000
2B	do	.074	.0025	.0003	Tinned at 500° F for 5 min after machining.	43,000
3	do	.072	.003	.0003	Heated to 500° F for 5 min before machining.	43,000
3A	do	.072	.003	.0003	Heated to 500° F for 5 min, machined, then tinned at 500° F.	44,000
4	do	.077	.003	.0006	Tinned at 500° F for 5 min before machining.	38,500
5	do	.073	.005	.0004	"As deposited"	40,500

* All plating was deposited with intermittent removal for "detreeing" except sheet 5, which was continuously deposited (no "detreeing").

TABLE 2. *Results of flexure fatigue tests on bonded plates*

Plate	Thickness of electroformed layer		Bonding agent	Fatigue limit (10^7 cycles)
	Iron	Nickel		
	in.	*in.*		*lb/in.²*
1	0.078	0.0028	2 brush coats of plastic adhesive.	46,000
2	.079	.003	1 brush and 1 spray coat of plastic adhesive.	43,000
3	.074	.003	50–50 tin-lead solder	40,000

The electroformed shells for the bonded plates were prepared in a manner essentially similar to that used for the electrolytic sheets described above. In every case they consisted of a layer each of iron and nickel of the respective thicknesses indicated in figure 2. These composites were ground on the iron face with a Blanchard grinder, and this surface then was cleaned by brushing with lime, pumice, and water. Finally it was washed with a 10-percent aqueous solution

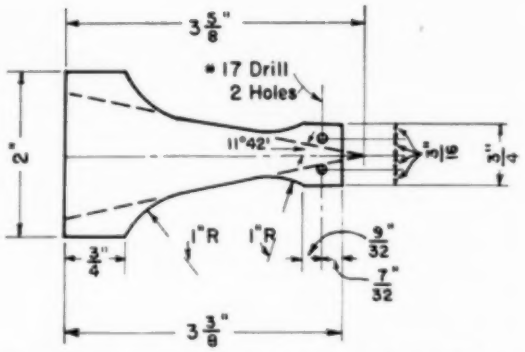

FIGURE 3. *Design of specimen used for determining the flexural fatigue properties of electroformed sheets.*

of hydrochloric acid. The bonding surfaces of the open hearth iron backs were similarly ground, cleaned, and treated with acid.

Soldering the electrolytic shell to the iron back was accomplished by fluxing the contacting iron surfaces with zinc chloride, sandwiching a 0.005-in.-thick sheet of 50–50 tin-lead solder between these surfaces, pressing them together at a temperature of 260° C (500° F) under a pressure of 80 lb/in.² in a press equipped with electrically heated plattens and cooling under pressure of 80 lb/in.² in a water-cooled press.

When the joints were made by adhesive cementing, the mating surfaces first were washed with an abrasive soap and water and then cleaned with steel wool. After thoroughly drying the surfaces, a coat of plastic adhesive was applied with a brush to each of them. Following a drying period of 30 min, a second coat of adhesive was applied, in some cases by brushing and in others by spraying, which also was allowed to dry in air for 30 min. These coatings then were dried at 85° C (185° F) for 25 min, after which the coated surfaces were mated and pressed together under a stress of approximately 80 lb/in.² at a temperature of 160° C (325° F) for 30 min.

The plates bonded by these methods had a nickel face and an iron back. Surface metal was removed from the iron backs by grinding with a Blanchard surface grinder until the plates were approximately 0.2 in. thick. Specimens of the form and dimensions shown in figure 4 were cut from these plates. In all cases, the edges of the specimens within the gage length were polished with fine (3/0 emery) abrasive paper to remove surface irregularities in the same manner and for

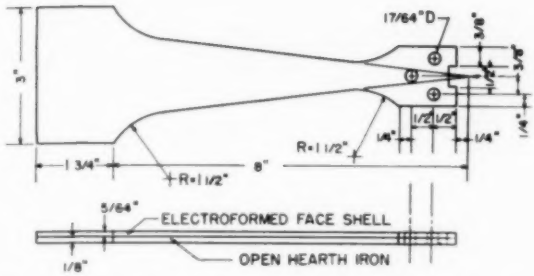

FIGURE 4. *Design of specimen used for determining the flexural fatigue properties of composite plates of electroformed nickel-iron shells bonded to open hearth iron backs.*

the same purposes as described for the electroformed sheet specimens.

III. Method of Test

The flexural fatigue tests were made on Krouse plate fatigue machines operating at 1,750 rpm. (fig. 5). The electroformed sheet and composite plate specimens in every case were adjusted in the machine so that the range of stress applied to the specimen face (nickel or chromium surface—see table 1) was from zero to maximum tension and the back (iron surface) was in zero to maximum compression. This stress cycle was used to simulate that to which a printing plate is subjected on the press.

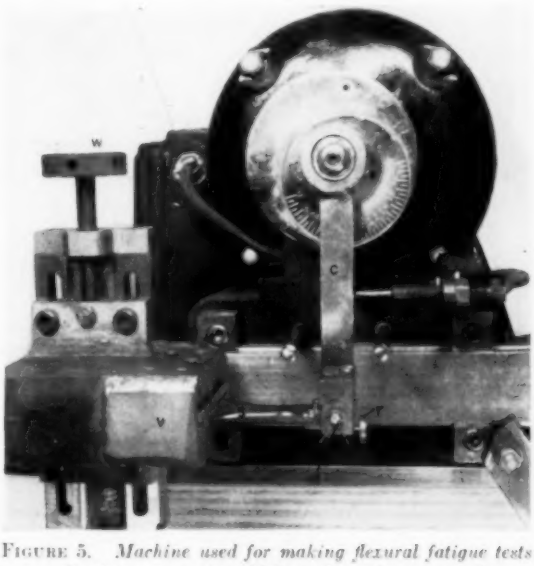

FIGURE 5. *Machine used for making flexural fatigue tests showing manner in which specimen is supported.*

s=specimen; v=vise for holding specimen in rigid position; w=screw for adjusting height of vise v; c=crank-arm for actuating specimen s; a=connecting pin for attaching arm c to specimen s; e=adjustable eccentric for varying throw of connecting arm c; r=reflecting mirror used for ascertaining specimen deflection in terms of stress as shown in figure 6.

The specimens were deflected to produce the maximum flexural stress by adjusting the eccentric (fig. 5, e) in the usual manner [6] except that the method used for measuring the deflection (fig. 6) was somewhat different from that generally employed with the Krouse flexure machine. Essentially it consisted of a flat mirror (*r*, fig. 5), attached to the adapter securing the specimen to the crank arm, which reflected a horizontally collimated beam of light to a 12-ft-long scale placed about 20 ft from the mirror (fig. 6). This permitted the reproducibility of any desired maximum stress to within 1 percent.

Each testing machine was equipped with a microswitch, which was automatically operated to open the motor circuit and thus stop the machine when a test specimen ruptured completely. A counter attached to the machine recorded the number of flexural stress cycles to which a specimen was subjected during test. In the case of some of the plate specimens, particularly those bonded by soldering, the electrolytic shell and the bond frequently failed first, whereas the back remained intact. Under this condition the stress in the iron back was decreased below its fatigue limit, and

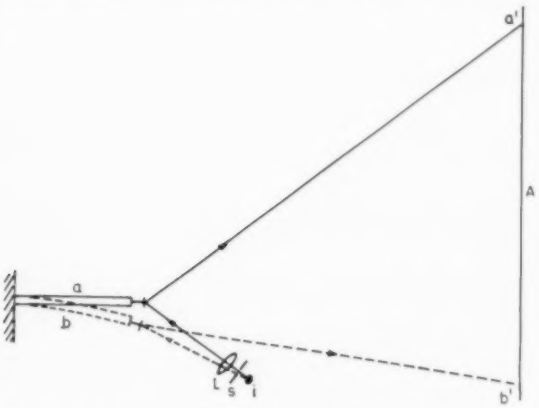

FIGURE 6. *Diagrammatic sketch showing the manner of measuring the deflection of the flexural fatigue specimen when loaded.*

The light beam from (I) passing through slit (S) and lens (L) is reflected by mirror to (a') on scale (A) when specimen is at zero stress position (a) and to (b') when at maximum stress position (b). The freely suspended end of the specimen is then attached to the crank-arm (fig. 5) and deflections corresponding to zero stress (a') and maximum stress (b') are obtained by adjusting the eccentric arm (fig. 5).

[6] Fatigue tests, H. F. Moore, ASM Handbook, 119 (1948).

the machine would run until stopped manually. Therefore, unless an operator was in constant attendance, a record of the number of cycles for failure of the shell was not obtained. In order to provide for this contingency, a special circuit comprising a relay in series with a number 38 B and S gage silk covered enamel copper wire secured with Duco cement to the upper surface of the specimen (fig. 7) was installed to interrupt the test when rupture of the shell occurred before complete failure of the back.

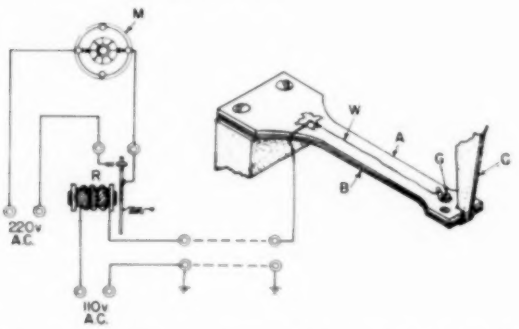

FIGURE 7. *Schematic diagram of the relay system used to discontinue the flexural fatigue test when the electroformed nickel-iron layer A (white section) failed while the fabricated iron backing B (cross-hatched) remained intact.*

When the electroformed layer A fractured, the copper wire W (grounded from G through the machine) ruptured, opening the relay R and stopping the machine.

In the present study the fatigue test was employed primarily as a means of obtaining an approximate relative measure of damage by flexing associated with the plating, thermal and bonding treatments employed. Because of this and the limited number of specimens available for test, the values selected for the fatigue limit were based on a stress, 500 to 1,000 lb/in.^{2} below the lowest stress resulting in failure, provided at least two runs of not less than 10 million cycles had been made at this stress.

IV. Results and Discussion

The S–N (stress-cycle) curves for each of the electro-formed materials tested are shown in figures 8 to 12, inclusive. The fatigue limits indicated in these figures are listed in table 1. It is apparent from a comparison of the curves in figures 8 and 9 that the fatigue properties of an iron-nickel composite sheet were affected adversely by the application of a thin (0.0003 in.) electro-

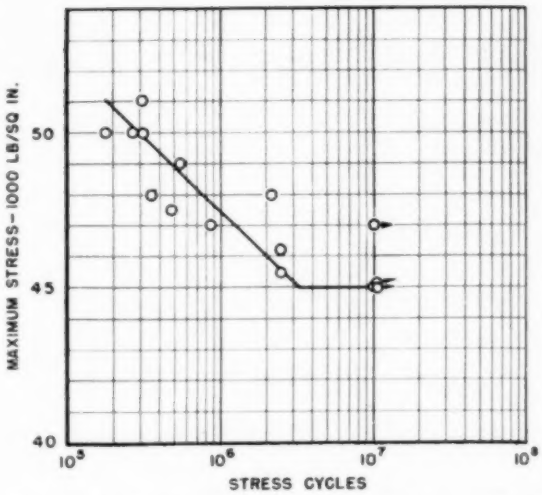

FIGURE 8. *Stress-cycle (S–N) graph based on results of flexural fatigue tests made on specimens of sheet No. 1 (table 1).*

deposited coating of chromium (fig. 1, b). However, this influence of the chromium layer was somewhat beneficially modified by thermal treatment (heated at 260° C (500° F) for 5 min), (figs. 9 and 10). Maximum improvement appeared to be obtained when the chromium plated iron-nickel sheet was heated (260° C for 5 min) after machining. In the cases of the solder-coated

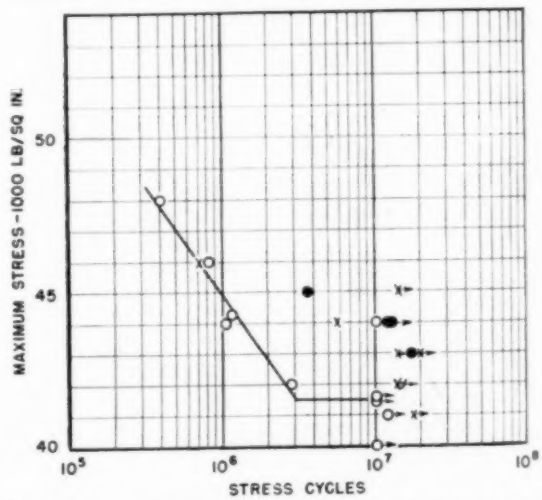

FIGURE 9. *Stress-cycle (S–N) graph based on results of flexural fatigue tests made on specimens of sheets No. 2, 2A, and 2B (table 1).*

○, as electroplated (sheet 2); X, tinned 5 min at 500° F after machining (sheet 2A); ●, heated 5 min at 500° F after machining (sheet 2B).

specimens, any deleterious effects that may have been imparted by the iron-tin compound formed at the iron-solder interface, apparently were overshadowed by the improvement resulting from the thermal effects (figs. 9 and 10).

The results of the tests on the specimens machined from the electroformed sheet 4 of iron-nickel-chromium after solder coating (fig. 1, d) at 260° C (500° F) (at temperature 5 min) showed considerably lower fatigue properties (fig. 11) than any of the electroformed sheets tested. It is noteworthy that the fatigue properties were significantly higher for the specimens cut from sheets 2B and 3A (table 1, also fig. 1, b, and c) having a 0.0003-in. thickness of chromium plate than for those prepared from sheet 4 (table 1 and fig. 1, d) plated with a 0.0006-in. thickness of chromium. Recent work done at the National Bureau of Standards [7] showed in certain cases that a plate thickness of 0.001 in. of chromium reduced the endurance properties of steel more than an appreciably thinner electrodeposit of this metal. This suggests that the lower fatigue limits (table 1) obtained on specimens of sheet 4 as compared with those machined from sheet 3 were attributable, at least in part, to the thicker deposit of chromium on sheet 4.

[7] The effect of chromium plating on the endurance limit of steels used in aircraft, H. L. Logan, J. Research NBS **43**, 101 (1949) RP2011.

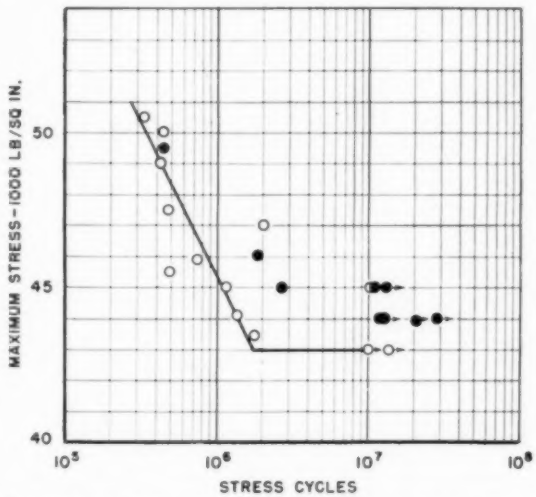

FIGURE 10.—*Stress-cycle (S–N) graph based on results of flexural fatigue tests made on specimens of sheets No. 3 and 3A (table 1).*

○, Heated for 5 min at 500° F before machining (sheet 3); ●, heated for 5 m.in at 500° F, machined and then tinned for 5 m.in at 500° F. (sheet 3A).

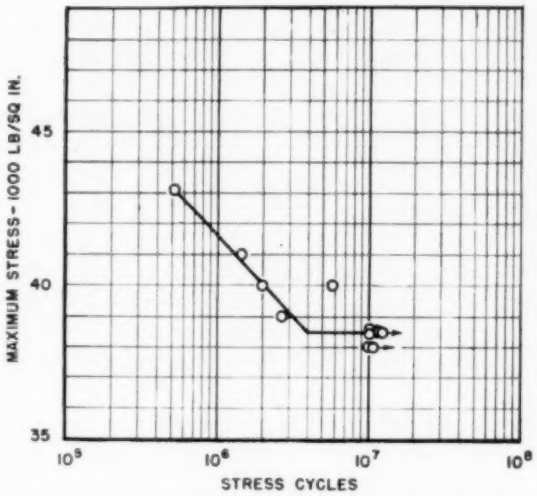

FIGURE 11. *Stress-cycle (S–N) graph based on the results of flexural fatigue tests made on specimens of sheet No. 4 (table 1).*

The fatigue limit of sheet 5 (fig. 1, e) formed by continuous electrodepositing (no detreeing) was somewhat lower than for material electroformed similarly (sheet 2, table 1, fig. 1, b) except for intermittent removal from the plating bath for detreeing. However, the adverse effect on the fatigue limit by thicker deposits of chromium previously discussed is considered to have been a greater influencing factor than the omission of the detreeing treatment.

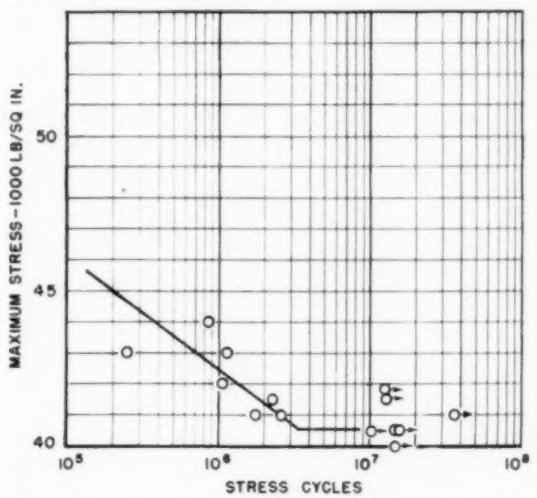

FIGURE 12. *Stress-cycle (S–N) graph based on the results of flexural fatigue tests made on specimens of sheet No. 5 (table 1).*

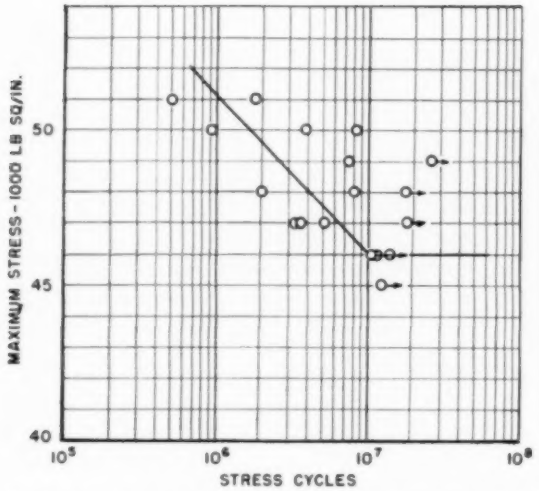

FIGURE 13. *Stress-cycle (S–N) graph based on the results of flexural fatigue tests made on specimens of printing plate composed of an electroformed shell of a layer each of iron and nickel (fig. 2) bonded to a backing of open hearth iron with two brushed coats of plastic adhesive.*

The results of the tests on specimens prepared from plates composed of electroformed sheets of iron-nickel bonded to open hearth iron backs are shown in figures 13 to 15, inclusive. It will be noted that the solder-bonded plate (fig. 15) had an appreciably lower fatigue limit than either of the composites bonded with the plastic adhesive (figs. 13 and 14). Furthermore, the specimens that were bonded with two brushed coats of the adhesive showed superior fatigue properties to those joined after applying first a brushed coat and then one by spraying. In nearly every case the failure of the soldered specimens was accompanied by a failure of the bond (fig. 16, a). The plastic bonded specimens rarely showed any indication of this type of failure, complete rupture occurring without separation of the component electroformed and fabricated iron layers as shown in figure 16, b.

A factor that in the greatest measure may be responsible for the adherence of the layers bonded with the plastic and the separation of those soldered is the degree of continuity of the bond. Thus, in every case examined the plastic bond was continuous (fig. 17, b) and in the case of separated soldered joints, there was evidence of discontinuities or porosity (fig. 17, a) in the bond layer. Another factor that may contribute to this result is the fact that the modulus of elasticity of the iron-tin compound at the interface of the solder and iron is higher than that of the plastic adhesive.

During the flexing action of the specimens, there was an appreciable stress applied to the bond layer. If the bond layer is of a porous nature, such as illustrated in figure 17, a, then its fatigue

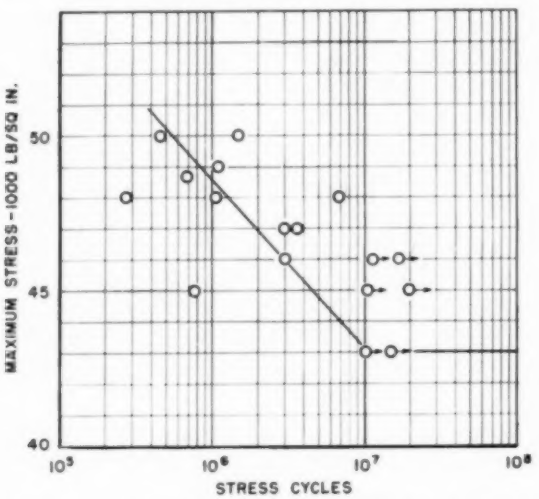

FIGURE 14. *Stress-cycle (S–N) graph based on the results of flexural fatigue tests made on specimens of printing plate composed of an eelctroformed shell of a layer each of iron and nickel (fig. 2) bonded to a backing of open hearth iron with first a brushed coat and then a sprayed coat of plastic adhesive.*

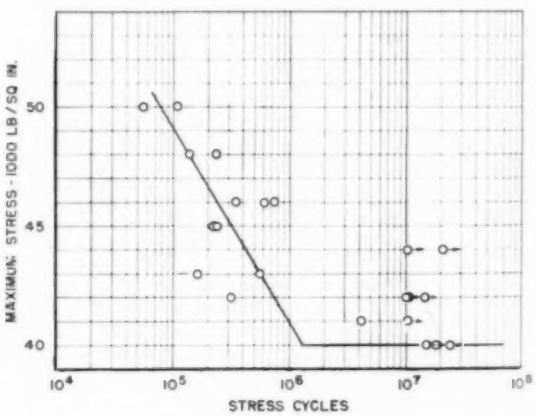

FIGURE 15. *Stress-cycle (S–N) graph based on the results of flexural fatigue tests made on specimens of printing plate composed of an electroformed shell of a layer each of iron and nickel (fig. 2) bonded to a backing of open hearth iron with 50–50 tin-lead solder.*

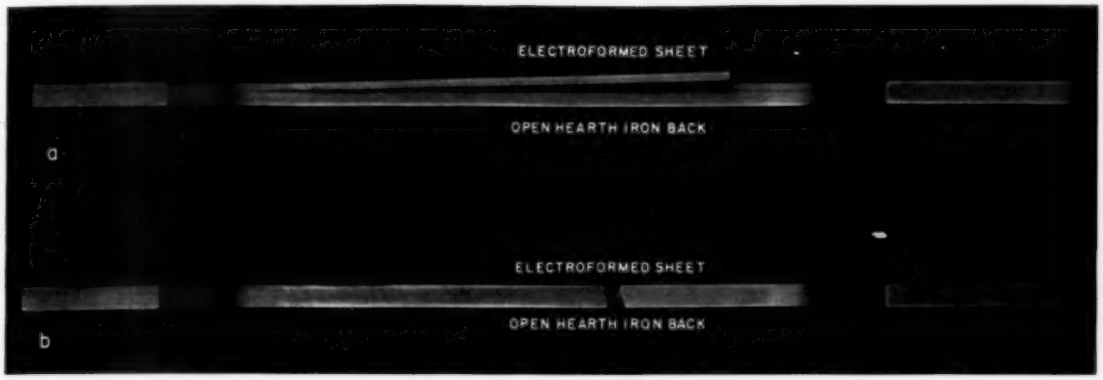

FIGURE 16. *Side view of flexural fatigue plate specimens showing the general manner in which failure occurred in the solder and plastic bonded plates respectively.*

a, Solder bonded specimen showing separation of the electroformed shell (upper portion) from the open hearth iron base; b, Plastic bonded specimen showing adherence of the electroformed shell to the iron base after complete fracture of the specimen.

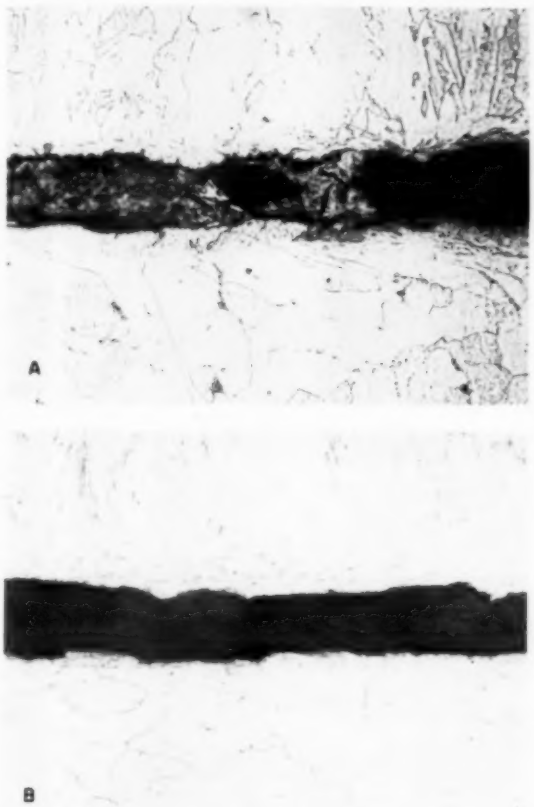

FIGURE 17. *Characteristic appearance of the bond layer between electroformed shell and open hearth iron back comprising the printing plate tested.*

Etched with 1 percent nital, x250; a, Solder (50-50 tin-lead) showing discontinuity and porosity (black areas); b, plastic adhesive.

strength might be sufficiently low to permit rupture during flexing with consequent separation of the two constituent layers. Despite this separation the layers remained firmly cemented together at their ends. This permitted a slight elongation and bowing of the electroformed layer (fig. 18), thus imposing a compressive stress on its bottom surface and tensile stress on its upper surface when the specimen was in the initially set zero stress position. As the specimen passed through a complete flexing cycle, the bottom face of the electroformed layer being above the center plane of the specimen parallel to its broad face (fig. 18) was subjected to a reversal of stress from compression to tension to compression. This suggests that since the maximum tensile stress imposed on the bottom face of the electroformed layer was approximately the same before and after the solder layer failed, the stress range for this bottom face increased after bond failure. This factor, coupled with stress raisers on the bottom face associated with the voids in the solder layer (fig. 17, a) and the corrosion effects of the excess soldering flux residing in the voids, may have caused fatigue failure of the electroformed layer.

Although the bonded printing plates commonly are chromium-plated on the nickel face, none of the bonded plates tested were thus plated. The results obtained on the electrolytic shells (figs. 8 to 12, inclusive) clearly indicate that the endurance properties of chromium-plated bonded plates would be somewhat lower than those shown for the bonded specimens tested (figs. 13, 14, and 15). However, on the basis of available service data, it

is not expected that the chromium plate would have altered the relative results as influenced by the type and method of bond employed.

V. Summary

A laboratory study was made to ascertain the flexural fatigue properties of electroformed iron-nickel and iron-nickel-chromium composite sheets and of plates composed of electroformed iron-nickel sheets bonded to open hearth iron. The electroformed sheets in every case consisted of one layer of each of the constituent metals. The bonding agents used in preparing the plates were 50–50 tin-lead solder, and a plastic adhesive applied in some cases as two brushed coats and in others as one brushed and one sprayed coat respectively to each of the two mating surfaces. On the basis of the results of this investigation, it is concluded that:

1. The fatigue limit of an iron-nickel composite is adversely affected by the application of a thin electrodeposited coating of chromium. Heating such tri-layer composites at 260° C (500° F) caused some increase of its fatigue limit. The most pronounced improvement resulted from heating at this temperature after machining.

2. The fatigue limits of the plates bonded with the plastic adhesive were significantly higher than those of the plates joined by soldering.

3. The application by brushing of the two coats of plastic adhesive to the mating surfaces of the composite layers of the plate resulted in a higher fatigue limit than the one brush and one spray coat procedure.

4. In nearly all cases, the solder bond failed either just prior to or simultaneously with the failure of the electroformed layer; the fabricated iron back remained intact under these circumstances. The number of plastic bond failures was negligible; in nearly all cases the iron layer remained secured to the electroformed layer and they failed as a unit.

5. The lower fatigue strength of the solder bonded specimens was attributed to the brittle iron-tin layer at the interface of the solder and iron, porosity or discontinuity of the solder layer, and corrosion caused by residual flux residing in the voids of the solder.

6. The results of this study are consistent with the service data of printing plates compiled at the Bureau of Engraving and Printing over a period of years in that the average life of the plastic bonded plates is considerably greater than the average life of plates whose component layers were joined by soldering.

FIGURE 18. *Schematic diagram indicating the bowing effect probably produced in the electroformed shell due to elongation of the shell during flexing after failure of the bond but before rupture of either the electroformed shell or the iron back.*

WASHINGTON, May 27, 1949.

U. S. Department of Commerce
National Bureau of Standards

Research Paper RP2040
Volume 43, November 1949

Part of the Journal of Research of the National Bureau of Standards

Interfacial Instability and Mixing in Stratified Flows

By Garbis H. Keulegan

When a liquid flows over a body of heavier liquid, with which it is miscible, an interface may be formed at which there is a sharp discontinuity of densities but not necessarily of velocities. As the relative velocity is increased, waves are formed at the interface, and at a critical velocity, mixing begins by the formation of eddies periodically ejected from the crests of the waves. The numerical values of a criterion for mixing, whose form was derived from theoretical considerations, were determined experimentally. Experimental data were also obtained on the relation of the amount of mixing to the relative velocity of the liquids at velocities higher than the critical.

I. Introduction

The intrusion of salt water in rivers that communicate with the seas and the silting of reservoirs receiving muddy waters are the two most important examples of stratified flow where the question of interfacial behavior assumes a basic significance. Depending on the conditions of approach, two possible forms of the interface may be noted. In one form, the interface may be identified as the dividing surface of two layers of liquid with different densities, the surface being one of sharp discontinuity of densities but not necessarily of velocities. Ordinarily the interface of this type is the locale of internal waves if the difference in velocities at points on opposite sides of the interface and at some distance from it is large. If mixing is present, it is in the form of eddies that are periodically ejected from the crests of the waves into the current that has the greater velocity. In the other form, the interface is a layer of transition between two currents. Both the densities and the velocities change uniformly in the layer that has measurable thickness. If any mixing is present, it is associated with the momentum exchange of turbulence, and the regular pattern of internal waves is absent. Thus a study of interfaces may be confined to one or the other of these forms.

In the present investigation, which is restricted to an interface with sharp discontinuity of densities, one may visualize the following distinct problems. First, what quantities are to be considered in determining a criterion for the incidence of mixing? Second, with current velocities exceeding the critical velocity of the criterion, how is the amount of mixing related to the velocity? Third, what is the exact mechanism of flow that produces the mixing?

About a decade or so ago at the National Hydraulic Laboratory, experiments were carried out to study each of these three questions. After having studied the first and the second of them with some degree of satisfaction with the results obtained, we were about ready to enter into the study of the third, which obviously is beset with considerable experimental difficulties and theoretical uncertainties. Unfortunately at that time it became necessary to suspend the hydraulic work in the laboratory, and since then we have had no opportunity to return to our original plans. Meanwhile considerable interest in these matters has developed. Since numerous inquiries have been received about the progress already made, it was decided to make these results known notwithstanding their incompleteness.

II. Determination of the Critical Velocity of Mixing

Observations on the instability of interfaces were made for the condition where the upper, less dense liquid was flowing over a heavier liquid at rest in a pool. The essentials of the apparatus

and the arrangements are shown in figure 1. The apparatus consisted of a closed flume with vertical glass walls and was limited at the entrance by a constant level tank and at the exit by a discharge tank. The large reservoir of the circulating liquid, which was the lighter liquid, was connected to the constant level tank through a pump. To prevent the transmission of pump vibrations to the flume frame, the connection to the constant level tank was made through a flexible rubber tubing. The return flow passed from the discharge tank into a metering tank of the orifice type, which in turn discharged its contents continually into the reservoir of light liquid below. The volume of the circulating liquid during a test remained the same, and since the reservoir volume was many times larger than the volume of the flume, mixing in the flume during a run had very little effect on the density of the upper liquid. The loss of the heavier liquid from the pool during tests was made up at intervals by drawing from a reservoir placed at a higher elevation.

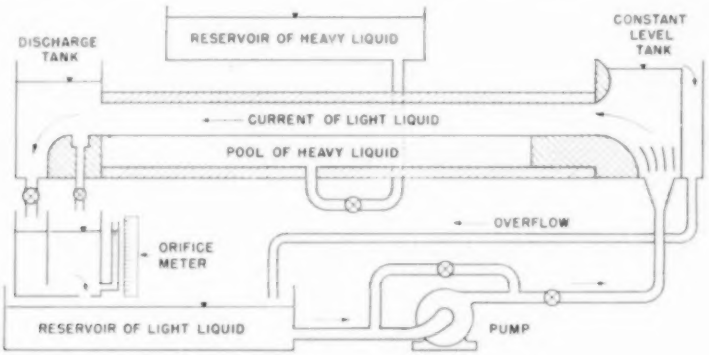

FIGURE 1. *Diagram of flume and accessories.*

For the purpose of examining the effect of Reynolds number, three flumes of various sizes were employed. They were rectangular in cross section, with the greater dimension vertical, with cross sectional dimensions of 2 by 4 cm, 4 by 8 cm, and 11.3 by 28.5 cm. The length in each case was about 25 times the total depth. The flumes were operated full, keeping the depths of the two layers equal or nearly equal. Accordingly, the hydraulic radii associated with the currents were 0.50, 1.00, and 3.27 cm. The flumes will be referred to as the small, the medium, and the large flume.

The flowing current caused the lower liquid to be dragged out in the downstream direction. In the small and the medium flumes, the escape of the lower liquid was prevented by tilting the flumes by means of screw-jack supports. This method was not practicable for the large flume. Instead, the flume was fixed in a moderately inclined position. When the velocities of the current were too high, the lower liquid that was dragged out was prevented from entering the lower reservoir by drawing it off through a trap at the exit end. The idea involved in the method is shown in figure 2.

The determination of the critical velocity; that is, the velocity at which the mixing of the liquid of the lower layer with the upper commenced, or was about to commence, was done visually by noting the condition of the interface. At low velocities a smooth interface was discernible even when the lower liquid was not colored. At this

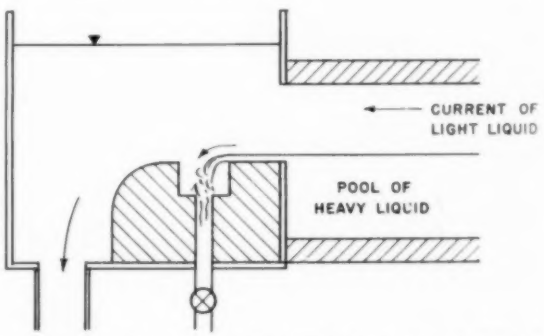

FIGURE 2. *Diagram of diverter for heavy liquid dragged out of flume by the current of light liquid.*

initial stage, observations showed that at the interface, and in a finite band on the two sides of the interface, the flow was laminar even when the central regions of the upper current were eddying or turbulent. When the velocity of the current was increased to some definite value depending on the densities and the viscosities of the two liquids, the interface appeared to be covered with ridges extending from one glass wall to the other. These ridges moved progressively downstream, and their crest lines were parabolic in shape, the crest heights being greatest at the center. With a slight increase in the value of the current velocity, waves appeared in a new configuration. The interface now was covered with waves of shorter crest lines. In the tests with the large flume these crest lines were one-half or one-third of the channel width. The appearance of the waves and their sequence was regular. The movement was progressive. The predominant wavelength remained constant, or nearly so, throughout the channel length. With further increase of the velocity of the current, the waves became sharp-crested, and mixing commenced. At the beginning the mixing was slight, and it augmented with subsequent increases in velocity. It appeared that increased velocities did not substantially affect the wavelengths of the interfacial waves, although there was a tendency for the lengths to decrease slightly. The most marked influence of the increasing velocities was to augment the height of the sharp-crested waves, the size of the eddies emanating from the crests, and the frequency of departure of the eddies. Practically, the mechanism of mixing was an ejection of eddies from the crests into the moving current, as shown diagrammatically in figure 3.

Now, what constitutes the critical velocity of mixing is a matter difficult to decide. The method that we employed is as follows: In the record book was entered a description of the appearance of the interface, together with a qualitative statement regarding the degree of mixing for a measured velocity of the current. The interface, for example, was described as being smooth, or having parabolic waves, or mixed waves, or sharp crests, or agitated crests. The mixing was described as absent, or slight, or moderate, or excessive. We note the velocity U_0, the maximum velocity recorded in the book as corresponding to a smooth interface and to no mixing. Next we take the velocity U_1, which is the average of all the velocities associated with slight mixing. The mean value of U_0 and U_1 is chosen to represent the critical velocity of mixing. It is denoted by U_c. The average value of the velocities associated with moderate mixing are denoted by U_2, and the average value above which there was always excessive mixing as U_3.

The test liquids were tap water and sugar solutions. Four series of tests were made. In three of the series the upper liquid consisted of tap water, and tests were made in all three flumes. The purpose of these tests was to determine the effect of the Reynolds number of the upper current on the incidence of mixing. The fourth series of tests was intended to determine the effect of viscosity on mixing. These tests were made with the medium flume. Both the upper liquid and the lower liquid were sugar solutions. The fractional difference of the densities was kept practically constant, but the viscosity of the upper liquid was varied. The velocity data from the tests of the four series are given in tables 1, 2, 3, and 4.

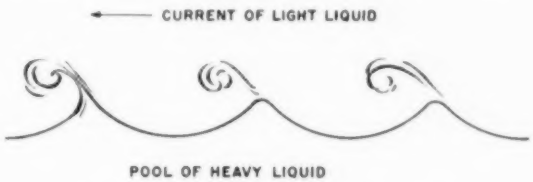

FIGURE 3. *Diagram of process of mixing.*

TABLE 1. *Mixing tests in the small flume*

(Hydraulic radius=0.50 cm)

Run	ρ_1	ρ_2	ν_1	ν_2	U_0	U_0	U_1	U_2	U_3
	g/cm³	g/cm³	cm²/sec	cm²/sec	cm/sec	cm/sec	cm/sec	cm/sec	cm/sec
C-13	1.000	1.097	0.0086	0.0174	7.45	6.97	7.94	9.96	13.01
C-14	1.000	1.185	.0086	.0455	9.14	8.12	10.16	12.85	15.28
C-15	1.000	1.173	.0085	.0395	10.18	8.47	11.89	14.65	23.65
C-16	1.000	1.139	.0084	.0283	7.99	7.00	8.98	12.61	16.53
C-17	1.000	1.095	.0080	.0151	7.12	6.34	7.91	10.15	14.65
C-18	1.000	1.064	.0080	.0120	6.98	5.91	8.06	10.35	14.24
C-19	1.000	1.061	.0079	.0119	6.19	5.58	6.81	9.16	12.76
C-20	1.000	1.036	.0082	.0101	6.25	5.65	6.85	8.02	9.63
C-21	1.000	1.017	.0081	.0088	5.21	4.61	5.82	6.96	8.37
C-22	1.000	1.007	.0082	.0083	4.08	3.92	4.27	5.01	5.41
C-23	1.000	1.226	.0081	.0800	8.14	7.96	9.52	14.71	20.45

TABLE 2. *Mixing tests in the medium flum*

(Hydraulic radius=1.00 cm)

Run	ρ_1	ρ_2	ν_1	ν_2	U_*	U_0	U_1	U_2	U_3
	g/cm³	g/cm²	cm²/sec	cm²/sec	cm/sec	cm/sec	cm/sec	cm/sec	cm/sec
D-1	1.000	1.038	0.0088	0.0131	4.39	3.85	4.93	5.37	6.63
D-2	1.000	1.044	.0095	.0129	4.59	3.96	5.23	5.50	5.81
D-3	1.005	1.052	.0095	.0140	4.55	4.47	4.62	5.02	5.41
D-4	1.026	1.062	.0106	.0137	4.75	4.47	4.62	5.02	5.41
D-5	1.037	1.085	.0118	.0175	5.52	5.05	5.99	6.67	7.62
D-6	1.049	1.094	.0137	.0204	6.49	6.07	6.91	7.45	8.60
D-7	1.064	1.103	.0163	.0235	6.88	6.86	6.91	7.27	7.71
D-8	1.074	1.119	.0178	.0277	7.18	6.68	7.68	8.03	8.23
D-9	1.088	1.122	.0192	.0268	7.04	6.53	7.56	8.04	8.80
D-10	1.100	1.139	.0203	.0301	6.97	6.77	7.18	7.60	8.75
D-11	1.128	1.164	.0233	.0351	7.68	7.65	7.72	8.20	8.00
D-12	1.146	1.183	.0276	.0449	8.56	7.96	9.17	9.26	9.31
D-13	1.161	1.203	.0336	.0501	9.98	9.31	10.66	11.28	12.19
D-14	1.171	1.204	.0303	.0642	10.46	9.78	11.15	11.93	12.60
D-15	1.205	1.245	.0799	.1563	13.29	12.17	14.41	14.98	15.46
D-16	1.225	1.257	.1020	.1970	13.17	11.74	14.61	15.80	16.74

TABLE 3. *Mixing tests in the medium flume*

(Hydraulic radius=1.00 cm)

Run	ρ_1	ρ_2	ν_1	ν_2	U_*	U_0	U_1	U_2	U_3
	g/cm³	g/cm³	cm²/sec	cm²/sec	cm/sec	cm/sec	cm/sec	cm/sec	cm/sec
D-18	1.000	1.206	0.0085	0.1890	10.12	9.12	11.13	.....	.....
D-19	1.000	1.139	.0092	.0318	7.86	6.44	9.28	11.10	.....
D-20	1.000	1.135	.0090	.0264	8.31	6.02	10.60	13.50	15.57
D-21	1.000	1.133	.0094	.0272	8.54	6.82	10.47	12.14	13.25
D-22	1.000	1.158	.0094	.0370	8.56	6.57	10.56	12.43	14.96
D-23	1.000	1.104	.0094	.0204	7.30	5.98	8.62	10.83	12.06
D-24	1.000	1.094	.0092	.0180	6.55	5.68	7.42	9.92	12.03
D-25	1.000	1.102	.0092	.0139	6.87	5.74	8.00	9.89	11.38
D-26	1.000	1.069	.0090	.0143	6.28	5.54	7.03	8.96	10.51

TABLE 4. *Mixing tests in the large flume*

(Hydraulic radius=3.27 cm)

Run	ρ_1	ρ_2	ν_1	ν_2	U_*	U_0	U_1	U_2	U_3
	g/cm³	g/cm³	cm²/sec	cm²/sec	cm/sec	cm/sec	cm/sec	cm/sec	cm/sec
E-8	1.000	1.0189	0.0090	0.0126	5.32	4.83	5.92	7.32	8.33
E-9	1.000	1.046	.0094	.0131	5.57	4.76	6.39	8.11	9.20
E-11	1.000	1.016	.0093	.0101	3.84	3.08	4.65	6.16	6.76
E-12	1.000	1.150	.0110	.0104	8.27	7.02	9.52	12.50	13.45
E-13	1.000	1.134	.0103	.0328	7.95	6.58	9.32	11.64	13.15
E-14	1.000	1.116	.0099	.0251	7.13	5.31	8.95	10.49	12.41
E-15	1.000	1.110	.0098	.0213	7.09	5.79	8.39	10.90	12.45
E-17	1.000	1.060	.0106	.0160	5.50	5.00	6.00	6.92	7.98
E-18	1.000	1.031	.0100	.0122	4.93	4.46	5.20	6.86	7.31
E-19	1.000	1.033	.0101	.0125	4.37	3.46	5.28	6.17	7.03
E-20	1.000	1.030	.0101	.0122	4.36	3.92	4.80	6.29	6.96
E-21	1.000	1.022	.0098	.0112	4.36	3.56	5.17	6.38	7.55

III. A Theoretical Basis for the Dimensionless Parameter of the Critical Velocity

If it were not for the inertia and the restraining effect of the upper current on the motion of the interfacial internal waves, we would introduce directly the criterion for wind-generated waves derived by Jeffreys as the desired criterion [1, 2].[1] Jeffreys has shown that at the moment of developing wind waves

$$U^3=\frac{27}{S}\nu_2 g\frac{\Delta\rho}{\rho_1}, \tag{1}$$

where U is the velocity of wind over water that is still initially, ν_2 is the kinematic viscosity of water, $\Delta\rho$ is the difference between the densities of water and air, ρ_1 is the density of air, S is a numerical constant, and g is the acceleration of gravity.

Jeffrey's method for the analysis of the wind velocity criterion shows a marked departure from the well-known derivation due to Kelvin. The hypothesis that the flow in air is irrotational is abandoned, and instead it is supposed that the motion of air is such as to introduce a pressure variation over the water surface of the magnitude

$$p=S\rho_1 U^2 dh/dx, \tag{2}$$

where S is a numerical constant referred to as the sheltering coefficient, U is the velocity of the air over the crest, h is the surface elevation of the wave above the undisturbed surface, and x is in the direction of wind motion.

Jeffreys has concluded from observations on the initial formation of wind waves in a river and in the waters of a large pond that the velocity of a wind just strong enough to raise waves is 110 cm/sec, the average of three observations. The corresponding value of S is 0.274. Substituting these values in eq 1, we get for the criterion, writing

$$\mathrm{O}=\left(\nu_2 g\frac{\Delta\rho}{\rho_1}\right)^{\frac{1}{3}}/U, \tag{3}$$

the value

$$\mathrm{O}=0.215. \tag{4}$$

The problem of interfacial waves between two moving layers is a question of small oscillations

[1] Figures in brackets indicate the literature references at the end of this paper.

about a steady state of motion. Let the velocity of the upper layer be U, and of the lower layer zero. Let the corresponding densities be ρ_1 and $\rho_2(=\Delta\rho+\rho_1)$. The wavelength and the period being λ and T, the internal waves may be assumed to be given by

$$h=a\cos(kx-\sigma t), \tag{5}$$

where $k=2\pi/\lambda$ and $\sigma=2\pi/T$. Supposing that the motions are irrotational everywhere, that the wavelengths are small in comparison with the depths of the layers, and that the wave height is small with respect to the wavelength, analysis gives for the velocity ω of the waves

$$\omega=\frac{\sigma}{k}=\frac{U}{2}+\left[\frac{1}{2}\frac{g}{k}\frac{\Delta\rho}{\rho_1}-\frac{1}{4}U^2\right]^{\frac{1}{2}}, \tag{6}$$

provided that the square of $\Delta\rho/\rho_1$ is negligible with respect to unity [3]. In stable waves σ is real, and thus

$$U^2\leq\frac{2g}{k}\frac{\Delta\rho}{\rho_1}. \tag{7}$$

As was noted previously, the internal interfacial waves just prior to the setting-in of mixing are regular in form and move progressively downstream without changing their form. The regularity and the permanency of form indicate that there is a mechanism by which the upper current is furnishing energy to the wave motion of the lower liquid just sufficient to counter the dissipation due to viscous effects. There are three conceivable methods of furnishing the energy. The energy supply may be effected through the normal stresses p_{zz}, or the tangential stresses p_{xz}, or by the combination of these stresses. Since for the ultimate purpose of the analysis, which is the derivation of dimensionless parameters, the selection is not important, it will be supposed that the transfer is made by the normal stresses p_{zz}, and the tangential stresses p_{xz} vanish.

The dependence of p_{zz} on the wave form must be known. The dissipation of waves through viscous forces has a direct bearing on the relation, and it is necessary that the ordinary equations of motion involving the viscosity terms be considered. These equations, neglecting the second-order terms, are

$$\frac{\partial u}{\partial t}=-\frac{1}{\rho}\frac{\partial p}{\partial x}+\nu\nabla^2 u,\ \nabla^2=\frac{\partial^2}{\partial x^2}+\frac{\partial^2}{\partial z^2}, \tag{8}$$

$$\frac{\partial w}{\partial t}=-\frac{1}{\rho}\frac{\partial p}{\partial z}-g+\nu\nabla^2 w, \tag{9}$$

and

$$\frac{\partial u}{\partial x}+\frac{\partial w}{\partial z}=0. \tag{10}$$

It is implied that z is drawn vertically upwards. It will also be supposed that the origin is in the undisturbed level of the interface, and that x is taken in the direction of wave motion. The quantities u and w denote the particle velocity components along the axes x and z, respectively.

It has been shown by Basset [3], that the above set of equations is satisfied by

$$u=-\frac{\partial\phi}{\partial x}-\frac{\partial\psi}{\partial z},\qquad w=-\frac{\partial\phi}{\partial z}+\frac{\partial\psi}{\partial x}, \tag{11}$$

and

$$p/\rho=\frac{\partial\phi}{\partial t}-gz, \tag{12}$$

provided that

$$\nabla^2\phi=0,\qquad \frac{\partial\psi}{\partial t}=\nu\Delta^2\psi. \tag{13}$$

Basset [3] and later Lamb [4] have applied these to the determination of the damping of the surface waves of a homogeneous layer. In reworking the solutions, we wish to find the condition that corresponds to no damping. It is to be noted that only in the event that ψ becomes negligible may the flow be regarded as irrotational.

It seems that the above equations and the solution derived from them can be applied directly to the case of internal waves after resorting to the following artifice. The presence of the upper current is imagined to be evidenced in two ways only. First, the dynamical action of the current consists of the normal stresses p_{zz}. Second, the intensity of gravity in the lower liquid is reduced from g to g', so that

$$g'=k\omega^2. \tag{14}$$

Accordingly, in the place of eq 12 we will write

$$p/\rho_2=\frac{\partial\phi}{\partial t}-g'z. \tag{15}$$

For the case of infinite depth and liquid at rest corresponding to the wave profile,

$$h=a\cos(kx-\sigma t), \tag{5}$$

correspond the solutions of eq 11:

$$\phi=Ae^{kz}e^{i(kx+\sigma t}, \tag{16}$$

and

$$\psi=Ce^{mz}e^{i(kx+\sigma t}, \tag{17}$$

with

$$m^2=k^2+\alpha/\nu. \tag{18}$$

If the case of cellular waves be excluded, m denotes that root which has its real part positive. Thus,

$$u=-(ikAe^{kz}+mCe^{mz})e^{i(kx+\sigma t}, \tag{19}$$

and

$$w=-(kAe^{kz}-ikCe^{mz})e^{i(kx+\sigma t}, \tag{20}$$

In this solution we are supposing that there is no bodily movement of the lower layer as a whole, so that the surface kinematical condition is

$$\partial h/\partial t=w, \qquad z=0, \tag{21}$$

and this leads to

$$h=-\frac{k}{\alpha}(A-iC)e^{i(kx+\sigma t}. \tag{22}$$

By Stokes' rule, the relations between the stresses and the dilatations are

$$p_{zz}=-p+2\mu\frac{\partial w}{\partial x}, \tag{23}$$

and

$$p_{xz}=\mu\left(\frac{\partial w}{\partial x}+\frac{\partial u}{\partial z}\right). \tag{24}$$

As regards the normal stresses, it is appropriate to suppose, since a regular progression of waves is imagined, that

$$p_{zz}=-\beta Ae^{i(kx+\sigma t}. \tag{25}$$

It being the convention to regard pressures as negative tensions, β is a positive quantity. The dynamical surface conditions, from eq 15, 19, 20, 22, 23, 24, and 25 are

$$(\alpha^2+2\nu k^2\alpha+g'k-\beta\alpha)A+i(g'k+2\nu km\alpha)C=0, \tag{26}$$

and

$$2i\nu k^2A+(\alpha+2\nu k^2)C=0. \tag{27}$$

The elimination of the quantities A and C leads to

$$\alpha^2+4\nu k^2\alpha+g'k-\alpha\beta-2\nu k^2\beta+4\nu^2k^4-4\nu^2k^3m=0. \tag{28}$$

where ν is small, the terms containing its square may be neglected, and

$$\alpha^2+4\nu k^2\alpha+g'k-\alpha\beta-2\nu k^2\beta=0. \tag{29}$$

This may be written

$$\alpha^2+4(\nu k^2-\beta/4)\alpha=-g'k+2\nu k^2\beta. \tag{30}$$

The condition that the waves are neither damped nor growing in height requires that

$$\nu k^2-\beta/4=0;$$

or,

$$\beta=4\nu k^2. \tag{31}$$

Thus, eq 30 reduces to

$$\alpha^2=-g'k+2\nu k^2\beta,$$

or

$$\alpha^2=-g'k+8\nu^2k^4,$$

and due to the approximations assumed

$$\alpha^2=-g'k, \tag{32}$$

or

$$\alpha=-\sigma i,$$

and substituting the latter in eq 22, since $\sigma/k=\omega$

$$h=\frac{1}{i\omega}(A-iC)e^{i(kx-\omega t}.$$

Equation 27 shows that the ratio C/A is a small quantity when ν is small. Neglecting C,

$$h=\frac{A}{i\omega}e^{i(kx-\omega t}.$$

Putting

$$A/i\omega=a,$$

$$h=a\cos(kx-\sigma t). \tag{5}$$

To this corresponds the surface pressure variation

$$p_{zz}=4\rho_2\nu k^2\omega a\sin(kx-\sigma t), \tag{33}$$

and therefore the pressure is smaller on the forward face of a wave and greater on the backward face, as is to be expected.

Here, following Jeffreys, we introduce the supposition that

$$p_{zz}=S\rho_1(U-\omega)^2 dh/dx, \tag{34}$$

that is,

$$p_{zz}=S\rho_1(U-\omega)^2 ka \sin(k\chi-\sigma t). \tag{35}$$

The implication is that for the maintenance and for the growth of waves U is larger than ω; that is, the current velocity is larger than ω. When U is smaller than ω, the waves are damped. The latter statement is due to Kelvin [5].

Comparing eq 33 and 35 with each other and ignoring the small term involving $\Delta\rho/\rho_1$, and writing ν_2 for ν_1

$$\frac{(U-\omega)^2}{\omega}=\frac{4\nu_2 k}{S}. \tag{36}$$

This is the relation to be satisfied between the quantities ω, U, and k at the instant that the internal waves are about to increase in height. Returning to the inequality, eq 7, it may be supposed that the wavelengths have reached the greatest values consistent with stability; that is

$$k=\frac{2g}{U^2}\frac{\Delta\rho}{\rho_1}. \tag{37}$$

Eliminating k between the latter two equations,

$$U^2(U-\omega)^2/\omega=\frac{8}{S}\nu_2 g\Delta\rho/\rho_1, \tag{38}$$

and since under these conditions

$$\omega=U/2, \tag{39}$$

(see eq 6) we finally obtain

$$U^3=\frac{16}{S}\nu_2 g\Delta\rho/\rho_1. \tag{40}$$

This may be written as

$$\Theta=(\nu_2 g\Delta\rho/\rho_1)^{1/3}/U, \tag{41}$$

and is the desired form for the criterion of mixing.

IV. Experimental Value of the Criterion of Mixing

To generalize the result of the theoretical analysis made above and in particular to examine the effect of the Reynolds number of the current on mixing, the data of the tests will be considered in the parametric forms

$$\Theta=(\nu_2 g/\Delta\rho/\rho_1)^{1/3} \tag{42}$$

and

$$\Theta=\Theta(U_c R/\nu_1). \tag{43}$$

In these, ρ_1 is the density of the upper flowing liquid, ν_1 and ν_2 are the kinematic viscosities of the upper and the lower liquids, respectively, $\Delta\rho$ is the difference in the densities of the two liquids, U_c is the critical velocity of mixing, and R is the hydraulic radius of the cross section of the flowing current.

However, prior to the consideration of the magnitude of the criterion it will be helpful to present the evidence of the effect of kinematic viscosity on the criterion itself. The criterion contains the quantities ν_2 and $\Delta\rho/\rho_1$ each raised to its one-third power. The effect of the viscosity will be seen best and also most convincingly if a series of tests are conducted keeping $\Delta\rho/\rho_1$ constant or nearly constant and varying the kinematic viscosity ν_2 over a large range. Most of the runs of the D series in the medium flume fulfill this condition. The test data are given in table 2. The plotting shown in figure 4 is from this table. The critical

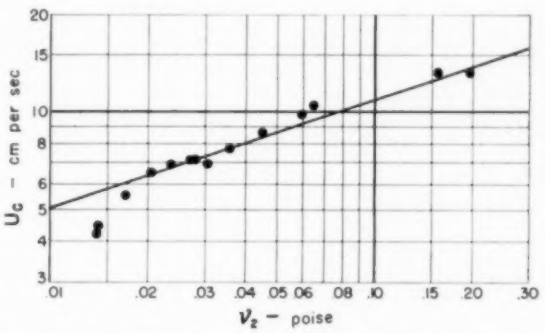

FIGURE 4. *Relation of critical velocity of mixing to kinematic viscosity of heavy liquid.*

velocity of mixing is treated as a function of the kinematic viscosity of the lower liquid. The great majority of the points aline themselves along a straight line having an inclination of one in three. Since the plotting is done logarithmically, this at least confirms the requirement of the theory.

As regards the criterion and the effect of Reynolds number on it, the values of the parameter

Θ from all the tests are shown in figure 5. One glance at the figure suggests that the criterion has one constant value below a Reynolds number of 450 and another constant value above it:

$$\Theta = 0.127,\ R_c < 450; \tag{44}$$

and

$$\Theta = 0.178,\ R_c > 450. \tag{45}$$

Significantly, $R_c = 450$ is also the Reynolds criterion that separates the regime of turbulent flow from the regime of laminar flow.

Considering the distribution of the Θ points more carefully for Reynolds numbers above 450, some systematic variations from the mean value, 0.178, are detectable. This would mean that there are other factors having a secondary influence on the value of the mixing criterion. Such factors

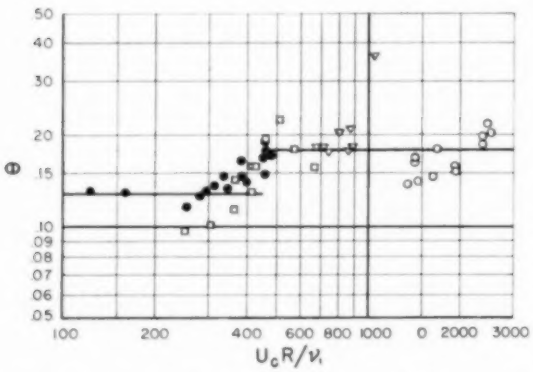

FIGURE 5. *Relation of criterion of mixing to the Reynolds number of the current of light liquid.*

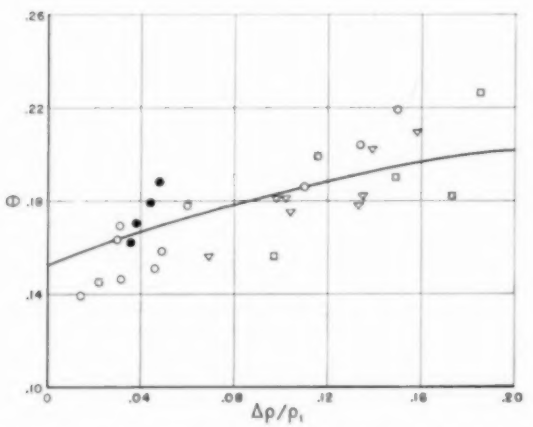

FIGURE 6. *Relation of criterion of mixing to the relative densities of the two liquids.*

may very well be (a) the surface tension between the two liquids, (b) the difference between the kinematic viscosities of the two liquids, and (c) the relative densities of the two liquids. It would be a futile effort to speculate on the effect of these factors separately. Since in these present tests the solutions were prepared from the same solvent and solute, one may say that all these factors or quantities are functions of $\Delta\rho/\rho_1$. Thus it would be appropriate and also sufficient to consider the dependence of Θ on $\Delta\rho/\rho_1$. For that purpose the graph in figure 6 has been prepared. That Θ values vary with $\Delta\rho/\rho_1$ appears to be unmistakable.

It is interesting to compare the value of the criterion for the mixing between two liquids obtained in these tests with the criterion that may be associated with the formation of wind waves. The latter, as determined from the observations of Jeffreys, has been mentioned previously. The value found by Jeffreys was 0.215, and this is not very different from the mean value of the mixing criterion of the tests; that is, the value 0.178. When the very great differences in the conditions of these two phenomena are considered, the closeness of the two values is quite surprising.

V. Mean Velocity Distribution in Currents

The fact, as shown earlier in this paper, that the criterion of mixing takes on two different values, one value when the Reynolds number of the current is below 450 and another value when above, may be explained on the grounds of velocity distributions. For the changes of the interface, the velocities near the interface are the important ones. The representation of the data, however, was based on the mean flow, and it will be illuminating to examine the variation of the mean velocity distributions in the cross section of a square channel for laminar and turbulent flows.

For this purpose we take a square of side $2l$, draw an inside square of side $2(l-s)$, with the centers coinciding, and consider the space between the two (fig. 7). This space is a frame of width s. Denoting the mean velocity in the complete large square by $\overline{u}$, and in the frame only by $\overline{u}_s$, we wish to find the variation of $\overline{u}_s/\overline{u}$ with s/l. If the flow is turbulent, using the Blasius law of velocity, and supposing that the wall shear is constant along the entire perimeter, it is a simple matter to show that

$$\frac{\overline{u}_s}{\overline{u}} = \frac{(s/l)^{\frac{1}{7}}(15-8s/l)}{7(2-s/l)}. \tag{46}$$

Values of this relation are shown in figure 7. Accordingly, when the flow is turbulent, the velocities near the interface are not much different from the mean velocity of the entire section. In the actual conditions of the tests, the differences are somewhat smaller than is indicated by the curve, since the liquid at the interface is in motion, and this was ignored in the derivation given above.

The computation of a similar result for the condition of laminar flow could have been made from

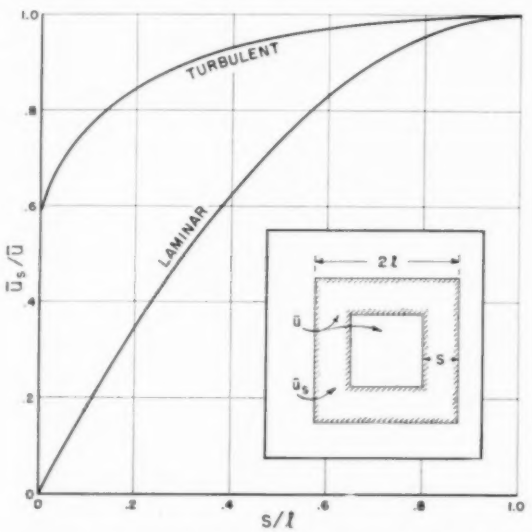

FIGURE 7. *Mean velocity distributions in a square channel for laminar and turbulent regimes.*

the formula of velocity distribution in a rectangular channel that Bateman gives [6]. However, computations from this particular formula are somewhat cumbersome, and it was decided to derive a simpler formula involving algebraic polynomials only.

Taking the axis of the channel as the z axis, pressures decreasing with z, the equation of motion is

$$\frac{\partial p}{\partial z} = \mu\left(\frac{\partial^2 u}{\partial x^2} + \frac{\partial^2 u}{\partial z^2}\right), \tag{47}$$

where p is the pressure, uniform across a normal section. Let $2l$ be the length of the square side. Let u_m be the maximum velocity in the section; that is, the velocity at $x=0$, $y=0$. Writing the variables

$$\left.\begin{aligned} \frac{u}{u_m} &= \chi, \\ \frac{x}{l} &= \zeta, \\ \frac{y}{l} &= \eta, \end{aligned}\right\} \tag{48}$$

and introducing the dimensionless form of the pressure term,

$$\frac{1}{\mu}\frac{l^2}{u_m}\frac{\partial p}{\partial z} = -\kappa, \tag{49}$$

the equation of motion now becomes

$$\nabla^2\chi = +\kappa, \tag{50}$$

where

$$\nabla^2 = \frac{\partial^2}{\partial\zeta^2} + \frac{\partial^2}{\partial\eta^2}.$$

The boundary conditions are

$$\left.\begin{aligned} \chi &= 0, \quad \zeta = 1, \quad -1 \le \eta \le 1, \\ \chi &= 0, \quad \eta = 1, \quad -1 \le \zeta \le 1, \\ \chi &= 0, \quad \zeta = 0, \quad \eta = 0. \end{aligned}\right\} \tag{51}$$

The velocity term may be expanded in terms of algebraic polynomials:

$$\chi = 1 + a\chi_2 + b\chi_4 + c\chi_8 + \ldots, \tag{52}$$

where $a\chi_2$ is a particular solution of eq 49, and the remaining polynomials χ_4, χ_8, . . . are the solution of

$$\nabla^2\chi = 0. \tag{53}$$

The quantities a, b, c are numerical constants.

Since the cross section is a symmetrical one, the polynomials χ_2, χ_4, χ_8 . . . are functions of ζ^2 and η^2. Also, in particular, the section is a square, and thus the value of the polynomials will not be altered when ζ is replaced by η and η is replaced by ζ. Subject to these conditions

$$\left.\begin{aligned} \chi_2 &= \zeta^2 + \eta^2, \\ \chi_4 &= \zeta^4 + \eta^4 - 6\zeta^2\eta^2, \\ \chi_8 &= \zeta^8 + \eta^8 - 28\zeta^6\eta^2 - 28\zeta^2\eta^6 + 70\zeta^4\eta^4 \ldots \end{aligned}\right\} \tag{54}$$

As $a\chi_2$ is solution of eq 50:

$$a = -\kappa/4. \tag{55}$$

This determines κ from the constant a. For the determination of the constants a, b, and c we write from eq 51

$$\left.\begin{aligned} \chi=0, \quad \eta=1, \quad \zeta=0, \\ \chi=0, \quad \eta=1, \quad \zeta=1, \\ \partial^2\chi/\partial\zeta^2=0, \quad \eta=1, \quad \zeta=0. \end{aligned}\right\} \tag{56}$$

Accordingly,

$$\left.\begin{aligned} a+b+c=-1, \\ 2a-4b+16c=-1, \\ a-6b-28c=0. \end{aligned}\right\} \tag{57}$$

Solving these simultaneously,

$$\left.\begin{aligned} a=-0.8456, \\ b=-0.1581, \\ c=-0.00368. \end{aligned}\right\} \tag{58}$$

The relation between the pressure fall and the maximum velocity now is

$$\frac{\partial p}{\partial z}=3.382\,\frac{\mu u_m}{l^2}, \tag{59}$$

and between the mean velocity and maximum velocity,

$$\overline{u}=0.4797u_m. \tag{60}$$

The values of $\overline{u}_s/u$ as determined in this analysis are shown likewiseiin figure 7 by the curve labeled "laminar." Accordingly, in laminar flows the velocities near the interface are appreciably lower than the mean velocity of the entire section, and this fact will lead to a smaller value of the mixing criterion if it is computed on the basis of mean flow.

VI. Nature of Assumptions in the Analysis for the Criterion of Mixing

It is necessary to call attention to the approximate nature of the assumptions that were made in the derivation of the criterion.

The first assumption is that the velocity of advance of the internal waves can be obtained by the ordinary well-known wave formula. The formula refers to the case of discrete densities and a surface of velocity discontinuity at the interface. Actually, although the condition of discrete velocities on the two sides of the interface is nearly satisfied, on the contrary the velocities are not discontinuous. In fact, at the instant just preceding the formation of nondeformable waves, the flow at the interface and on the two sides of it is viscous, and the regime is laminar. According to an analysis relative to the boundary layer of the interface when the density difference and the viscosity difference of the two liquids are small, the velocity at the interface is nearly half that of the current, the lower liquid being a pool [7]. During some of the runs small wax beads loaded with lead particles were introduced. These would fall through the lighter liquid, but in reaching the lower liquid the beads would float at the interface. The motion of the beads, whenever this was observed, showed that the interfacial velocity was nearly half that of the current. For example, in run E–19, corresponding to the current velocities 2.29, 3.53, and 4.56 cm/sec, the interface velocities noted were 1.37, 1.78, and 2.12 cm/sec, respectively. Thus, in a more precise derivation of the velocities of the interface waves, attention might be given to the laminar regime of the interface.

The second assumption consists of a statement as to the wavelengths attained at the instant the mixing is about to commence. The wavelengths for the current velocity are maximum values consistent with the condition of stability; that is,

$$\lambda=\frac{\pi U_c^2}{g\Delta\rho/\rho_1}. \tag{61}$$

Whenever records of wavelengths were kept, the recorded values appeared to be in agreement with the formula, as can be seen from the data in figure 8. The wavelengths were estimated rather than accurately measured. This fact and also the fact that the measurements are few appreciably weaken the value of the evidence shown.

The third assumption assigns to the waves a value of velocity propagation in conformity with the wavelengths; that is,

$$\omega=U_c/2. \tag{62}$$

Although in many cases this relation held nearly true, there were noted instances when the wave velocity was larger, and in the vicinity of $\omega=0.8U_c$.

The final assumption is in regard to the supply of energy to the internal waves. The source of supply is thought to be due to the eddies in the

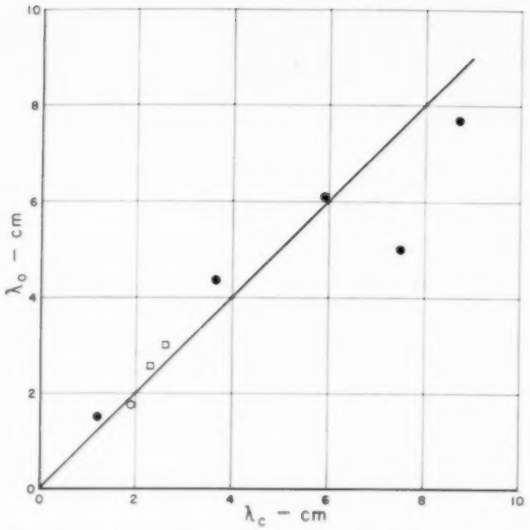

FIGURE 8. *Comparision of observed with computed wavelengths at initial mixing.*

troughs or depressions of the upper current. The supply is of such magnitude as to balance that part of the dissipation of the internal waves taking place in the liquid of the lower pool. Probably this idea is correct. However, our attempts to verify it by observations on the mechanism of flow did not prove successful.

Whatever be the details of a new analysis, carried out with greater rigor and with proper assumptions, the parametric form of the criterion of mixing will not be modified. Whatever changes are obtained will be in the nature of replacing the numerical constants appearing in eq 40, either by new constants or by a new function involving the densities and viscosities of the two liquids appearing as a correction.

VII. The Amount of Mixing With Increasing Current Velocity

The second purpose of the investigation was to determine the amount of mixing when the velocities of the current are above the critical value. The amount of mixing, q, may be defined as the volume of the heavier liquid that crosses unit area of the interface in unit time. The dimensions of the quantity q are that of velocity, and the symbol U_m will be used for this quantity. The tests of the amount of mixing were made with the large flume.

The experimental determinations of q, or of U_m, are based on the following simple concepts. Let V be the volume of the upper liquid. In these tests, V is the volume of the lighter liquid contained initially in the reservoir below and prior to its introduction into the flume. The heavy liquid of the pool is highly colored with a darkish-blue water-soluble dye. Let N be the number of coloring particles in unit volume of the heavier liquid. Let A_i be the total area of the interface. As a result of mixing the upper liquid becomes tinted. Let dN be the number of coloring particles entering into unit volume of the upper liquid during the time interval Δt when the current velocity is constant for this interval.

Because of continuity of mass

$$VdN = A_i q N \Delta t. \tag{63}$$

Introducing the symbol

$$\Delta C = dN/N, \tag{64}$$

$$q = \frac{V\Delta C}{A_i \Delta t}. \tag{65}$$

We may refer to ΔC as the increase in the fractional concentration of the upper liquid.

During the conduct of tests the velocity of the upper current was changed to the values u_1, u_2, u_3, . . . at the times t_0, t_1, t_2, ... Thus, during the time interval $t_1 - t_0$, the velocity of the current was constant and equal to u_1. In general, during the time interval $t_n - t_{n-1}$, the current velocity was u_n. At the times t_0, t_1, t_2, . . . ; that is, at the times that new velocities were established, samples s_0, s_1, s_2, . . . s_n of the liquid in the reservoir below were taken. Let the partial concentrations of these samples be C_0, C_1, C_2, . . . C_n, respectively. Thus to obtain the rate of mixing q_n, when the velocity of the current is u_n, we consider the equation

$$q_n = \frac{V(C_n - C_{n-1})}{A_i(t_n - t_{n-1})}. \tag{66}$$

The determination of the partial concentrations C of the samples s was effected by the use of photoelectric cells. Standard solutions of known partial concentrations of 0, 2, 4, 6, 9, and 10 percent, using the heavier liquid from the pool as base, were prepared. These were introduced one

at a time into a rectangular glass jar with plane polished surfaces. The jar was interposed between a source of light of constant illumination-intensity and a photoelectric cell, and the milliampere reading of the cell excitation was noted. The milliampere reading was taken as a measure of the partial concentration of the sample in the jar. These measurements of the standard solutions of known partial concentrations established a calibration curve. Next, the milliampere readings of the samples $s_0, s_1, \ldots s_n$ were obtained. By reference to the calibration curve, the partial concentrations $C_0, C_1, \ldots C_n$ were then determined.

The mixing-rate values as determined by the above process for run E–14 are given in figure 9. The circles correspond to the photoelectric measurements. The square marks the velocity U_1, which by visual observation was associated with the condition of slight mixing. The triangle marks what we have judged as the critical velocity, U_c. The distribution of the observation points marked by circles can be best approximated by a curved line. This same condition was observed in practically all of the runs of the E series. Nevertheless, for the purpose of effecting simplicity in the representation, a straight line is drawn, starting from the point of slight mixing, U_1. This means that, approximately, the amount of mixing is proportional to the increase of the current velocity above the velocity U_1 of slight mixing. Accordingly,

$$U_m/(U-U_1)=C. \tag{67}$$

The value of C, the constant of proportionality, from all the runs of the series E tests, made with the large flume, are shown in figure 10. It would seem that the magnitude of the constant decreases when the relative density of the pool liquid is increased. We shall ignore, provisionally, the effect of density. Furthermore, there is a correlation between the velocities U_1 and U_c, such that, $U_1=1.15U_c$. On this basis, the simplified form of the law of mixing rate will be

$$U_m=3.5\times10^{-4}(U-1.15\,U_c). \tag{68}$$

It was unfortunate that, due to the limitations of the apparatus and the capacity of the pump, it was not possible to have current velocities higher

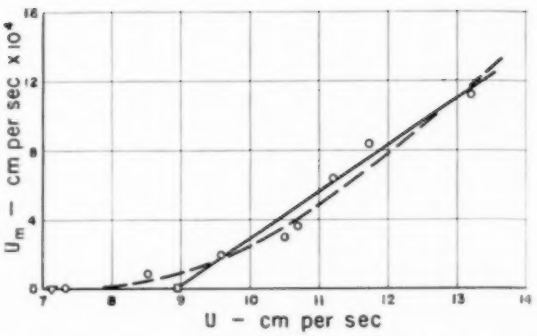

FIGURE 9. *Relation of amount of mixing to velocities of the current of light liquid.*

than those employed in the tests. It is important to have an idea of the limiting velocity where the law ceases to be linear, or nearly linear, and of the marked changes that may occur at the higher velocities. Another undesirable aspect of the

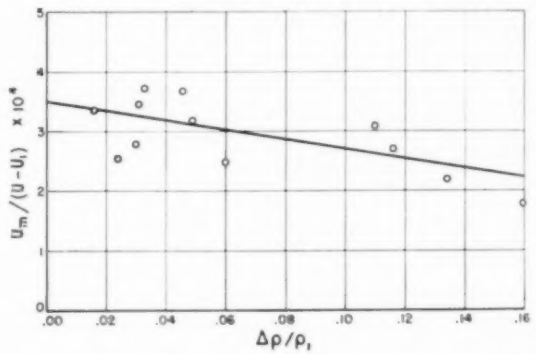

FIGURE 10. *Relation of amount of mixing to relative densities of the two liquids.*

apparatus was the shortness of the flumes. It was not always possible to divert correctly the dragging of heavier liquid at the exit end. In some cases the diversions were somewhat excessive and in others somewhat deficient, and, therefore, because of the shortness of the flume, errors were made in estimating the mixing rates, U_m.

It will be interesting at this point to inquire about the increased frictional force between the two liquids due to the mixing. The frictional force caused by the maintenance of the waves at the interface may be expressed as

$$\tau_1=\frac{1}{U}\frac{dE}{dt}, \tag{69}$$

where U is the current velocity and dE/dt the dissipation in the waves per unit area of interface. Writing for the shear,

$$\tau_1 = f_1 \rho U^2/2, \tag{70}$$

where f_1 is the coefficient of friction, it is seen that

$$f_1 = \frac{2}{\rho U^3} \frac{dE}{dt}. \tag{71}$$

As an estimate it may be supposed that the dissipation will take on the same value as for surface waves in contact with air. The expression is

$$\frac{dE}{dt} = 16\pi^3 \mu \omega^2 a^2/\lambda^3. \tag{72}$$

Hence,

$$f_1 = 32\pi^3 \frac{\nu}{\lambda U} \left(\frac{\omega}{U}\right)^2 \left(\frac{a}{\lambda}\right)^2. \tag{73}$$

Assume that $\omega = U/2$, a condition that was observed in some tests, and

$$f_1 = 8\pi^3 (\nu/\lambda U)(a/\lambda)^2. \tag{74}$$

This would indicate that, a and λ remaining the same, f_1 decreases with increasing U. Actually, however, a increases with U. Let it be assumed for the present that a^2 is proportional to U and that λ is unaltered. Then the value of the coefficient can be obtained by noting the conditions at the onset of mixing, and

$$f_1 = 8\pi^3 \frac{\nu}{\lambda U_c} \left(\frac{a}{\lambda}\right)^2, \tag{75}$$

where a and λ are the wave dimensions at the condition of slight mixing. Using the observed values $\lambda = 2.0$ cm, $a = 0.2$ cm, $\nu = 0.01$ cm^2/sec., and $U_c = 10$ cm/sec., we obtain

$$f_1 = 0.0010. \tag{76}$$

Denoting next the additional shearing resistance due to mixing by τ_2,

$$\tau_2 = \rho U_m U, \tag{77}$$

since the liquid crossing the interface is initially at rest, and after crossing the interface it takes on the velocity of the current. Writing τ_2 in the form

$$\tau_2 = f_2 \rho U^2/2, \tag{78}$$

then

$$f_2 = 2U_m/U. \tag{79}$$

Introducing the expression for U_m from eq 68

$$f_2 = 7.0 \times 10^{-4}(1 - 1.15 U_c/U). \tag{80}$$

Thus, if the mixing law as found above is valid also for large values of U, the coefficient of friction due to mixing is

$$f_2 < 0.0007. \tag{81}$$

These results show that for moderately small channels and moderately small velocities the friction coefficient at the interface is smaller than the coefficient ordinarily obtained for smooth-walled channels. Perhaps this explains our failure to obtain reliable readings of pressure fall along the flumes during the tests.

VIII. Mixing in a Large Body of Water

The bearing of the results of the present investigation on the interfacial mixing occurring in large bodies of water in stratified flow must be discussed.

In the laboratory experiments, where relatively short flumes are used and one of the liquids, the lower or the upper, is at rest, and the other is in motion, the state of the interface is one of discontinuity of density. In the case when the lower heavy liquid moves, it will be supposed that the flow has continued for a long time and that the characteristic wave front is absent. Under these conditions, the interfacial stability, the critical velocity of mixing, and the mixing for velocities above the critical may be studied. All these, however, refer to a reach that is to be looked upon as a type of initial length.

In the phenomenon transpiring in natural environments and thus involving large bodies of water in stratified flow, it may be assumed that conditions arise so that initial reaches are established. It is expected that the changes taking place in the initial length will be similar to those observed in a laboratory. What is not known definitely in this respect is the direct applicability of the results to be obtained in a laboratory investigation to the prototype magnitudes. Certainly, however, a qualitative similarity, at least, must exist.

If that is granted, the application of the laboratory results must be restricted to a very short reach, which will be viewed as the initial reach.

Beyond this in the remaining reach, which will be of considerable length, the conditions for mixing and the manner of mixing will be of a different type, obeying different laws. For the mixing in the initial reach will establish in the following adjoining reach a transition layer between the liquids, and in this transition layer the density will vary continuously. As an illustration of how this can be brought about, we may visualize the following situation. A current of fresh water of depth H is flowing with a uniform velocity over a pool of heavier liquid. In places in the initial length, portions of liquid coming from the lower pool will spread themselves in the upper current only gradually. Let it be supposed that the spreading is proportional to time, this being measured from the instant of departure from the lower liquid. The density gradient established for this case can be obtained readily. Taking the instant when the spreading is completed and the area covered is a square of sides of length H, the concentration along a vertical may be represented by

$$C=A+B/y, \tag{82}$$

for finite distances away from the interface.

Now, the actual law of spreading for a given actual case may not be as simple as in the above illustration. As long as it is assumed that spreading of liquids ejected from below into the upper current and in the initial length is gradual, a qualitatively similar law for the concentrations as the one mentioned above will be expected. But these distributions imply the existence of transition layers. Whereas the mixing in the case of sharp interfaces is brought about by the ejection of eddies at the crests of the internal waves, the mixing through the transition layers must be associated with the momentum exchange of turbulent motion. This is a matter to be approached using the basic ideas of the Prandtl and Richards criterion for mixing and is, therefore, a subject outside the scope of the present investigation.

The author expresses his appreciation to K. Hilding Beij, Assistant Chief of the National Hydraulic Laboratory, for his editorial review of the paper and for constructive suggestions.

IX. References

[1] Harold Jeffreys, On the formation of water waves by wind, Proc. Roy. Soc. [A] **107**, 189 (1925).

[2] Harold Jeffreys, Formation of water waves by wind, Proc. Roy. Soc. [A] **110**, 241 (1926).

[3] A. B. Basset, A treatise on hydrodynamics, Vol. II (Cambridge University Press, Cambridge, Eng. 1888).

[4] H. Lamb, Hydrodynamics (ed. 5), (Cambridge University Press, Cambridge, Eng., 1924).

[5] Lord Kelvin, Baltimore lectures on molecular dynamics and wave theory of light (Cambridge University Press, Cambridge, Eng., 1904).

[6] H. L. Dryden, F. D. Murnaghan, H. Bateman, Report of the committee on hydrodynamics, Bull. National Research Council, No. 84 (1922).

[7] G. H. Keulegan, Laminar flow at the interface of two liquids, J. Research NBS **32**, 303 (1944), RP1591.

Washington, May 26, 1949.

U. S. Department of Commerce
National Bureau of Standards

Research Paper RP2041
Volume 43, November 1949

Part of the Journal of Research of the National Bureau of Standards

The Remainder in Linear Methods of Approximation

By W. E. Milne [1]

The following discussion grows out of an effort to formulate a systematic treatment of the error for such diverse processes as interpolation, numerical differentiation, numerical integration, harmonic analysis, approximation by Least Squares, approximation by equating moments, and other allied operations.

First of all, a systematic and uniform procedure is exhibited by which a desired method of approximation may be explicitly constructed. Second, by suitable transformation the remainder is put in a form in which it is possible in many cases to estimate its approximate magnitude. And third, the theory is applied to a variety of concrete examples, and bounds are obtained for the magnitude of the error.

I. Fundamental Problem of Approximation

In the various types of problems to which this investigation applies, we are dealing with a real function $f(x)$ in an interval $a \leqq x \leqq b$, and we are supplied with a more or less adequate description, or definition, of this function. For example, we may have a table of values of $f(x)$ furnished by experimental observations, or a table of values of $f(x)$ computed from a series or an asymptotic expansion, or we may have the values, not of $f(x)$ itself, but of certain of its derivatives, $f'(x)$, or $f''(x)$ etc. In such instances $f(x)$ is not completely defined by the information provided. On the other hand, $f(x)$ may be a particular solution of a given differential equation, for which no solution in elementary form is known. Or $f(x)$ may be the solution of an integral equation or of some other type of functional equation. In such cases the function $f(x)$ may be completely, though implicitly, defined by the given equation.

The essential point is that we may not have a simple mathematical expression for $f(x)$, and yet we wish to obtain particular values of $f(x)$, or to find its integral, or to find its derivatives—in short to be able to use $f(x)$ just as freely as if it were expressed in terms of known elementary functions.

In order to do these things, a common practice is to replace $f(x)$ by an approximate expression in terms of suitably chosen known functions. How to secure this approximate representation of $f(x)$ is the problem that we shall call the fundamental problem of approximation.

In order that the subsequent analyses can be performed, it will be assumed henceforth that $f(x)$ has a continuous derivative of order $n+1$ in a fixed interval $a \leqq x \leqq b$. The values of n to be selected will appear as we proceed.

II. Basic Functions

In all the types of approximation here considered the first essential idea is to employ a basic set of linearly independent known functions $u_0(x)$, $u_1(x)$, . . ., $u_n(x)$, and to use an appropriately chosen linear combination of these functions as an approximation to the given function. So far as theory is concerned any other set $v_0(x)$, $v_1(x)$, . . ., $v_n(x)$, equivalent to the set $\{u_i(x)\}$ by linear combination, might equally well be used. In practical numerical analysis however, it is important to select the set best suited to the numerical process to be employed.

In numerical methods the set of basic functions more often employed than all others put together is the set of *polynomials*, $1, x, x^2, \ldots, x^n$. Actually these appear more frequently in various linear combination such as the binomial coefficient functions $\binom{x}{0}, \binom{x}{1}, \cdots \binom{x}{n}$, the Legendre polynomials $P_0(x)$, $P_1(x)$, . . ., $P_n(x)$, the Lagrangian coefficients $L_0^{(n)}(x)$, $L_1^{(n)}(x)$, . . . $L_n^{(n)}(x)$, etc.

[1] Mathematics Department, Oregon State College.

Next in importance probably are the *trigonometric* functions, 1, cos x, sin x, . . . cos mx, *sin* mx which may also occur in power form, 1, cos x, sin x, . . ., $\cos^m x$, $\sin^m x$, or in products of terms such as sin $(x-x_i)/2$.

Other sets sometimes used are $e^{-x^2/2}\ H_i(x)$, where $H_i(x)$ is an Hermitian polynomial, $e^{-x}L_i(x)$, where $L_i(x)$ is a Laguerre polynomial, etc.

It is assumed henceforth that the basic functions $u_0(x)$, $u_1(x)$, . . ., $u_n(x)$ all possess continuous derivatives of order $n+1$ in the closed interval $a \leqq x \leqq b$, and that the Wronskian determinant

$$W=\begin{vmatrix} u_0(x) & u_1(x) & \cdots & u_n(x) \\ u_0'(x) & u_1'(x) & \cdots & u_n'(x) \\ \cdots & \cdots & \cdots & \cdots \\ u_0^{(n)}(x) & u_1^{(n)}(x) & \cdots & u_n^{(n)}(x) \end{vmatrix}$$

does not vanish anywhere in the interval $a \leqq x \leqq b$.

III. Equivalence Operators

The basic set of approximating functions having been selected, the next step in solving the fundamental problem of approximation is to set up the rule by means of which the coefficients in the approximating linear combination of basic functions are to be determined. We shall consider here only objective, analytic methods, as opposed to subjective and graphical methods. With this restriction, it will be found that in a great many cases of practical importance, the rule is based on what might be called the *principle of equivalence*. We shall not attempt to formulate a completely general statement of this principle, but shall instead bring out its meaning by citing some familiar examples in which a principle of equivalence is employed. Such examples are:

(a). Equivalence of *value* at discrete points. That is, the value of the approximating function is made equal to the value of the given function $f(x)$ at $x_0, x_1, \ldots, x_n$.

(b). Equivalence of *lineal elements* at discrete points. That is, the values of the approximating function and its first derivative are made to agree with $f(x)$ and $f'(x)$ at assigned points. This may also be regarded as a limiting case of (a) when pairs of points move into coincidence.

(c) Equivalence of *weighted definite integrals*. That is, the value of

$$\int_a^b w_i(x)\ f(x)\ dx,$$

are made to agree with corresponding expressions formed for the approximating function.

(d) Equivalence of *weighted sums*. That is, the values of

$$\sum_{j=0}^{M} w_i(x_j)\ f(x_j),$$

are made to agree with similar expressions for the approximating function.

Evidently this list can be greatly extended.

We shall henceforth in this paper consider only cases in which the coefficients are completely determined by some appropriate application of the principle of equivalence.

In order to treat all such cases by means of a comprehensive notation, it is convenient to introduce a set of operators $O_0, O_1, \ldots, O_n$, equal in number to the set of basic functions, and called *equivalence operators*. What these operators actually do in any particular method of approximation is determined by the rule selected for setting up the approximation. For the examples (a), (b), (c), and (d) above the corresponding operators are:

(a) $O_i f(x)=f(x_i)$; $\quad i=1, \ldots, n.$

(b) $O_{2i} f(x)=f(x_i)$, $\quad i=1, \ldots, n.$

$O_{2i+1} f(x)=f'(x_i)$;

(c) $O_i f(x)=\int_a^b w_i(x)\ f(x)dx$; $\quad i=1, \ldots, n.$

(d) $O_i f(x)=\sum_{j=0}^{M} w_{ij} f(x_j)$; $\quad i=1, \ldots, n.$

It is desirable to employ some form of analytical expression for the operators O_i, sufficiently general to include all types of linear operators likely to arise, but sufficiently restricted to guarantee that subsequent mathematical manipulations can be carried out. Accordingly, it is assumed henceforth that $O_i f(x)$ can be expressed by means of Riemann-Stieltjes integrals in the form

$$O_i f(x)=\sum_{j=0}^{k} \int_a^b f^{(j)}(x) dq_{ij}(x), k<n,$$

in which the $q_{ij}(x)$ are suitably chosen functions of bounded variation in the interval $a \leqq x \leqq b$. By specialized choices of the q_{ij} we may obtain each of the particular operators (a), (b), (c), and (d) listed above. For example, if $q_{i0}(x)$ is a step function with unit step at $x=x_i$ while the other $q_{ij}(x)$ vanish we have

$$O_i f(x) = \int_a^b f^{(0)}(x) dq_{i0}(x) = f^{(0)}(x_i).$$

Again if $dq_{i0}(x) = w_i(x)dx$ and $q_{ij}=0$ for $j=1, 2, \ldots, k$, then

$$O_i f(x) = \int_a^b w_i(x) f(x) dx.$$

Also if $q_{i0}(x)$ is a step function having $M+1$ steps of magnitude w_{i0} at x_0, w_{i1} at x_1, . . ., w_{iM} at x_M, and if $q_{ij}=0$, for $j>0$, then

$$O_i f(x) = \sum_{j=0}^{M} w_{ij} f(x_j).$$

From the definition of O_i as a sum of integrals, it is clear that

(1) The operation O_i is *distributive* with respect to addition, i. e.,

$$O_i[f_1(x) + f_2(x)] \equiv O_i f_1(x) + O_i f_2(x),$$

$$(O_1 + O_2) f(x) \equiv O_1 f(x) + O_2 f(x).$$

(2) If A is constant

$$O_i[Af(x)] \equiv AO_i f(x).$$

(3) The result of the operation O_i on any function $f(x)$ no longer contains x as an *independent* variable and insofar as the variable x is concerned may be treated as a constant.

IV. The Approximation Formula

Suppose that the function $f(x)$ has been given in any of the ways suggested in section I, that an appropriate basic set $\{u_i\}$ has been chosen, that a rule for determining the coefficients based on the principle of equivalence has been selected (i. e., the equivalence operators $O_1, O_2, \ldots, O_n$ are decided upon), and that what we desire is a formula expressing the result of some given operation O when performed on $f(x)$, where O satisfies the conditions imposed on the O_i in section III. Let the desired approximating linear combination of the u_j be

$$\sum_{j=0}^{n} A_j u_j(x),$$

in which the A's are coefficients to be determined. Then the principle of equivalence gives the $n+1$ equations

$$O_i f(x) = O_i \sum_{j=0}^{n} A_j u_j(x).$$

which by the properties stated at the end of section III are the same as

$$O_i f(x) = \sum_{j=0}^{n} A_j O_i u_j(x). \qquad (1)$$

It is assumed henceforth that the determinant

$$D = \begin{vmatrix} O_0 u_0(x) & O_1 u_0(x) & \ldots & O_n u_0(x) \\ O_0 u_1(x) & O_1 u_1(x) & \ldots & O_n u_1(x) \\ \ldots & \ldots & \ldots & \ldots \\ O_0 u_n(x) & O_1 u_n(x) & \ldots & O_n u_n(x) \end{vmatrix}$$

does not vanish. Clearly the $n+1$ eq 1 determine the coefficients A_j uniquely.

Our objective is to express the result of the operation O applied to $f(x)$ by means of the same operation, O, applied to the approximating function $\Sigma A_i u_i(x)$, together with a remainder term, R, denoting the error of this approximate representation. That is

$$Of(x) - O \sum A_i u_i(x) = R.$$

When the values of the A_i as determined by eq 1 are substituted in the expression for R, the left-hand member may be written in determinant form, and we have the general expression for the error term

$$\frac{1}{D} \begin{vmatrix} Of(x) & O_0 f(x) & O_1 f(x) & \ldots & O_n f(x) \\ Ou_0(x) & O_0 u_0(x) & O_1 u_0(x) & \ldots & O_n u_0(x) \\ Ou_1(x) & O_0 u_1(x) & O_1 u_1(x) & \ldots & O_n u_1(x) \\ \ldots & \ldots & \ldots & \ldots & \ldots \\ Ou_n(x) & O_0 u_n(x) & O_1 u_n(x) & \ldots & O_n u_n(x) \end{vmatrix} = R. \qquad (2)$$

Formula 2 provides the explicit means for setting up any linear approximation formula when the desired operation O, the basic set $u_i(x)$, and the

rule for the coefficients based on the principle of equivalence have been selected.

It is obvious from formula 2 that R vanishes whenever $f(x)$ is any linear combination of the basic set $\{u_i(x)\}$. Also, R vanishes if the operator, O, is any linear combination of the operators O_0, O_1, . . ., O_n.

V. The Operator R

Since we have assumed that the operator, O, is expressible by means of Riemann-Stieltjes integrals just as are the O_i, it is clear from formula 2 that R may be looked upon as the result of an operation of this same general type performed on the function $f(x)$ and might be called $O'f(x)$. However, we wish to retain the letter R associated with the idea of a remainder term, and hence shall use the notation

$$R=R[f(x)],$$

indicating both that R is a remainder and also that R is the result of a linear operator operating on the function $f(x)$.

This operator also obeys the distributive property with respect to addition so that

$$R[f_1(x)+f_2(x)]=R[f_1(x)]+R[f_2(x)].$$

Moreover, as we observed at the end of section IV,

$$R[u_i(x)]=0, \quad i=0, \quad 1, \quad \ldots, \quad n.$$

These two properties of R are essential in the subsequent developments.

A few examples showing the formation of $R[f(x)]$ in specific cases will be illuminating. In each case D is the cofactor of the element in the upper left-hand corner of the numerator determinant. If the values $x_0, x_1, \ldots, x_n$ are all distinct it may be shown that in none of these cases does D vanish.

Example 1. *Polynomial interpolation.*

Here the formula is

$$\frac{1}{D}\begin{vmatrix} f(x) & f(x_0) & f(x_1) & \ldots & f(x_n) \\ 1 & 1 & 1 & \ldots & 1 \\ x & x_0 & x_1 & \ldots & x_n \\ x^2 & x_0^2 & x_1^2 & \ldots & x_n^2 \\ \ldots & \ldots & \ldots & \ldots & \ldots \\ x^n & x_0^n & x_1^n & \ldots & x_n^n \end{vmatrix} = R[f(x)].$$

Example 2. *Lineal element interpolation.*

$$\frac{1}{D}\begin{vmatrix} f(x) & f(x_0) & f'(x_0) & \ldots & f(x_n) & f'(x_n) \\ 1 & 1 & 0 & \ldots & 1 & 0 \\ x & x_0 & 1 & \ldots & x_n & 1 \\ x^2 & x_0^2 & 2x_0 & \ldots & x_n^2 & 2x_n \\ \ldots & \ldots & \ldots & \ldots & \ldots & \ldots \\ x^{2n+1} & x_0^{2n+1} & (2n+1)x_0^{2n} & \ldots & x_n^{2n+1} & (2n+1)x_n^{2n} \end{vmatrix} = R[f(x)].$$

Example 3. *Quadrature formula.*

$$\frac{1}{D}\begin{vmatrix} \int_\alpha^\beta f(x)dx & f(x_0) & f(x_1) & \ldots & f(x_n) \\ \beta-\alpha & 1 & 1 & \ldots & 1 \\ \frac{\beta^2-\alpha^2}{2} & x_0 & x_1 & \ldots & x_n \\ \frac{\beta^3-\alpha^3}{3} & x_0^2 & x_1^2 & \ldots & x_n^2 \\ \ldots & \ldots & \ldots & \ldots & \ldots \\ \frac{\beta^{n+1}-\alpha^{n+1}}{n+1} & x_0^n & x_1^n & \ldots & x_n^n \end{vmatrix} = R[f(x)].$$

Example 4. *Taylor's series with remainder*

$$\frac{1}{D}\begin{vmatrix} f(x) & f(x_0) & f'(x_0) & \cdots & f^{(n)}(x_0) \\ 1 & 1 & 0 & \cdots & 0 \\ x & x_0 & 1 & \cdots & 0 \\ x^2 & x_0^2 & 2x_0 & \cdots & 0 \\ \cdots & \cdots & \cdots & \cdots & \cdots \\ x^n & x_0^n & nx_0^{n-1} & \cdots & n! \end{vmatrix} = R[f(x)].$$

Example 5. *Least square approximation.*

Since any linearly independent set of functions can be made orthonormal by linear combination, the basic set itself may be assumed to be orthonormal with respect to a given interval $a \leqq x \leqq b$. Then with the abridged notation

$$\int fu = \int_a^b f(x)u(x)dx, \text{ etc.},$$

the formula is

$$\frac{1}{D}\begin{vmatrix} f(x) & \int fu_0 & \int fu_1 & \cdots & \int fu_n \\ u_0(x) & 1 & 0 & \cdots & 0 \\ u_1(x) & 0 & 1 & \cdots & 0 \\ \cdots & \cdots & \cdots & \cdots & \cdots \\ u_n(x) & 0 & 0 & \cdots & 1 \end{vmatrix} = R[f(x)].$$

A Fourier series with remainder is a particular case of this example. So also is Least Square approximation using Legendre Polynomials.

The procedure outlined above evidently has great flexibility, since theoretically at least there are infinitely many ways of choosing a basic set of functions, infinitely many ways of selecting the rule for forming the coefficients based on the equivalence principle, and similarly for $f(x)$ and the operator O.

It should be emphasized that although eq 2 has been called "an approximation formula", it is not necessarily in any sense a "good" approximation. Only when the remainder term $R[f(x)]$ is small enough to be ignored without affecting the desired accuracy do we call it a good approximation.

VI. The Basic Differential Equation

Since the functions $u_i(x)$ have continuous derivatives of order $n+1$ and the Wronskian, W, does not vanish in the interval $a \leqq x \leqq b$, we may construct a homogeneous linear differential equation

$$L(u) = D^{n+1}u + P_1(x)D^n u + P_2(x)D^{n-1}u + \cdots + P_{n+1}(x)u = 0$$

of order $n+1$ with coefficients $P_i(x)$ continuous in $a \leqq x \leqq b$, which has the $n+1$ functions $u_i(x)$ as a set of linearly independent solutions.

In determinant form this differential equation is

$$\frac{1}{W}\begin{vmatrix} u^{(n+1)} & u^{(n)} & u^{(n-1)} & \cdots & u \\ u_0^{(n+1)} & u_0^{(n)} & u_0^{(n-1)} & \cdots & u_0 \\ u_1^{(n+1)} & u_1^{(n)} & u_1^{(n-1)} & \cdots & u_1 \\ \cdots & \cdots & \cdots & \cdots & \cdots \\ u_n^{(n+1)} & u_n^{(n)} & u_n^{(n-1)} & \cdots & u_n \end{vmatrix} = 0$$

Example 1. For the basic set of polynomials 1, x, . . ., x^n, the differential equation is simply

$$L(u) = D^{n+1}u = 0.$$

Example 2. For the basic trigonometric functions, 1, cos x, sin x, . . ., cos mx, sin mx, the equation is

$$D(D^2+1)(D^2+2^2) \cdots (D^2+m^2)u = 0.$$

Example 3. For the basic hyperbolic set 1, cosh x, sinh x, . . ., cosh mx, sinh mx, the equation is

$$D(D^2-1)(D^2-2^2) \cdots (D^2-m^2)u = 0.$$

Example 4. For the basic exponential set e^x, e^{2x}, . . ., e^{mx} the equation is

$$(D-1)(D-2) \cdots (D-m)u = 0.$$

It is of interest to note that in each of these four examples the differential equation has constant coefficients. In general, of course, the coefficients are functions of x. It may also be noted that in the first three examples above the differential equation is self-adjoint.

The general solution of the nonhomogeneous differential equation

$$L(u)=\phi(x),$$

is

$$u=\sum_{i=0}^{n} C_i u_i(x)+\int_a^x \phi(s)g(x,s)ds, \tag{3}$$

in which the C_i's are arbitrary constants and

$$g(x,s)=\frac{\begin{vmatrix} u_0(x) & u_1(x) & \cdots & u_n(x) \\ u_0^{(n-1)}(s) & u_1^{(n-1)}(s) & \cdots & u_n^{(n-1)}(s) \\ \cdots & \cdots & \cdots & \cdots \\ u_0'(s) & u_1'(s) & \cdots & u_n'(s) \\ u_0(s) & u_1(s) & \cdots & u_n(s) \end{vmatrix}}{\begin{vmatrix} u_0^{(n)}(s) & u_1^{(n)}(s) & \cdots & u_n^{(n)}(s) \\ u_0^{(n-1)}(s) & u_1^{(n-1)}(s) & \cdots & u_n^{(n-1)}(s) \\ \cdots & \cdots & \cdots & \cdots \\ u_0'(s) & u_1'(s) & \cdots & u_n'(s) \\ u_0(s) & u_1(s) & \cdots & u_n(s) \end{vmatrix}} \tag{4}$$

The essential property of $g(x,s)$ is that

$$\frac{\partial^k}{\partial x^k}g(x,s)=\begin{cases}0 \text{ at } x=s \text{ for } k=0,\ 1,\ \ldots,\ n-1\\ 1 \text{ at } x=s \text{ for } k=n.\end{cases} \tag{5}$$

VII. The Function $g(x, s)$

For the basic set $1, x, x^2, \ldots, x^n$ we find that

$$g(x,s)=(x-s)^n/n!.$$

For the basic set $1, \cos x, \sin x, \ldots, \cos mx, \sin mx$,

$$g(x,s)=\left[2\sin\left(\frac{x-s}{2}\right)\right]^{2n}\Big/(2n)!.$$

For the set $1, \cosh x, \sinh x, \ldots, \cosh mx, \sinh mx$,

$$g(x,s)=\left[2\sinh\left(\frac{x-s}{2}\right)\right]^{2n}\Big/(2n)!.$$

For the functions $e^{-x^2/2}H_n(x)$,

$$g(x,s)=e^{(s^2-x^2)/2}(x-s)^n/n!.$$

For the functions $e^{-x}L_n(x)$,

$$g(x,s)=e^{s-x}(x-s)^n/n!.$$

For the set $e^x, e^{2x}, \ldots, e^{(n+1)x}$,

$$g(x,s)=(e^{x-s}-1)^n/n!.$$

VIII. Expression for the Remainder

Let $f(x)$ be a function with a continuous derivative of order $n+1$ in the region under consideration and set up the nonhomogeneous differential equation

$$L(u)=L(f(x)).$$

A particular solution of this equation is obviously $u=f(x)$, and hence by eq 3

$$f(x)=\sum a_i u_i(x)+\int_a^x L(f(s))g(x,s)ds. \tag{6}$$

Suppose now that we have some particular operator, R, where R is formed for the same basic set as is eq 6. Applying the operator, R, to eq 6 we get, in view of distributive property of R,

$$R[f(x)]=\sum a_i R[u_i(x)]+R\left[\int_a^x L(f(s))g(x,s)ds\right].$$

Since $R[u_i(x)]=0,\ i=0,\ 1,\ \ldots,\ n$, the first term on the right drops out. Now R applied to any function $\varphi(x)$ has the form

$$R[\varphi(x)]=\sum_{i=0}^{k}\int_a^b \varphi^{(i)}(x)dq_i(x), \qquad k<n,$$

where the $q_i(x)$ are of bounded variation in $a\leqq x\leqq b$.

Consequently

$$R\left[\int_a^x L(f(s))g(x,s)ds\right]=\sum_{i=0}^{k}\int_a^b \frac{d^i}{dx^i}\left[\int_a^x L(f(s))g(x,s)ds\right]dq_i(x).$$

By successive differentiations of the integral and use of eq (5) at each step we obtain

$$\frac{d^i}{dx^i}\left[\int_a^x L(f(s))g(x,s)\right]=\int_a^x L(f(s))\frac{\partial^i}{\partial x^i}g(x,s)ds;$$

hence

$$R\left[\int_a^x L(f(s))g(x,s)ds\right]$$
$$=\sum_{i=0}^{k}\int_a^b\int_a^x L_i f(s))\,\frac{\partial^i}{\partial x^i}\,g(x,s)ds\,dq_i(x).$$

It is convenient to define $\bar{g}(x,s)$ by the conditions

$$\bar{g}(x,s)=\begin{cases} g(x,s) \text{ for } x\geqq s \\ 0 \quad\quad \text{for } x<s. \end{cases} \tag{7}$$

Then the functions $\partial^i\bar{g}(x,s)/\partial x^i$, $i=0, 1, \ldots, n-1$, are continuous in the square $a\leqq x\leqq b$, $a\leqq s\leqq b$, and vanish identically in that half of the square for which $x<s$. Hence in the double integral above we may replace g by $\bar{g}$, replace the variable upper limit x by the constant limit b, interchange the order of the integrations, and put the summation under the first integral. The result is

$$R\left[\int_a^x L(f(s))g(x,s)ds\right]=\int_a^b L(f(s))G(s)ds,$$

where we have set

$$G(s)=\sum_{i=0}^{k}\int_a^b\frac{\partial^i}{\partial x^i}\,\bar{g}(x,s)dq_i(x)$$
$$=R[\bar{g}(x,s)].$$

We have therefore

$$R[f(x)]=\int_a^b L(f(s))G(s)ds, \tag{8}$$

in which

$$G(s)=R[\bar{g}(x,s)]. \tag{9}$$

Note that R operates on $\bar{g}(x,s)$ as a function of x, not s. Equation 8 provides the desired expression for the remainder term. It should be noted that eq 8 is merely a mathematical identity and therefore in one sense tells us nothing new. Actually, however, eq 8 accomplishes the important step of separating the problem into two parts, one of which, $L(f(s))$, is independent of the operator R, and the other, $G(s)$, independent of the function $f(x)$.

IX. The Function $G(s)$

For brevity the function $G(s)$ has been written as a function of the single variable s, since s is the variable of immediate concern in the integral of eq 8. In reality $G(s)$ depends, directly or indirectly, also on all the values of x, fixed or variable, that are implied in the performance of the operation R. When s is larger than the largest x involved in the operation $R[f(x)]$, the function $G(s)$ vanishes identically because for all such values of s the function $\bar{g}(x,s)$ is zero by definition. Again if s is less than the least x involved in $R[f(x)]$ the function $G(s)$ vanishes identically, this time because $\bar{g}(x,s)=g(x,s)$ and is therefore simply a linear combination of the $u_i(x)$, so that

$$R[\bar{g}(x,s)]=0.$$

It follows that the limits a, b, of the integral in eq 8, may as well be replaced by $-\infty$, $+\infty$, respectively.

The behavior of $G(s)$ in the interval where it does not vanish can best be illustrated by a number of simple examples.

Example 1. Let the basic set be 1, x, x^2, x^3, let x_0, x_1, x_2, x_3, x_4 be five equally spaced values of x with interval h, let $y_i=f(x_i)$ and let

$$R[f(x)]=y_4-4y_3+6y_2-4y_1+y_0=\Delta^4y_0.$$

For this case

$$\bar{g}(x,s)=(x-s)^3/3!, x>s,$$

whence

$$G(s)=R[\bar{g}(x,s)]=\frac{1}{3!}\,[\overline{(x_4-s)}^3-4\overline{(x_3-s)}^3+$$
$$6\overline{(x_2-s)}^3-4\overline{(x_1-s)}^3+\overline{(x_0-s)}^3],$$

where the notation $\overline{(x-s)}^3$ means that

$$\overline{(x-s)}^3=\begin{cases}(x-s)^3 & \text{if } x\geqq s, \\ 0 & \text{if } x<s.\end{cases}$$

We now see at once that for

$x_4 s\leqq<\infty$	$G(s)=0$
$x_3 s\leqq<x_4$	$G(s)=\frac{1}{3!}\,(x_4-s)^3$
$x_2\leqq s<x_3$	$G(s)=\frac{1}{3!}\,[(x_4-s)^3-4(x_3-s)^3]$
$x_1 s\leqq<x_2$	$G(s)=-\frac{1}{3!}\,[-4(x_1-s)^3+(x_0-s)^3]$
$x_0 s\leqq<x_1$	$G(s)=-\frac{1}{3!}\,[(x_0-s)^3]$
$-\infty<s<x_0$	$G(s)=0.$

855498—49——6

The graph of this function is shown in figure 1.

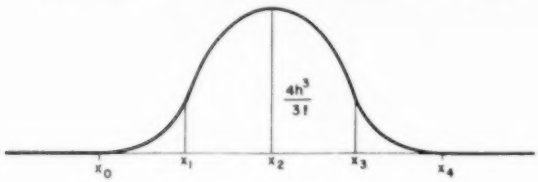

FIGURE 1.

Thus it is seen that $G(s)$ consists of four arcs of four different third-degree polynomial curves joined together continuously and with continuous first and second derivatives.

Since we started with $R[f(x)]=\Delta^4 y_0$, we have shown that

$$\Delta^4 y_0=\int_{-\infty}^{\infty} f^{(4)}(s)G(s)ds,$$

when $G(s)$ is the function just described.

Example 2. Let the basic set be $1, x, x^2, x^3, x^4$, let x_0, x_1, x_2 be three equally spaced points with interval h, and let

$$R[f(x)]=y_2-y_0-\frac{h}{3}(y_2'+4y_1'+y_0').$$

(This is equivalent to Simpson's Rule).

For this case

$$\overline{g}(x,s)=\overline{(x-s)}^4/4!$$

whence

$$G(s)=\frac{\overline{(x_2-s)}^4-\overline{(x_0-s)}^4}{4!}$$

$$-\frac{h}{3\times 3!}[\overline{(x_2-s)}^3+4\overline{(x_1-s)}^3+\overline{(x_0-s)}^3].$$

We have then:

$$x_2\leq s<\infty \qquad G(s)=0$$

$$x_1\leq s<x_2 \qquad G(s)=\frac{(x_2-s)^4}{4!}-\frac{h(x_2-s)^3}{3\times 3!}$$

$$x_0\leq s<x_1 \qquad G(s)=\frac{(x_0-s)^4}{4!}+\frac{h(x_0-s)^3}{3\times 3!}$$

$$-\infty<s<x_0 \qquad G(s)=0.$$

The graph of this function is shown in figure 2. Here $G(s)$ consists of arcs of two fourth-degree polynomials joined together with third-degree contact.

Recalling the original definition of $R[f(x)]$ in this example we see that

$$y_2-y_0-\frac{h}{3}(y_2'+4y_1'+y_0')=\int_{-\infty}^{\infty} y^{(5)}(s)G(s)ds.$$

The right-hand member of this equation is therefore a measure of the error of Simpson's rule in the special form chosen here.

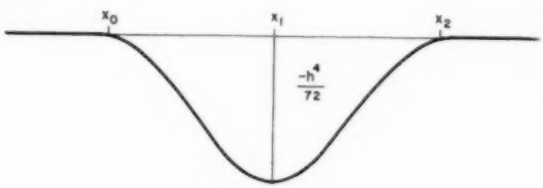

FIGURE 2.

Example 3. In the two preceding examples we have started with a known operator, R, and have derived from R the function $G(s)$. Now that we see something of the character of $G(s)$ in the case of a polynomial basic set, it is clear that we could reverse the process—i. e., start with a $G(s)$ satisfying suitable conditions as to degree and continuity and derive from it the operator R. To illustrate this procedure we start with

$$G(s)=0 \qquad \text{if } x_1\leq s,$$

$$G(s)=(x_1-s)^3(s-x_0)^3 \qquad \text{if } x_0\leq s<x_1,$$

$$G(s)=0 \qquad \text{if } s<x_0.$$

Here $G(s)$ is a polynomial of degree six, so that the basic set is $1, x, x^2, x^3, x^4, x^5, x^6$, the differential equation is $D^7 u=0$, and

$$R[f(x)]=\int_{-\infty}^{\infty} f^{(7)}(s)\overline{(x_1-s)}^3\overline{(s-x_0)}^3 ds$$

$$=\int_{x_1}^{x_0} f^{(7)}(s)(x_1-s)^3(s-x_0)^3 ds.$$

Now $G(s)=G'(s)=G''(s)=0$ at $s=x_0$ and at $s=x_1$.

$$G'''(x_0)=6h^3 \qquad G'''(x_1)=-6h^3$$

$$G^{(4)}(x_0)=-72h^2 \qquad G^{(4)}(x_1)=-72h^2$$

$$G^{(5)}(x_0)=360h \qquad G^{(5)}(x_1)=-360h$$

$$G^{(6)}(x_0)=-720 \qquad G^{(6)}(x_1)=-720.$$

Integration by parts gives accordingly

$$R[f(x)]=6h^3[f'''(x_1)+f'''(x_0)]$$

$$-72h^2[f''(x_1)-f''(x_0)]+360h[f'(x_1)+f'(x_0)]$$

$$-720[f(x_1)-f(x_0)].$$

Transposing and dividing by 720 we obtain the formula with remainder term

$$f(x_1)-f(x_0)=\frac{h}{2}[f'(x_1)+f'(x_0)]-\frac{h^2}{10}[f''(x_1)-f''(x_0)]+$$

$$\frac{h^3}{120}[f'''(x_1)+f'''(x_0)]-\frac{1}{720}\int_{x_0}^{x_1}f^{(7)}(s)(x_1-s)^3(s-x_0)^3ds.$$

This formula might be looked upon as the first few terms with remainder of a sort of two-point Taylor expansion. It can be used in successive approximations to secure a starting value in the step-by-step integration of a differential equation. Its virtue lies in the fact that while it requires only the first three derivatives it is as accurate as a Taylor's series using the first six derivatives.

This example illustrates that fact that $G(s)$ is a kind of *generating* function from which the particular operator R associated with $G(s)$ can be obtained by carrying out the integration

$$\int_{-\infty}^{\infty}f^{(n+1)}(s)G(s)ds.$$

It is this property which suggested the notation $G(s)$.

Example 4. In certain instances it may be easier to determine the contact properties by which the arcs composing the function $G(s)$ are joined and to construct $G(s)$ from these data rather than to compute $R[(x-s)^n]$ directly. An instance of this is the following: Let the basic set be $1, x, \ldots, x^n$, and let $R[f(x)]$ represent the difference between $f(x)$ and the best n-th degree polynomial approximation by Least Squares for the interval $(-1, 1)$. We shall suppose that x is in this interval. A brief examination will show that $G(s)$ is of degree n in x, of degree $2n+1$ in s, vanishes at $s=1$ to the same order as $(1-s)^{n+1}$, vanishes at $s=-1$ to the same order as $(1+s)^{n+1}$, and if G_R and G_L are the polynomials to the right and left respectively of $s=x$, then

$$G_L=\frac{(x-s)^n}{n!}+G_R.$$

These data determine G_R and G_L completely and after considerable algebraic reduction it is found that

$$G(s)=\frac{1-s^{n+1}}{2^{2n+1}n!}\left[\sum_{k=0}^{n}\frac{1}{2^k k!}\frac{d^k}{dx^k}\left\{(x+1)^n(x-1)^k\right\}(1+s)^k\right],$$

$$\text{for } x<s<1.$$

The foregoing examples furnish an idea of the character of (Gs) when the basic set consists of polynomials. Similarly when the basic set is trigonometric we would expect to find that $G(s)$ is composed of trigonometric arcs welded together; for the exponential case, $G(s)$ would be made up of exponential arcs, etc.

X. Computation of the Error

As has been shown, the remainder is of the form

$$R[f(x)]=\int_{-\infty}^{\infty}L(f(s))G(s)ds.$$

If $a\leqq s\leqq b$ is the interval in which $G(s)$ is not identically zero, we have

$$|R[f(x)]|<MK(b-a), \tag{10}$$

in which

$$M=\max|L(f(s))| \text{ in } a\leq s\leq b,$$

$$K=\max|G(s)| \text{ in } a\leq s\leq b.$$

The inequality 10 provides a bound for the magnitude of the error in all cases.

In many particular problems this result can be considerably improved. For example, if $G(s)$ does not change sign in the interval (a,b) we may apply the law of the mean for integrals and write

$$R[f(x)]=L(f(\xi))\int_{-\infty}^{\infty}G(s)ds, \tag{11}$$

where $a<\xi<b$. Note that this is the case for examples 1, 2, and 3 of section IX. Since in those examples we have the explicit expressions for the several arcs of which $G(s)$ is composed, there is no difficulty in performing the integration over each arc and thus we can obtain the actual value of the integral

$$\int_{-\infty}^{\infty}G(s)ds.$$

However we now show that the value of the above integral may be obtained from the operator R without making any use of the explicit form of $G(s)$. Let $w(x)$ be any solution of the differential equation

$$L(w)=1,$$

and replace $f(x)$ in eq 8 by $w(x)$. The result is

$$R[w(x)]=\int_{-\infty}^{\infty}G(s)ds.$$

By using this result in eq 11 we have

$$R[f(x)]=L(f(\xi))R[w(x)], \tag{12}$$

provided $G(s)$ does not change sign.

XI. Polynomial Approximation

For the polynomial case where

$$L(u)=\frac{d^{n+1}u}{dx^{n+1}}=0,$$

a particular solution of $L(w)=1$ is

$$w(x)=x^{n+1}/(n+1)!.$$

Hence we have the theorem:

if, (a) *the basic set is* $1, x, \ldots, x^n$, *and*
(b) *the function* $G(s)$ *does not change sign, then the error is*

$$R[f(x)]=\frac{f^{(n+1)}(\xi)}{(n+1)!}R[x^{n+1}], \tag{13}$$

where $a<\xi<b$.

This result contains many well-known expressions for the error as special cases. For example, in the case of polynomial interpolation eq 13 reduces to

$$R[f(x)]=\frac{f^{(n+1)}(\xi)}{(n+1)!}(x-x_0)(x-x_1)\ \ldots\ (x-x_n).$$

In the type of interpolation where both $f(x)$ and $f'(x)$ are given by the approximating polynomial at the given points, eq 13 becomes

$$R[f(x)]=\frac{f^{(2n+2)}(\xi)}{(2n+2)!}(x-x_0)^2(x-x_1)^2\ \ldots\ (x-x_n)^2.$$

In the case of Newton-Cotes quadrature formulas, eq 13 also gives the same results as those obtained by the use of Bernoulli polynomials.

Example 1. In the case of Newton's "three eighth's rule" in the form

$$y_3-y_0-\frac{3h}{8}(y_3'+3y_2'+3y_1'+y_0')=R(y),$$

the basic set is $1, x, x^2, x^3, x^4$, and the points are $x_0, x_0+h, x_0+2h, x_0+3h$.

There is no loss in generality if we take $x_0=0$, since the formula is independent of any particular location on the x-axis. Then

$$R[x^5]=\left\{3^5-\frac{15}{8}(3^4+3\times2^4+3\times1^4+0^4)\right\}h^5=-9h^5/2,$$

and the error turns out to be

$$|R[y]|=\frac{y^{(5)}}{5!}\cdot\frac{9h^5}{2}=\frac{3h^5y^{(5)}}{80}.$$

Here, and elsewhere below, the argument of the derivative in the remainder has been suppressed.

The theorem also applies to a wide variety of approximate formulas that are not commonly treated in texts on interpolation and numerical integration, and to which the customary methods for obtaining the error do not directly apply.

A few such formulas, together with error terms, are listed below.

(1) $$y_n-y_{n-1}=\frac{h}{2}(y_n'+y_{n-1}')-\frac{h^2}{12}(y_n''-y_{n-1}'')+\frac{h^5y^{(5)}}{720}.$$

(2) $$y_n-y_{n-1}=\frac{h}{2}(y_n'+y_{n-1}')-\frac{h^2}{10}(y_n''-y_{n-1}'')+\frac{h^3}{120}(y_n'''-y_{n-1}''')-\frac{h^7y^{(7)}}{100800}.$$

(3) $$y_{n+1}=y_n+\frac{h}{24}(7y_{n+1}'+16y_n'+y_{n-1}')+\frac{h^2y_n''}{4}-\frac{h^5y^{(5)}}{180}.$$

(4) $$y_{n+2}=y_n+\frac{2h}{3}(5y_{n+1}'-y_n'-y_{n-1}')-2h^2y_n''+\frac{7h^5y^{(5)}}{45}.$$

(5) $$y_{n+1}=y_{n-1}+\frac{h}{15}(7y_{n+1}'+16y_n'+7y_{n-1}')-\frac{h^2}{15}(y_{n+1}''-y_{n-1}'')+\frac{h^7y^{(7)}}{4725}.$$

(6) $$y_{n+1}-2y_n+y_{n-1}=\frac{3h}{8}(y_{n+1}'-y_{n-1}')-\frac{h^2}{24}(y_{n+1}''-8y_n''+y_{n-1}'')+\frac{h^8y^{(8)}}{60480}.$$

(7) $$y_{n+1}=y_{n-1}+\frac{h}{105}(41y_{n+1}'+128y_n'+41y_{n-1}')-\frac{2h^2}{35}(y_{n+1}''-y_{n-1}'')+\frac{h^3}{315}(y_{n+1}'''+16y_n'''+y_{n-1}''')-\frac{h^{11}y^{(11)}}{130,977,000}.$$

These formulas have applications in the numerical solution of differential equations.

XII. Future Investigations

So far, the possibilities of securing usable remainder terms by the methods of this paper have not been fully explored. It is, for example, unknown whether these methods will give practically useful forms of the remainder for the case of polynomial approximation by Least Squares, for the case of Fourier series, and more general Fourier type expansions. These cases have, of course, been extensively studied by Dunham Jackson and others by using a very different line of attack.

Another matter deserving attention is the discovery of general theorems by which it can be determined for whole classes of operators whether or not the associated function $G(s)$ changes sign. For we have seen that when we know that $G(s)$ does not change sign the evaluation of the magnitude of the error is considerably simplified. On the other hand, if it is necessary to compute $G(s)$ in order to determine whether or not $G(s)$ changes sign, the benefit of this simplification is considerably reduced. Except in a few special cases such as polynomial interpolation, no such general theorems are known.

Los Angeles, February 25, 1949.